

Håvard Haugen

Spin and Charge Transport in Two-dimensional Electron Gases

Thesis for the degree of Philosophiae Doctor

Trondheim, October 2010

Norwegian University of Science and Technology
Faculty of Natural Sciences and Technology
Department of Physics



NTNU – Trondheim
Norwegian University of
Science and Technology

NTNU

Norwegian University of Science and Technology

Thesis for the degree of Philosophiae Doctor

Faculty of Natural Sciences and Technology
Department of Physics

© Håvard Haugen

ISBN 978-82-471-2379-9 (printed ver.)
ISBN 978-82-471-2380-5 (electronic ver.)
ISSN 1503-8181

Doctoral theses at NTNU, 2010:200

Printed by NTNU-trykk

To my dear Ellen

Abstract

With the continuing demand for miniaturisation from the electronics industry, it becomes increasingly important to understand the physical behaviour of nanometre sized conductors. State-of-the-art transistors have typical length scales of the order a few tens of nanometres. On these mesoscopic scales, quantum effects become important in certain semiconductor systems at low temperature, or in the case of the newly discovered graphene even at room temperature. The quantum effects can significantly alter the electronic behaviour of a device. Quantum transport on the mesoscopic scale is also interesting from a fundamental point of view, as it allows us to study the crossover between the quantum and classical regimes of physics.

The two-dimensional electron gases studied in this thesis can be created at the interface between a semiconductor and another semiconductor or an insulator. Graphene is another two-dimensional conductor which holds great promises for use in electronics, due to high mobilities, gate controllable doping, and its intrinsic two-dimensionality.

In the first two papers of this thesis [1, 2] we investigate spin transport in graphene. The first paper [1] suggests a way of inducing a significant spin polarisation in the non-magnetic material, while the second paper [2] examines the role of the spin-orbit interaction in highly doped graphene.

The last two papers [3, 4] study the non-local electronic signal that can be induced between two normal contacts in the presence of a superconductor. The physical process responsible for this signal, crossed Andreev reflection, has been suggested as a candidate for generating entangled electrons in a solid state device. While experimentally such a signal has only been observed beyond linear response or in the presence of interactions, we show that it is possible to generate this type of signal also in linear response.

Preface

This thesis is submitted to the Norwegian University of Science and Technology (NTNU) for partial fulfilment of the requirements for the degree of philosophiae doctor.

The doctoral work has been performed at the Department of Physics, NTNU, Trondheim, supervised by professor Arne Brataas, and financed by the Norwegian Research Council (NFR) through the STORFORSK project “Fundamentals of Condensed Matter” (grant no. 167498/V30).

I am the main author and contributor to all the papers, with important feedback and assistance from the respective co-authors.

Trondheim, October 2010

Håvard Haugen

Acknowledgements

Although pursuing a PhD in Physics is in many ways a solitary endeavour, I wouldn't have managed without the help and inspiration of many people.

First, I would like to thank my supervisor Arne Brataas for giving me the opportunity to work with him, and for sharing with me his great insights into physics. Arne's constructive and encouraging advice has always pointed me in the right direction when I was stuck. Also, I would like to thank him for the many opportunities of meeting and getting to know some of the leading scientists in our field through various conferences and workshops.

I would also like to thank my co-authors who have contributed valuable feedback, advice and knowledge. First, I would like to thank to Daniel Huertas Hernando for his patient guidance and many (heated) discussions about physics and science in general during the first years of my PhD. Thanks to Xavier Waintal for stimulating collaboration, and not the least for lending and teaching me how to use his versatile simulation software. I would also like to thank Gerrit E. W. Bauer for his detailed and ever constructive feedback. His contagious enthusiasm about physics and many other things has been a great inspiration to me.

During my four years as a PhD, I have shared office with four excellent individuals: Jørn Foros, Hans Joakim Skadsem, Severin Sadjina, and Swarnali Bandopadhyay. I have greatly appreciated the lunch and coffee breaks, hikes, shared conference experiences, ski jump competitions, and the many humorous discussions with you. A number of other people have also positively influenced my work environment. Some that deserve special mention are Lars Kyllingstad and Lars Leganger (in alphabetical order) for providing many coffee break opportunities, Johannes Jäschke for countless good conversations and for inspiration to renew my violin skills, Simen Ellingsen for shared studies of renormalisation and other difficult topics, and Terje Røsten for instant response to my computer problems.

I would also like to thank Knut Arne Strand for many deep conversations about much more than physics, and for making my mandatory guidance on student labs a fun and rewarding experience.

My parents deserve special mention for their continuous encouragement during my whole life. I still have much to learn from their sincerity, curiosity, and altruism. I am also thankful to my siblings and in-laws for their encouragement and genuine interest in what I am doing as a physicist. If I were only able to explain it to you!

Birk, you were lucky enough that you only had to endure your father's PhD anxieties for a few months. Your smile is priceless!

Finally, I want to mention my dear wife and friend Ellen. How you have managed to endure my many periods of frustration during these years is beyond my comprehension. Your smile, reassurance and vitality have enlivened me countless times. I'm looking forward to many more years spent with you!

Contents

| | |
|--|------------|
| Abstract | i |
| Preface | iii |
| Acknowledgements | v |
| Contents | vii |
| List of Papers | ix |
| List of Figures | xi |
| 1 Introduction | 1 |
| 2 Quantum transport | 4 |
| 2.1 Electrons in conductors | 4 |
| 2.2 Important length scales in mesoscopic physics | 5 |
| 2.3 Scattering theory | 7 |
| 2.4 Spintronics and magnetism | 10 |
| 3 Two-dimensional electron gases | 13 |
| 3.1 Semiconductor heterostructures | 13 |
| 3.2 Graphene | 14 |
| 4 Crossed Andreev reflection | 19 |
| 4.1 Superconductivity | 21 |
| 4.2 Basic processes in multiterminal devices containing a superconductor | 22 |
| 4.2.1 Andreev reflection | 22 |
| 4.2.2 Crossed Andreev reflection | 25 |
| 4.2.3 Electron transfer | 26 |
| 4.3 Scattering formulation | 27 |
| 5 Conclusion | 29 |
| Bibliography | 31 |

List of Papers

Paper [1]

H. Haugen, D. Huertas-Hernando & A. Brataas
Spin transport in proximity-induced ferromagnetic graphene
Physical Review B **77**, 115406 (2008)

Paper [2]

H. Haugen & A. Brataas
Spin transport in doped graphene
Unpublished manuscript (2010)

Paper [3]

H. Haugen, D. Huertas-Hernando, A. Brataas & X. Waintal
Crossed Andreev reflection versus electron transfer in three-terminal graphene devices
Physical Review B **81**, 174523 (2010)

Paper [4]

H. Haugen, A. Brataas, G. E. W. Bauer & X. Waintal
Focused crossed Andreev reflection
Preprint arXiv.org:1007.4653 (2010)
Submitted to Physical Review Letters

List of Figures

| | | |
|-----|---|----|
| 2.1 | The elements of scattering theory | 8 |
| 3.1 | Hexagonal lattice and first Brillouin zone of graphene | 15 |
| 4.1 | Schematic illustration of Andreev reflection | 23 |
| 4.2 | Illustration of spatially separated normal and Andreev reflection | 24 |
| 4.3 | Basic transport processes in a multiterminal device containing a superconductor | 25 |

1 Introduction

Waves surround us everywhere. Sound and light waves enable us to communicate through speech and gestures, and electromagnetic waves in various outfits provide the physical basis on which our modern communication society is built.

A wave is defined as the propagation of a disturbance through space and time [5], for example, due to the density variations caused by a loudspeaker pushing the air with a membrane. The wave can propagate through a medium as in the case of sound or water waves, or through vacuum in the case of electromagnetic waves.

A characteristic property of waves is the ability to interfere, whereby the amplitudes of waves add up to produce a total wave amplitude at a given point. An immediate consequence of this *superposition principle* is that waves from different sources can annihilate or amplify each other at certain points in space or time. The superposition principle, with associated interference, is the basis for such phenomena as the rainbow-coloured patterns observed in thin oil films, or the beating pattern that can be heard when two strings on a guitar are slightly out of tune.

In the presence of boundary conditions, such as when both ends of a guitar string are held fixed, only standing waves with certain characteristic frequencies can exist, while waves with other frequencies quickly die out. This “quantisation” gives musical instruments their ability to produce sound waves with a clear pitch. In general, the sound from an instrument is a superposition of waves with the fundamental frequency and many of its overtones, where the geometry and material of the instrument determines the amplitude or weight of each overtone. This weighting gives each instrument its characteristic timbre.

In classical mechanics a physical body is completely characterised by its position and momentum, or by the positions and momenta of its constituent particles [5, 6]. Waves transfer energy and momentum from one particle to another, and can be thought of as the collective motion of many particles [5]. However, during the development of quantum theory during the first quarter of the 20th century, it became apparent that this classical picture of matter was inadequate when trying to explain features of very small bodies such as atoms. Consistency with experiments could only be achieved by assuming that matter itself has both wave-like and particle-like properties. The wave-like properties of matter manifest themselves in that physical bodies can be assigned a wave length called the de Broglie wave length, which is directly related to the momentum of the body [7].

In quantum theory, the properties of a physical single particle system is described by a complex

valued wave function $\psi(\mathbf{r}, t)$, which evolves in time according to the Schrödinger equation,

$$i\hbar\partial_t\psi(\mathbf{r}, t) = H\psi(\mathbf{r}, t). \quad (1.1)$$

Here H is the Hamiltonian operator associated with the total classical energy and \hbar is the reduced Planck's constant. To completely specify the state of the system, Eq. (1.1) must also be supplemented with an initial condition, specifying the known state of the system at an earlier instant, $\psi(\mathbf{r}, 0) = f(\mathbf{r})$. Quantum theory is inherently probabilistic in that we cannot know with absolute certainty the outcome of a measurement event. However, the absolute square of the wave function, $|\psi(\mathbf{r}, t)|^2$ gives us the probability for observing the particle at the position \mathbf{r} and time t [8].

The wave-like nature of matter manifests itself in that the wave function ψ can be expressed as a weighted superposition of amplitudes. For example, choosing to expand the wave function in the eigenstates of the energy operator H , we have

$$\psi(\mathbf{r}, t) = \sum_{\alpha} c_{\alpha}\phi_{\alpha}(\mathbf{r})e^{-iE_{\alpha}t/\hbar}, \quad (1.2)$$

where the quantum numbers α characterise all the symmetries of the Hamiltonian, and contain in principle both continuous and discrete labels [9]. Just as for classical waves, the superposition can lead to constructive or destructive interference such that the probability of observing the particle certain regions of time and space might be high or low, respectively.

The classical description of electrical conduction in a metal treats the electrons as charged particles that can be accelerated by an electric field [5]. Collisions with impurities and vibrating lattice ions leads to a viscous force opposing the acceleration, a picture that correctly yields Ohm's law, which states that the current density is proportional to the electric field [5]. Certain quantum mechanical aspects of the scattering process can be incorporated, yielding a semi-classical transport theory where the dynamics of the electrons is described by a Boltzmann transport equation analogous to the dynamic equation for an ideal classical gas [10]. This semi-classical treatment is adequate for metals at ambient temperatures and also for semiconductors at low temperatures when length and/or time scales are so long that interference effects are washed out [9, 10].

However, at shorter length scales the wave nature of the conduction electrons become important. This is especially true in two-dimensional electron gases, where the de Broglie wave length of the conduction electrons can easily reach tens of nanometres [11]. If typical sample dimensions are also of this magnitude, a quantum transport treatment is needed to properly account for interference effects.

The motivations for studying quantum transport properties in mesoscopic condensed matter systems can be grouped in two broad categories. First, it allows us to learn about the behaviour of physical systems governed by quantum mechanics, and especially about the crossover between the quantum and the classical regime. Second, the field has many technological applications, the most obvious being due to the continuing demand for miniaturisation of electronic devices. Characteristic dimensions of state-of-the-art transistors are typically less than 100 nm

[12]. Quantum effects might therefore soon have to be taken into consideration in the design of electronic components.

This thesis is divided into two parts: (i) A general introduction to the topic of quantum transport in two-dimensional electron gases, and (ii) a collection of four papers resulting from my PhD work.

The topic of the two first papers is spin transport in graphene, a recently discovered two-dimensional carbon material which exhibits exceptional conduction properties.¹ The first paper [1] proposes a way of inducing spin polarisation in this non-magnetic material, while the second paper [2] examines the role of the spin-orbit coupling for spin transport in doped graphene.

The remaining two papers [3, 4] discuss transport in the presence of crossed Andreev reflection, a physical process in which electrons in two separate non-superconducting contacts become strongly correlated when connected to a superconductor. Crossed Andreev reflection has been proposed as a candidate process for creating a solid state entangler, with applications to cryptography and secure communication. We investigate how crossed Andreev reflection can be detected by suppressing competing processes, either due to geometric effects in graphene nanoribbons [3] or by using an external magnetic field [4].

¹As I was finishing this thesis, this year's Nobel Prize in Physics was announced [13]. I was, naturally, delighted to learn that the prize was awarded to the two main scientist behind the first experimental isolation of graphene.

2 Quantum transport

Mesoscopic physics is the study of condensed matter systems on length scales ranging from nanometres to micro metres [11]. This is an intermediate or crossover regime between the microscopic details associated with the individual atoms of a material and the macroscopic behaviour observed with the bare eye. The prospect for applications in the electronic and computer industry is an important motivation for understanding the transport properties of mesoscopic systems. Mesoscopic physics is also interesting from a fundamental point of view, since many phenomena that originate from the quantum nature of matter can be studied in mesoscopic samples. Examples of such phenomena are the quantised Hall effects [14–16], weak localisation [17], artificially engineered energy levels in quantum dots [18], and several others [11].

Physical processes on macroscopic length scales are well described by the classical theories due to Newton and Einstein (with contributions by many others). In such processes the quantum properties of nature can be neglected, although sometimes taken into account phenomenologically, as is the case with friction, for example.

On the atomic scale, classical physical theory has to be replaced by quantum theory to achieve consistency with experiments. In the atoms, the strong electromagnetic interactions binds the electrons to the nucleus, and gives rise to discrete energy levels with splitting of the order of the Rydberg energy 13.6 eV [7]. Together with the Pauli principle, which states that two electrons cannot occupy the same quantum state, the large splitting between energy levels leads to the stability evident in the systematic appearance of the periodic table of elements [7].

Contrary to the localised nature of the electrons in atoms, the conduction electrons in metals and semiconductors are delocalised, and are associated with a particular wave motion in the material rather than a fixed position [19]. For a mesoscopic sample this can lead to observable interference effects that strongly influence the conduction properties. Due to the importance of quantum effects, the quantum nature of a material must therefore be properly accounted for in the mesoscopic regime.

2.1 Electrons in conductors

When atoms organise into the periodic structures found in crystalline solids, the atomic energy levels merge into bands where closely spaced energy levels are associated with different momenta. The number of energy levels in each band is proportional to the number of atoms in

the lattice [7]. The Pauli principle prevents two electrons from occupying the same quantum state, so in the ground state of the conductor all energy levels up to the Fermi energy E_F are filled.

In the simplest picture (the Drude model) electron conduction can be understood as the acceleration of free electrons by an electric field [7]. However, due to the Pauli principle, all electrons except the ones at the Fermi energy are trapped because of the filled energy levels above them. Thus, only the electrons at the Fermi energy participate in the transport.

Depending on the symmetries of the crystal, different bands may be separated by forbidden energy gaps, where there are no available electronic states. If such a band gap occurs right above the Fermi energy, it will hinder conduction, as an appreciable energy will have to be supplied to excite the electrons into the next band so that their momenta can change. A solid with a large band gap above the Fermi energy is called an insulator, while a solid where the band gap is small enough that electrons can be excited by thermal energies is called a semiconductor. In a metal there is no band gap at the Fermi level, so only tiny energies are needed to excite electrons into a state with non-zero momentum [19].

The band theory is a one-electron theory which strictly speaking is only justified when electron-electron interactions can be neglected. The interaction between a single electron and all other electrons and nuclei in the lattice are taken into account in an average way. One could therefore suspect that electron-electron interactions or other many-body effects would invalidate this single electron picture [20]. However, in many conductors the lifetimes of fundamental excitations are so long that they can in practice be treated as free quasi-particles that are in one-to-one correspondence with the original excitations [9]. This is the basic idea behind Fermi liquid theory, where interactions between the quasi-particles are suppressed due to constraints on the available phase space for the scattered particles imposed by the Pauli principle [20]. The quasi-particle picture of Fermi liquid theory applies to many metals and semiconductor system, but breaks down for example in one-dimensional conductors, where interactions are always strong [9].

2.2 Important length scales in mesoscopic physics

In quantum transport, a number of different length scales come into play. These different length scales are associated with different processes, and determine the types of interference that can be observed in quantum transport measurements.

The two most fundamental length scales associated with an electron in a crystalline material are the lattice constant a and the Fermi wave length λ_F . The lattice constant is determined by the bonds between lattice atoms and is typically only a few Å. In the terminology of quantum mechanics λ_F is the de Broglie wave length of the conduction electrons at the Fermi level – the length scale of the amplitude variations of the electrons' wave function. In metals, λ_F is typically comparable to the lattice constant [20], while it can reach tens of nanometres in semiconductors [11]. From classical wave theory we know that manifestations of the wave na-

ture through diffraction and interference requires physical dimensions (such as the slit width in a diffraction experiment) to be comparable in magnitude to the wave length. Since the Fermi wave length in metals is so small, quantum transport phenomena related to wave function interference is difficult to observe in such systems [9]. However, semiconductor systems where λ_F can be comparable to typical sample dimensions are ideal for the study of quantum transport.

A crucial length scale for quantum transport is the phase coherence length l_ϕ (or phase breaking length). This length is the distance over which an electron's wave function is adequately described by a one-particle Schrödinger equation [9]. For a simple free electron model in a static potential the Schrödinger equation is given by

$$i\partial_t\Psi(\mathbf{r}, t) = \mathcal{H}(\mathbf{r})\Psi(\mathbf{r}, t) = \left[\frac{(-i\hbar\nabla_{\mathbf{r}})^2}{2m} + V(\mathbf{r}) \right] \Psi(\mathbf{r}, t), \quad (2.1)$$

with general solution

$$\Psi(\mathbf{r}, t) = \psi(\mathbf{r})e^{iEt/\hbar}. \quad (2.2)$$

Interactions that lead to a breakdown of the single particle picture are usually associated with inelastic scattering events, where energy is transferred to or from the single electron system. If the energy E of the electron is unchanged, the properties of the system at two instances of time are related through a unitary evolution of the wave function determined by the Schrödinger equation. When the electron exchanges energy with its surroundings through inelastic scattering events, the evolution of the wave function will be different before and after the event. After many inelastic collisions the quantum mechanical phase of the electron is therefore randomised, and coherence is lost, a process known as dephasing [9]. If the sample dimensions L are much larger than l_ϕ , the system effectively behaves as a collection of $N = L/l_\phi \gg 1$ statistically independent subsystems. Observations on the scale of L are therefore given by the ensemble average of these N systems. Due to this self-averaging when L is much larger than l_ϕ interference effects associated with the wave nature of the electrons are averaged out on macroscopic scales [9, 21]. In this regime electron transport is best described as a diffusion of electrons across the sample, and the system is said to be in the diffusive regime. However, even in this regime some quantum effects can survive, most notably the weak localisation correction to the conductivity, in which the interference between time reverse electron paths at zero magnetic field gives an enhanced probability for back reflection [11]. Weak localisation is destroyed in a magnetic field, when the time reversal symmetry between the paths is broken.

The most important many-body processes in conducting materials are electron-phonon and electron-electron interactions. In the electron-phonon interaction the electron interacts with the quantised collective vibrational modes of the host lattice (called phonons since they are the carriers of sound in a solid). Lattice vibrations generally increase with temperature, and the electron-phonon interaction is therefore the dominant scattering mechanism at high temperatures (such as room temperature) [22]. At low temperatures, electron-electron interactions dominate the dephasing. The phase coherence length due to electron-electron interactions scales as $l_\phi \propto T^{-2}$ [9, 11], and it is therefore possible to create systems with very long phase coherence lengths by lowering the temperature. Phase coherence lengths in the micrometre range are common at liquid helium temperatures [9].

In a perfect lattice the potential is periodic, $V(\mathbf{r} + \mathbf{R}) = V(\mathbf{r})$, and the wave function of an electron is described by eigenfunctions of the form [20]

$$\psi_{n\mathbf{k}}(\mathbf{r}) = u_{n\mathbf{k}}(\mathbf{r})e^{i\mathbf{k} \cdot \mathbf{r}}. \quad (2.3)$$

Here n labels the band and the Bloch functions $u_{n\mathbf{k}}(\mathbf{r})$ have the same periodicity as the lattice. Impurities and lattice defects can destroy the periodicity, leading to scattering from one momentum state to another, $\mathbf{k} \rightarrow \mathbf{k}'$. The characteristic distance between such momentum scattering events is called the mean free path l_{mfp} , and decreases with increasing impurity density. When typical sample dimensions are much smaller than the mean free path, so that electrons can traverse the device without scattering, the system is said to be in the ballistic regime.

When $l_{\text{mfp}} \ll l_\phi$, which is possible at low temperatures, scattering off different impurities can interfere [9]. For a sample of characteristic dimension $L \ll l_\phi$ the impurity potential therefore creates a highly complex, but static, interference pattern. This gives each sample a unique signature which can be observed when the sample is subject to a magnetic field. When applying a magnetic field \mathbf{B} , the associated vector potential \mathbf{A} leads to a change in the phase of each trajectory through the sample, proportional to the line integral of \mathbf{A} along the trajectory [9]. Changing the magnetic field therefore modifies the overall interference pattern, as the phases associated with different trajectories are changed differently.

2.3 Scattering theory

A common task in quantum transport is to calculate the conductance pertaining to a specific geometry or mesoscopic device. To linear response, the relation between the currents and the voltages in a device connected to, say, three leads is given by

$$\begin{pmatrix} I_1 \\ I_2 \\ I_3 \end{pmatrix} = \begin{pmatrix} G_{11} & -G_{12} & -G_{13} \\ -G_{21} & G_{22} & -G_{23} \\ -G_{31} & -G_{32} & G_{33} \end{pmatrix} \begin{pmatrix} V_1 \\ V_2 \\ V_3 \end{pmatrix}. \quad (2.4)$$

Several formalisms exist that allow one to calculate the conductances $G_{\alpha\beta}$ while properly accounting for the quantum properties of the mesoscopic device in question. This chapter briefly outlines scattering theory, as developed by Landauer [23] and Büttiker [24], and later applied by numerous authors to various mesoscopic transport problems. Scattering theory is a convenient tool for studying noise and fluctuations in mesoscopic devices [25], and also provides the basis for random matrix theory (RMT), which gives insight into the universal properties of mesoscopic transport [26]. Scattering theory is useful at low temperatures, where inelastic processes like phonon scattering is of minor importance [11], although inelastic scattering can be modelled to a certain extent by introducing auxiliary reservoirs [11].

In scattering theory one distinguishes between three sections of the system: The reservoirs, the

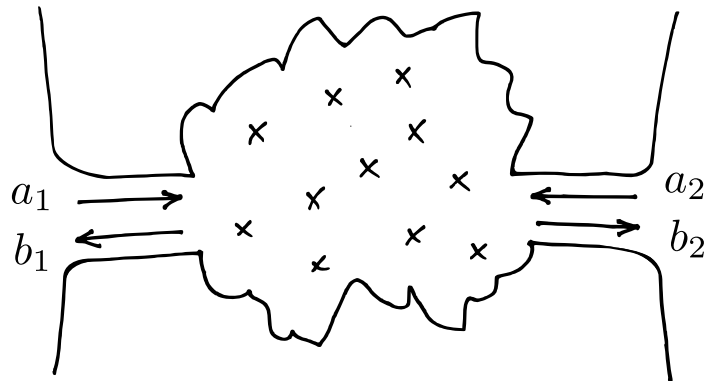


Figure 2.1: The elements of scattering theory. Carriers are injected from the reservoirs on the left and right into the mesoscopic scattering region in the centre via the narrow contacts. Each contact supports a number of modes which can be populated with carriers from the reservoirs. The modes are divided into incoming (a_i) and outgoing (b_i) according to the direction of propagation in the contact.

leads (or contacts),¹ and the scattering region, as illustrated in Fig. 2.1. The reservoirs act as electron sources and drains, and are characterised only by macroscopic quantities such as temperature, chemical potential, voltage, and possibly magnetisation. The leads are waveguides for electrons which connect the scattering region to the reservoirs [27]. Each lead supports a number of current carrying electron modes or channels. These discrete modes are a result of the transverse confinement of the electrons [11]. Electrons injected from a reservoir traverse the mesoscopic device without losing phase coherence. The electronic states are therefore most appropriately described in terms of scattering states, which represent an incoming electron in one mode and the resultant scattered waves in all other modes and leads [25]. Crucial to scattering theory is the assumption that there is no coherent back-reflection of electrons from the reservoirs to the leads. In other words, there is no phase-coherence between the electrons that are absorbed and emitted by the reservoir. This is equivalent to assuming that all energy dissipation occurs entirely in the reservoirs, *i.e.* that scattering inside the device is elastic [11].

The modes in each lead can be categorised as either incoming (towards the scattering region) or outgoing (towards the reservoir), depending on their direction of propagation in the lead. It is customary, as in Fig. 2.1, to denote incoming modes by the letter a and outgoing modes by letter b . The mode structure determines the available states that can be populated with electrons from the reservoir. The population of these states depend on the parameters of the reservoir. If the chemical potential in the reservoir is higher than the energy of the highest populated state in the lead, electrons are injected from the reservoir to the lead.

¹The words *lead* and *contact* are used somewhat inconsistently in the literature. Sometimes the distinction between the lead and the reservoir is not specified, and both words can refer to either to the lead, the reservoir, or sometimes both. In this thesis the word contact is always synonymous with lead, and both refer to the electron waveguide connecting the reservoir and the scattering region.

The description of the creation and annihilation of electrons in the leads is most conveniently described in the second quantisation picture of quantum mechanics. Following Ref. [25], we represent the annihilation and creation of an incoming electron in mode n of lead α at energy $\hbar\omega$ by the operators $\hat{a}_{\alpha n}(\omega)$ and $\hat{a}_{\alpha n}^\dagger(\omega)$, respectively. The total current in lead α is given by the difference between incoming and outgoing current due to all modes in that lead [28],

$$I_\alpha(t) = \sum_n I_{\alpha n}(t) = \frac{e}{h} \int d\omega d\omega' e^{i(\omega-\omega')t} \sum_n \left\langle \hat{a}_{\alpha n}^\dagger(\omega) \hat{a}_{\alpha n}(\omega') - \hat{b}_{\alpha n}^\dagger(\omega) \hat{b}_{\alpha n}(\omega') \right\rangle, \quad (2.5)$$

where $\langle \hat{o} \rangle$ denotes the thermal average of the operator \hat{o} . Intrinsic quantum states such as spin (and electron/hole nature in the case of superconductivity) are represented as separate modes. The scattering matrix relates the outgoing modes in lead α to the incoming modes in any other lead β [11, 25, 28]:

$$\hat{b}_{\alpha n}(\omega) = \sum_{\beta m} S_{\alpha n; \beta m}(\omega) \hat{a}_{\beta m}(\omega). \quad (2.6)$$

The scattering matrix \mathbf{S} (with elements $S_{\alpha n; \beta m}$) is unitary as a consequence of current conservation [11]. Using Eq. (2.6), the current in Eq. (2.5) can be expressed as

$$I_\alpha(t) = \frac{e}{h} \int d\omega d\omega' e^{i(\omega-\omega')t} \sum_n \sum_{\substack{\beta m \\ \beta' m'}} A_{\beta m; \beta' m'}^{\alpha n}(\omega, \omega') \left\langle \hat{a}_{\beta m}^\dagger(\omega) \hat{a}_{\beta' m'}(\omega') \right\rangle, \quad (2.7)$$

with

$$A_{\beta m; \beta' m'}^{\alpha n}(\omega, \omega') = \delta_{\beta\alpha} \delta_{mn} \delta_{\alpha\beta'} \delta_{m'n} - S_{\alpha n; \beta m}^*(\omega) S_{\alpha n; \beta' m'}(\omega'). \quad (2.8)$$

The population of a given incoming lead mode depends only on the adjacent reservoir, so [25, 28]

$$\left\langle \hat{a}_{\beta m}^\dagger(\omega) \hat{a}_{\beta' m'}(\omega') \right\rangle = \delta_{\beta\beta'} \delta_{mm'} \delta(\omega - \omega') f(\omega - eV_\beta), \quad (2.9)$$

where $f(\varepsilon) = [1 + \exp(\varepsilon/(k_B T))]^{-1}$ is the Fermi-Dirac distribution function. Combining Eqs. (2.7) and (2.9), the manifestly time-independent current becomes

$$I_\alpha = \frac{e}{h} \int d\omega \sum_\beta \bar{A}_\beta^\alpha(\omega) f(\omega - eV_\beta), \quad (2.10)$$

where

$$\begin{aligned} \bar{A}_\beta^\alpha(\omega) &\stackrel{\text{def.}}{=} \sum_{n,m} A_{\beta m; \beta m}^{\alpha n}(\omega, \omega) = \sum_{n,m} (\delta_{\beta\alpha} \delta_{mn} - S_{\alpha n; \beta m}^*(\omega) S_{\alpha n; \beta m}(\omega)) \\ &= \text{Tr} [\delta_{\beta\alpha} \mathbf{1}_\alpha - [\mathbf{S}^\dagger(\omega)]_{\beta\alpha} \mathbf{S}_{\alpha\beta}(\omega)], \end{aligned} \quad (2.11)$$

and the trace runs over all modes in α and β . To linear response, we can ignore the explicit voltage dependence in $\bar{A}_\beta^\alpha(\omega)$ [29], and the differential conductance becomes

$$(-1)^{\delta_{\alpha\beta}} G_{\alpha\beta} \stackrel{\text{def.}}{=} \frac{\partial I_\alpha}{\partial V_\beta} = \frac{e^2}{h} \int d\varepsilon \bar{A}_\beta^\alpha(\varepsilon + eV_\beta) \left(-\frac{\partial f(\varepsilon)}{\partial \varepsilon} \right) \quad (2.12)$$

At zero temperature the last factor reduces to $\delta(\varepsilon)$, and we find [29]

$$(-1)^{\delta_{\alpha\beta}} G_{\alpha\beta} = \frac{e^2}{h} \bar{A}_{\beta}^{\alpha}(eV_{\beta}) = \frac{e^2}{h} \text{Tr} [\delta_{\beta\alpha} \mathbf{1}_{\alpha} - [\mathbf{S}^{\dagger}(eV_{\beta})]_{\beta\alpha} \mathbf{S}_{\alpha\beta}(eV_{\beta})] \quad (2.13)$$

An example of this standard result is for a two terminal system such as that in Fig. 2.1. The scattering matrix

$$\mathbf{S} = \begin{pmatrix} r_{11} & t_{12} \\ t_{21} & r_{22} \end{pmatrix}, \quad (2.14)$$

is divided into block matrices describing transitions between the leads. The conductance of this system is [30]:

$$G_{21} = -\frac{\partial I_2}{\partial V_1} = \frac{e^2}{h} \text{Tr} [\mathbf{t}_{21}^{\dagger} \mathbf{t}_{21}] = \frac{2e^2}{h} \sum_n T_n, \quad (2.15)$$

where the T_n are the eigenvalues of the square matrix $\mathbf{t}_{21}^{\dagger} \mathbf{t}_{21}$, the so-called transmission eigenvalues. We have assumed spin degeneracy in the last step. Equation (2.15) is powerful result, since it applies to any strength of the scattering and any number of modes. Once the symmetries of the system are known, one can often find the distribution of transmission eigenvalues. The properties of both ballistic and diffusive conductors have been assessed in this way [26].

2.4 Spintronics and magnetism

In addition to charge, electrons also have an intrinsic quantum mechanical property called spin, which was postulated in 1925 by Goudsmit and Uhlenbeck to explain the experiments by Stern and Gerlach a few years earlier [7]. The spin is an axial vector quantity analogous to angular momentum. However, being of quantum nature the spin is quantised so that only two outcomes are possible in a spin measurement, $+\hbar/2$ (up or \uparrow) or $-\hbar/2$ (down or \downarrow), regardless of the direction of the measurement apparatus [7].

The spin degree of freedom leads to a whole range of interesting and complex phenomena in condensed matter physics. The most obvious manifestation is ferromagnetism, in which a large number of spins are frozen into alignment due to mutual interactions. The alignment arises due to the quantum mechanical exchange interaction, which is a consequence of the symmetry constraints imposed on the wave function pertaining to two indistinguishable quantum mechanical particles [19]. The exchange interaction can involve both localised and itinerant electrons, depending on the detailed interplay of the different energy levels and bands of the involved materials [19]. The mechanism leading to ferromagnetism is therefore to a certain extent materials dependent and quite complex, and the microscopic details are not fully understood even for metals [20].

Spintronics² is a branch of mesoscopic physics that aims to exploit not only the charge, but also the spin of the electron [22]. The discovery of the giant magnetoresistance (GMR) effect

²According to Žutić *et al.* [22], the name *spintronics* was invented by S. A. Wolf in 1996.

in the late 1980's [31, 32], where the resistance through a so-called spin valve can change dramatically depending on the orientation of two ferromagnets, was a major achievement in this field. The GMR effect, and later work on magnetic tunnel junctions, is the basic principle behind the magnetic read heads in modern hard disks [22]. The discoverers of the GMR effect, Albert Fert and Peter Grünberg, were awarded the Nobel Prize in Physics in 2007 [33].

There are two main problems that spintronics attempts to address [22]: (i) How do we efficiently induce and detect spin polarisation, and (ii) how long can a spin polarisation be preserved in a material?

In a non-magnetic metal or semiconductor, electrons with spin up and spin down contribute equally to the conductivity of the material, and the two spin populations can be treated as two parallel channels of conduction. In a ferromagnetic material, there is an excess of electrons with one spin, and we say that the material is spin polarised.

Spin polarisation can be induced in a non-magnetic material by shining circularly polarised light on the material. When the light is absorbed, the angular momentum associated with the polarised light can be transferred to the spin system, creating an imbalance between spin up and spin down electrons [22]. Furthermore, spin injection into a normal metal can also be realized by coupling it to a ferromagnetic reservoir. The spin polarisation inherent in the ferromagnet is then (partially) transferred to the normal conductor, with efficiency highly dependent on the nature of the conductors and the interface between them. It has proven difficult to inject polarised currents from a ferromagnetic metal into a semiconductor in this way, due to the mismatch of the resistances of the two materials [34]. This problem has been avoided either by using a ferromagnetic semiconductor instead of a metal, by using a highly polarised ferromagnet as the polarising material, or by inserting a tunnel barrier between the ferromagnet and the semiconductor [22].

In paper [1] we address question (i) above, proposing a way to induce spin polarisation in the non-ferromagnetic conductor graphene using a ferromagnetic insulator. The two-dimensional nature of graphene makes it viable to deposit such an insulator directly on top of the graphene sheet. Spin polarisation in graphene can then be induced by a strong exchange interaction between the localised spins in the insulator and the itinerant electrons in graphene.

The second question (ii) is concerned with over what length or time scales one can expect spin information to be preserved in a given system. If this information is lost, it becomes difficult to create spintronic devices with predictable behaviour. The loss of spin coherence is called spin relaxation, since in a normal conductor a polarisation will gradually relax towards the non-polarised state at equilibrium.

A number of different spin relaxation mechanisms exist [22]. Here I will only briefly mention the Elliott-Yafet (EY) and D'yakonov-Perel (DP) mechanisms, both of which are dependent on the combined action of momentum scattering and the spin orbit (SO) interaction. The EY and DP mechanisms are the important spin relaxation mechanisms for graphene [35].

The SO interaction is of relativistic origin, and couples the spin and the spatial motion of the electrons [7]. As a consequence, potential variations due to impurities, phonons or sample

boundaries can either induce transitions between different spin states (EY mechanism) or lead to a stabilisation of the spin ensemble (DP mechanism) [22]. Which mechanism dominates depends on various factors, such as band structure and temperature [22].

The EY mechanism stems from the fact that in the presence of the SO interaction, the electronic eigenstates are no longer pure spin up or spin down states, but rather superpositions of the two [22]. Assuming that an electron is found in a pure spin state immediately after a collision, the wave function evolves according to the Schrödinger equation after the collision, and the relative amplitude of its spin up and spin down character changes. When the electron is scattered again, it therefore has a finite probability of being found with the opposite spin, *i.e.* of undergoing a spin flip. Spin relaxation by the EY mechanism is characterised by proportionality between the momentum and spin relaxation rates, as a decrease in momentum scattering also leads to a decrease in spin relaxation [22].

The DP mechanism contributes in systems with broken inversion symmetry. In this case the SO gives rise to a momentum dependent effective magnetic field about which the spins precess between scattering events [22, 35]. Scattering randomly changes the momentum, and therefore also the direction and magnitude of the effective magnetic field. Provided scattering is sufficiently frequent, the spin precesses between each scattering by only a small angle proportional to the time between the momentum scattering events. Therefore, an increase in momentum scattering will lead on average to a *decrease* in the amount of change for the spin direction. It can be shown that this leads to an inverse proportionality between the spin and momentum scattering rates in the DP mechanism [22]

Paper [2] discusses spin transport in doped graphene, where both of the above mechanisms can contribute [35]. Due to the weak SO interaction in graphene, long spin relaxation times are expected. However, so far experiments have yielded relaxation times that are not much longer than in a normal two-dimensional electron gas (2DEG). Typical room temperature spin relaxation times in a GaAs-based 2DEGs are $\tau_s \approx 10 - 100$ ps [22], while the measured times in graphene are in the range $\tau_s \approx 100 - 200$ ps [36–38]. We confirm in paper [2] that spin transport in doped graphene is similar to that in a normal 2DEG with Rashba SO interaction [35], and find that in doped graphene the intrinsic SO coupling, which arises from intra-atomic processes, only contributes for large magnetic fields and is then completely masked by the Zeeman effect.

3 Two-dimensional electron gases

For the observation of quantum transport phenomena, semiconducting systems are advantageous over metals. The lower electron densities lead to longer Fermi wave lengths, so interference effects related to the quantum nature of the carriers are more easily observed [39].

Using a two-dimensional instead of a three-dimensional conductor has apparent benefits, since the transverse direction effectively becomes an extra dimension to “play with”. Apart from obvious geometrical advantages related to the ability to easily position gates and contacts, the two-dimensional structure is important for the observation of certain effects such as the quantum Hall effect (QHE), where the wave length of the quantum states under observation is tuned by a transverse magnetic field [39]. In weaker transverse magnetic fields it is also possible to study quantum ballistic transport in semiconductor 2DEGs via magnetic focusing of electrons injected through a quantum point contact [40].

This chapter describes the two most common realisations of two-dimensional electron gases today, namely by transverse confinement of electrons in semiconductor heterostructures or the electron gas found naturally in the two-dimensional crystal graphene.

3.1 Semiconductor heterostructures

A 2DEG can be artificially created by strong confinement in one direction (conventionally called the transverse direction or the z direction) of an ordinary electron gas found in a semiconductor.

When two semiconductors, or a semiconductor and an insulator, are brought into contact, the equilibration of charge between the two materials can lead to band bending which creates a narrow quantum well at the interface [39]. Due to the confinement in the well, a series of transverse energy bands are generated with energy separation determined by the inverse of the width of the well [9]. When the energy band separation is much larger than the thermal energy $k_B T$, only the lowest energy band will be relevant for conduction, and the electron gas in the well effectively behaves like a two-dimensional conductor. Low temperatures are generally required to perform such experiments [9, 39].

In several of the early works on two-dimensional transport the 2DEG was realised in a silicon metal-oxide semiconductor field effect transistor (MOSFET) by applying a relatively large voltage to a metallic gate separated from the silicon by an oxide layer [39]. This creates an inversion layer at the interface, acting as an effective quantum well. The quantum Hall effect,

which allows for very high accuracy measurements of several fundamental physical constants, was first observed in a silicon based 2DEG [14].

Today, 2DEGs are more commonly realised in semiconductor heterostructures [9], where a quantum well structure at the interface between two different semiconductors develops due to band bending because of a difference in band gap between the materials [39]. The most common heterostructure in use is GaAs/AlGaAs [9], but other combinations of semiconductor materials can also be used to tailor the properties for specific purposes. GaAs/AlGaAs heterostructures have the advantage over silicon MOSFET based 2DEGs that the lattice mismatch is minimal between the GaAs and the AlGaAs layers [9]. This reduces boundary scattering and leads to a dramatic increase in the mobility of the 2DEG compared to that usually observed in silicon MOSFET devices [39]. Using or adding other semiconducting materials can enhance specific properties. For example, indium can be used to tailor spin injection from a ferromagnetic metal into a 2DEG [41], or to enable good contact between the 2DEG and a superconductor [42]. Since the quantum well at the heterostructure interface relies only on the intrinsic band gaps of the materials, no external voltage has to be applied to generate the 2DEG in these materials [39]. Typical mobilities in a GaAs/AlGaAs 2DEG are in the range $10^2 - 10^4 \text{ cm}^2\text{V}^{-1}\text{s}^{-1}$ [39], but values up to $10^7 \text{ cm}^2\text{V}^{-1}\text{s}^{-1}$ have been reported [43, 44].

The low Fermi energy (low density of carriers) in a semiconductor 2DEG compared to a thin metallic film implies that the carriers have long Fermi wave lengths. Typically, the conduction electrons have $\lambda_F \sim 40 \text{ nm}$ in semiconductor 2DEGs [39]. Combined with the high mobilities that can be achieved, with mean free paths exceeding ten micrometres, this makes such 2DEGs ideally suited for the study of quantum transport [39]. Finally, by lateral confinement of the 2DEG using electrostatic gates one can create electron wave guides so as to study quasi one-dimensional quantum transport phenomena [39]. Several interesting quantum phenomena are related to the quantisation of transverse modes in such systems: conductance quantisation due to the onset of transverse modes, and universal conductance fluctuations due to the conductance quantum as the fundamental unit of conductance.

Recently, another two-dimensional conductor was realised in an atomically thin carbon layer known as graphene [45, 46]. The charge carriers in graphene are described by a two-dimensional Dirac-like Hamiltonian, leading to a linear dispersion relation resembling that of relativistic electrons. Consequently, several effects, such as the integer Quantum Hall effect and tunnelling, are qualitatively different from a regular 2DEG described by a non-relativistic Hamiltonian.

3.2 Graphene

Graphene was for the first time produced in 2004 by a research group at the University of Manchester, UK [47]. No thin film of atomic thickness was known to be electrically conducting or continuous at room temperature [47]. Although the experiment did not unequivocally prove that they had produced single layers of graphene, the following year the same group

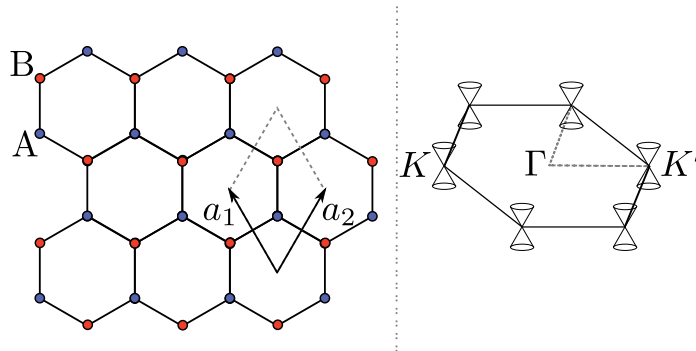


Figure 3.1: Hexagonal lattice and first Brillouin zone of graphene. (left) Graphene consists of a two-dimensional hexagonal lattice of carbon atoms. The hexagonal lattice can be viewed as two interleaved triangular lattices. Graphene’s pseudospin degree of freedom is associated with the weight of the electron wave function on either the A or B sublattice. (right) For low energy transport the dispersion relation can be expanded around the two inequivalent points K and K' , defining two inequivalent valleys. The dispersion relation of each valley has a conical shape, giving rise to the relativistic-like linear dispersion relation of the charge carriers.

[45, 48] and a group at Columbia University, New York, USA [46] reported successful experimental realisation and identification of graphene. The leading scientists of the Manchester group, A. Geim and K. Novoselov, were awarded the 2010 Nobel Prize for the discovery of graphene, only 6 years after the first publication [13].

The basic theory of graphene had been developed already in 1947 by Wallace [49] when he described graphite as weakly coupled layers of carbon atoms ordered in a hexagonal lattice. The two-dimensional hexagonal layer structure of carbon atoms is used as the conceptual basis for the description of both carbon nanotubes and fullerenes [50]. However, a general argument (the Mermin-Wagner theorem) suggested that no purely two-dimensional material would survive in the presence of thermal fluctuations [51, 52]. It was therefore assumed that graphene would be unable to exist in the free state, being unstable against the formation of soot, nanotubes, or fullerenes [47].

Producing graphene from high quality graphite was surprisingly simple [47]. Single or multiple layers from the graphite crystal can be extracted by mechanical exfoliation onto a piece of regular adhesive tape [48], colloquially known as the “Scotch tape trick”. The graphene layers are then deposited on a substrate for further experimental studies. The most difficult and time consuming part of the process is to detect and isolate the single layers. This process was greatly simplified by the observation that for a specific substrate thickness characteristic optical colour shifts due to interference could be used to distinguish between the different numbers of graphene layers [46, 50]. The presence of single layers of graphene can also be confirmed by correlating data from optical microscopy, scanning electron microscopy (SEM) and atomic-force microscopy (ATM) [45, 46]. Single and few layer graphene can also be

identified and distinguished from multi layer graphene by Raman spectroscopy [53].

In graphene, the carrier density can easily be varied over several orders of magnitude by the application of a back gate voltage [47]. The combination found in graphene of good electric conduction and a controllable doping through the electric field effect at room temperature was especially appealing as it had been sought after in thin metal films for a long time without success [47].

Graphene is one of few candidate materials for creating ballistic transistors, due to the fact that the mobility of graphene is high even at room temperature and with relatively high doping [50]. Although the highest mobilities that have been reported are at low temperature in suspended graphene [54, 55], the mobility of graphene on a substrate is generally found to be weakly dependent on temperature. This indicates that impurity scattering is the dominant scattering mechanism even at room temperature [47, 50], making graphene a promising material for probing ballistic transport [55, 56]. The mobility in graphene remains high even for low carrier densities, in contrast to the behaviour of semiconductor 2DEGs where the mobility decreases when the density is lowered [55]. High room temperature mobilities for graphene on a substrate have been achieved by screening the substrate impurities using ionic solvents [57]. The question of the dominant scattering mechanism limiting the mobility in graphene has not been conclusively settled [58]. Charged impurity scattering is the most probable mechanism, although scattering due to the intrinsic corrugations of the graphene sheets is also a possible explanation [58, 59].

Graphene can be characterised as a zero-gap semiconductor [50], where the valence and conduction bands touch at two inequivalent points in the Brillouin zone. Transport in graphene can be adequately described by a tight-binding model taking into account nearest neighbour hopping between the carbon atoms [49, 60]. Conduction properties are determined by the π and π^* bands, arising from the finite overlap of the predominantly out-of-plane $2p_z$ orbitals in carbon [61]. The σ bands, which arise from the sp^2 hybridised $2s$, $2p_x$, and $2p_y$ orbitals, play a minor role for the conduction properties, as they are well separated from the Fermi energy [62]. In undoped graphene, the π and π^* bands exactly touch at certain symmetry points in the Brillouin zone. These points are called the Dirac points, since the effective Hamiltonian found by expanding the dispersion relation around these points resembles the Hamiltonian of two-dimensional Dirac electrons [63–65],

$$H = v\boldsymbol{\sigma} \cdot \hat{\boldsymbol{p}} + V(\boldsymbol{r}). \quad (3.1)$$

Here $\hat{\boldsymbol{p}} = -i\hbar\nabla + e\boldsymbol{A}(\boldsymbol{r})$ is the momentum operator, and the pseudospin operators $\boldsymbol{\sigma}$ are Pauli matrices associated with the sublattice and valley space (see Fig. 3.1). The Fermi velocity $v \approx 10^6$ m/s is independent of energy, and can be determined from *ab initio* calculations or measured directly [45, 61, 66].

The eigenstates in graphene have a definite chirality associated with the eigenvalues of the operator $\boldsymbol{\sigma} \cdot \boldsymbol{p}/p$, analogous to the chirality inherent in the relativistic Dirac theory [67]. However, in graphene the chirality is not coupled to the electron spin, but rather to the pseudospin arising from the directionally dependent amplitude of a given momentum state on each of the

two sublattices [50]. The chirality of the charge carriers manifests itself in peculiar tunnelling properties, named Klein tunnelling after a related effect in relativistic quantum theory [67]. Contrary to the behaviour of electrons in a regular 2DEG, where the transmission probability T through a potential barrier decays exponentially with the length of the barrier, the chiral Dirac fermions in graphene can tunnel through a barrier with absolute certainty ($T = 1$) for certain angles, most notably in the forward direction. The conservation of chirality for potentials that are smooth on the scale of the lattice constant leads to a strict suppression of backscattering. An important implication of this Klein tunnelling property is that the Dirac fermions in graphene cannot be confined by an electrostatic potential [67]. However, boundary scattering which is naturally abrupt on the scale of the lattice constant does of course provide confinement. Due to the analogies between carriers in graphene and relativistic electrons, it has been suggested that the material could be used as a means to perform quantum electrodynamics experiments in a solid state environment [68].

As a consequence of the Dirac-like spectrum, the integer QHE in graphene is qualitatively different from that in a normal 2DEG described by non-relativistic quantum theory. The QHE filling factor is shifted by half an integer compared to the normal case [46], and most notably, the QHE in graphene has been observed at room temperature, while the observation of this effect normally requires liquid-helium temperatures [69].

Numerous applications have already been suggested for graphene [50]. The material is a very attractive candidate for electronics due to high mobilities which are not significantly affected by doping [50]. Transistor functionality at room temperature has already been demonstrated in graphene based quantum dots, that were created by carving out the desired geometry in a single graphene sheet [70]. Few layer graphene devices that respond to the absorption of single molecules have been demonstrated, making graphene interesting for use as a solid state gas detector [58]. Strains alter the hopping amplitude between neighbouring carbon atoms and thereby induce changes in the conduction properties. This feature makes graphene interesting for applications of graphene in mechanical transducers [71].

Graphene is also a promising material for spintronics. The low atomic number of carbon is expected to give a weak SO coupling [62, 72, 73], and hence long spin relaxation lengths [66, 74]. However, the spin relaxation found in experiments [36–38, 74, 75] is much stronger than the theoretical estimates [35, 76]. The discrepancy might be due to the role of the disorder [76], with experiment indicating that the dominant mechanisms need not be the same for momentum and spin relaxation [75]. The strength of the SO coupling in graphene and its role for spin relaxation is also still subject to debate [77].

Paper [1] discusses the possibility of inducing a large spin polarisation in graphene by means of contact with a ferromagnetic insulator. In a series of experiments where ferromagnetic insulators based on europium were coupled to superconducting aluminium, it was found that the itinerant electrons in the superconductor experienced a large exchange splitting [78–80]. The effect was attributed to a finite overlap of the wave function of the localised moments and the itinerant electrons in the metal [81]. The wave function of the itinerant electrons in thin films of Al is expected to have an atomic-like character in the transverse direction [82]. A very attractive feature of graphene is that one can easily contact it to other materials by

direct deposition on top of the graphene sheet. The bands relevant for electronic transport in graphene arise from electrons in the $2p_z$ orbital of the carbon atom [49], which are expected to have a similar spatial range as that of electrons in Al [1]. Based on these observations, we estimate in paper [1] that a ferromagnetic insulator as that used in the experiments of Refs. [78–80] can lead to a strong exchange splitting experienced by the charge carriers in graphene. Inducing a comparable Zeeman splitting by means of an external magnetic field would require strong fields of the order $10 - 20$ T.

As previously stated, in the lowest order the σ bands do not contribute to electronic transport in graphene. However, if the atomic SO of carbon is taken into account, second order intra-atomic processes involving the σ bands will lead to an effective intrinsic SO interaction in graphene [62, 73]. Also, if inversion symmetry of the graphene layer is broken, a Rashba-like extrinsic SO interaction arises [72]. The inversion symmetry can be broken by applying an electric field transverse to the graphene plane or by bending of the graphene layer [62]. Initial estimates [62, 73] of the SO coupling constants suggested that the extrinsic mechanism would be dominant [35]. This was recently challenged by a first principles calculation, which found that the two mechanisms would be comparable [77].

In paper [2] we study the spin dynamics in doped graphene in the presence of both types of SO interactions, including the effect of a transverse magnetic field. We show that at high doping the extrinsic SO creates a non-vanishing momentum dependent magnetic field in the plane, analogous to the Rashba SO interaction in normal 2DEG. At high doping, the intrinsic SO coupling of graphene only contributes at large magnetic fields, and will then be masked by the Zeeman effect.

4 Crossed Andreev reflection

Building computers capable of exploiting the quantum properties of nature has been on the wish list of scientist and engineers for a long time [83]. A computer that could invoke the superposition principle of quantum mechanics would have access to modes of computation which could vastly outperform classical logic devices, simultaneously performing the equivalent of a large number of classical computations [83]. Quantum computation algorithms have been developed for solving certain problems exponentially faster [84] or factor large numbers much more efficiently [85] than is possible on a classical computer. An implementation of these algorithms on a quantum computer could invalidate or seriously reduce the usefulness of current computer cryptography schemes. Efficient simulation of quantum systems is another field where a quantum computer would provide a huge gain [83]. This becomes especially important as materials are increasingly being tailored to specific applications even down to the mesoscopic scale.

Two crucial properties of quantum mechanics are of particular interest for quantum computing, namely *the superposition principle* and *entanglement*. The former was discussed the previous chapters, while this section gives a brief introduction to the latter. In an entangled state two (or more) quantum particles have become intertwined in such a way that measuring the state of one particle has immediate consequences for measurements done on the other. For a very readable introduction to entanglement, see Alain Aspect's introduction to the book [86], which also contains Bell's insightful paper [87] discussing the measurable consequences of quantum versus classical correlations.

In classical physics, nothing travels faster than the speed of light. It is therefore slightly surprising that quantum mechanics seems to provide us with processes where spatially well separated particles can immediately "sense" the behaviour of other particles. This entanglement is an immediate consequence of the non-locality of quantum theory, by which in principle the entire state of the universe should be simultaneously accounted for. However, as our daily experience tells us, the influence of an individual electron in Antarctica on the atoms in Europe is so small that it can safely be ignored. However, under certain circumstances where two particles have been brought close enough to interact, their properties can become coupled together in such a way that they cannot any more be thought of as separate particles [86]. Entanglement does not in fact break the causality demanded by classical physics, since entangled particles can only be made by first bringing the particles close enough to interact. Furthermore, the correlations between measurements made on the two particles can only be detected by comparing the measured results. This comparison requires a classical communication link [86].

As an illustration of entanglement, consider two electrons at positions labelled 1 and 2. The

superposition principle states that the total spin state of the compound system of two electrons is given by a linear combination of the tensor product $|s_1 s_2\rangle = |s_1\rangle \otimes |s_2\rangle$, where $|s_i\rangle$ is the state where the electron at i has spin $s_i \in \{\uparrow, \downarrow\}$. The total spin state of the two-electron system must therefore be of the form

$$|\psi_{12}\rangle_{\text{spin}} = c_{\uparrow\uparrow} |\uparrow\uparrow\rangle + c_{\uparrow\downarrow} |\uparrow\downarrow\rangle + c_{\downarrow\uparrow} |\downarrow\uparrow\rangle + c_{\downarrow\downarrow} |\downarrow\downarrow\rangle = \sum_{s_1, s_2} c_{s_1 s_2} |s_1 s_2\rangle. \quad (4.1)$$

This exhausts all possible combinations of the two spins. The absolute squares of each amplitude is the probability to measure that particular combination of spins, *i.e.* $|c_{\uparrow\uparrow}|^2$ is the probability that electron 1 is measured to have spin \downarrow and electron 2 to have spin \uparrow simultaneously. The interpretation of $|c_{\uparrow\uparrow}|^2$ as probabilities leads to the constraint that the sum of squares of the amplitudes add to 1. The value of each amplitude is determined by the initial conditions that are imposed on the two-electron system.

The states $|s_1 s_2\rangle$ above can be traded for any another complete set of quantum states. For the two-spin system a useful set is

$$|\psi_{12}\rangle_{\text{spin}} = a_0 \frac{(|\uparrow\downarrow\rangle - |\downarrow\uparrow\rangle)}{\sqrt{2}} + b_{1,-1} |\downarrow\downarrow\rangle + b_{1,0} \frac{(|\uparrow\downarrow\rangle + |\downarrow\uparrow\rangle)}{\sqrt{2}} + b_{1,+1} |\uparrow\uparrow\rangle. \quad (4.2)$$

Due to the way spins (and angular momenta in general) are added in quantum mechanics, the state corresponding to a_0 has total spin 0 and is known as the singlet state of the two-spin system. The three states corresponding to the b 's all have total spin \hbar , are normally degenerate in energy and are therefore known as the triplet states.

Suppose that we have somehow prepared our two-spin system in the singlet state, *i.e.* all the b 's in Eq. (4.2) are zero. If the two electrons in the singlet state are now spatially separated from each other, *e.g.* by separating them into separate electrical contacts, a peculiar situation arises. If the spin of electron 1 is measured to be \uparrow (for example by detection with a ferromagnet), we know immediately that electron 2 will have spin \downarrow when measured. This phenomenon is known as entanglement, and has no classical analogue. In classical physics, entities always interact locally or subject to constraints given by the propagation of light (which is the maximum speed with which information can travel).

Entanglement has been observed with photons, but has so far not been observed with massive electrons, due to the difficulty of combined creation and detection of electron entanglement in a solid state environment [88, 89]. However, the long spin dephasing times seen in semiconductors has led to the proposal of using such materials for the detection of electron entanglement [88, 89]. Two promising schemes for the generation of spin entangled electron pairs are with quantum dots [90], or using a superconductor [89]. In the first proposal an effective exchange interaction will couple electrons on two nearby quantum dots, so that the spin state of the two-electron system is of the singlet type [90].

The use of a superconductor in a solid state entangler relies on exploiting the natural spin entanglement of the Cooper pairs in a singlet superconductor to generate spatially correlated electrons in two normal conductors [89]. This is the topic of the last two papers [3, 4] of this thesis. The rest of this chapter therefore gives an introduction to the associated physics.

4.1 Superconductivity

Superconductivity is possibly the physical phenomenon which most strikingly displays the quantum nature of materials. At a certain material dependent (low) critical temperature T_c , the system undergoes a phase transition into a state where a weak attractive interaction between the electrons leads to the formation of bound pairs, called Cooper pairs [91]. In conventional superconductors, the attractive interaction between the electrons is mediated by the electron-phonon interaction [92]. The Cooper electron pairs have bosonic character, *i.e.* they easily condense into the same quantum state [93]. This leads to the hallmark effects associated with superconductivity: dissipation-less currents and the Meissner effect [92].

Superconductivity was discovered experimentally in 1911 by Kamerlingh Onnes [94], and although phenomenological theories were able to explain important properties of superconductors such as the Meissner effect [95, 96] and the correct scaling behaviour near the phase transition at T_c [97], it took almost half a century before a satisfactory microscopic theory was developed by Bardeen, Cooper and Schrieffer (BCS) [98]. The BCS theory brought great insight into the microscopic mechanisms behind superconductivity, and is one of the most important early applications of many-body quantum theory to a condensed matter problem [99].

Superconductors that can be described by BCS theory are called conventional superconductors, and are usually elemental metals such as mercury, tin, lead, or aluminium. The transition temperature is typically below 10 K for these superconductors [93], and the phase transition to the superconducting phase is usually first order (abrupt). In contrast, unconventional superconductors are not very well described by BCS theory [93]. These superconductors, which include the high T_c superconductors discovered in 1986 [100] and later, are usually characterised by a second order (smooth) phase transition to the superconducting state [92]. High T_c superconductivity is normally found in compound materials like alloys or ceramics.

A superconductor can be understood as a system where quantum mechanical phase coherence of the bosonic Cooper pairs is maintained over macroscopic distances [92]. The system has a minimal uncertainty in the quantum mechanical phase, trading it for a high uncertainty in the number of particles [92]. The superconducting coherence length ξ characterises the maximal separation of the quasi-particles bound in a Cooper pair, with typically $\xi \sim 10 - 100$ nm for many superconductors [101]. In most conventional superconductors, a spin-singlet state for the Cooper pair is energetically favoured [9, 102].

The important part of the mean field BCS Hamiltonian can be written compactly as [103]

$$\hat{H} = \int d\mathbf{r} \check{\Psi}_{\uparrow}^{\dagger}(\mathbf{r}) \check{\mathcal{H}}(\mathbf{r}) \check{\Psi}_{\uparrow}(\mathbf{r}) = \int d\mathbf{r} \check{\Psi}_{\uparrow}^{\dagger}(\mathbf{r}) \begin{bmatrix} \mathcal{H}(\mathbf{r}) & \Delta(\mathbf{r}) \\ \Delta^*(\mathbf{r}) & -\mathcal{H}^*(\mathbf{r}) \end{bmatrix} \check{\Psi}_{\uparrow}(\mathbf{r}), \quad (4.3)$$

where $\mathcal{H}(\mathbf{r})$ is the normal state single particle Hamiltonian, and the field operator is [104]

$$\check{\Psi}(\mathbf{r}) = \begin{pmatrix} \hat{\psi}_{\uparrow}(\mathbf{r}) \\ \hat{\psi}_{\downarrow}^{\dagger}(\mathbf{r}) \end{pmatrix}. \quad (4.4)$$

The pair potential $\Delta(\mathbf{r})$ is proportional to the effective attractive electron-electron interaction $V(\mathbf{r})$, typically arising from electron-phonon interactions [93], and is defined as

$$\Delta(\mathbf{r}) = V(\mathbf{r}) \langle \hat{\psi}_{\downarrow}(\mathbf{r}) \hat{\psi}_{\uparrow}(\mathbf{r}) \rangle. \quad (4.5)$$

In systems with only one superconductor, the phase of $\Delta(\mathbf{r})$ is rendered irrelevant by gauge invariance, and the pair potential can be treated as a real variable [105, 106].

The formulation in Eq. (4.3) describes the superconducting system as a set of non-interacting quasi-particles obeying the Bogoliubov-de Gennes (BdG) equations,

$$\begin{bmatrix} \mathcal{H}(\mathbf{r}) & \Delta(\mathbf{r}) \\ \Delta^*(\mathbf{r}) & -\mathcal{H}^*(\mathbf{r}) \end{bmatrix} \begin{pmatrix} u(\mathbf{r}) \\ v(\mathbf{r}) \end{pmatrix} = \epsilon \begin{pmatrix} u(\mathbf{r}) \\ v(\mathbf{r}) \end{pmatrix}, \quad (4.6)$$

and is therefore suitable as a starting point for the scattering matrix description of transport in systems involving superconductivity [103, 106]. The quantities $u(\mathbf{r})$ and $v(\mathbf{r})$ describe, respectively, the electron-like and hole-like character of the quasi-particles, as can be seen by letting $\Delta(\mathbf{r}) \rightarrow 0$.

4.2 Basic processes in multiterminal devices containing a superconductor

The spin-singlet nature of the Cooper pairs in conventional superconductors make them attractive as a source for spin entangled electrons [89, 90]. A key requirement for a useful entangler is the ability to generate non-local correlations, *i.e.* the entangled electrons must be spatially separated. This can be achieved by contacting two (or more) non-superconducting conductors to a superconductor [107–109]. In this section we discuss the various conduction processes that can be expected in such a multiterminal device.

4.2.1 Andreev reflection

Andreev reflection (AR) is a process occurring at a normal–superconductor (NS) interface [110]. The process is especially important at subgap energies, where single electrons are prohibited entry into the superconductor, and thus no single electron transport from the normal to the superconducting side can occur.

As illustrated in Fig. 4.1, AR occurs when an electron from the normal contact N travels towards the NS interface at subgap energy $\epsilon < \Delta$. The electron can only enter the superconductor if an electron in the corresponding time reverse state (at energy $-\epsilon$ measured with respect to the Fermi level of the superconductor) is also transferred to the superconductor [106]. The two electrons then enter the superconducting condensate as a Cooper pair without exciting the superconductor. In AR, a total charge of $2e$ is therefore transferred from N to S

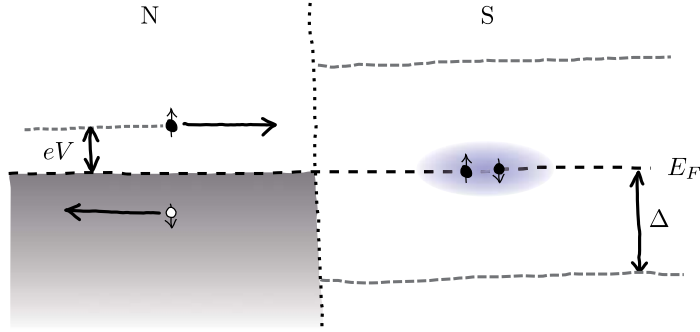


Figure 4.1: Schematic illustration of Andreev reflection (AR) at a normal-superconductor (NS) interface. An electron from the normal conductor N at energy $\epsilon = eV < \Delta$ can only enter the superconducting condensate if it manages to find another electron at energy $-\epsilon$ (below the Fermi level of the superconductor) to form a Cooper pair. The process leads to a hole being reflected on the normal side, hence the name Andreev reflection.

for each incident electron. The removal of the negative-energy electron on the normal side of the interface is equivalent to a back-reflected hole in N .

Since AR is an elastic scattering process (one single energy determines the scattering), the scattering matrix formalism can be applied. The scattering matrix in the presence of superconductivity has the general form in the extended electron-hole space [29]

$$\check{\mathbf{S}}(\epsilon) = \begin{pmatrix} \mathbf{S}^{ee}(\epsilon) & \mathbf{S}^{eh}(\epsilon) \\ \mathbf{S}^{he}(\epsilon) & \mathbf{S}^{hh}(\epsilon) \end{pmatrix}, \quad (4.7)$$

where the superscripts in $\mathbf{S}^{eh}(\epsilon)$ are used to indicate scattering from hole-like to electron-like states.

The leakage of electron-hole correlations into the normal conductor due to AR is called the superconducting proximity effect [111, 112]. There is also an inverse proximity effect, where the pair correlation is suppressed in a thin layer on the superconductor side of the NS junction. In the case of a superconductor coupled to a ferromagnetic conductor, AR will be suppressed on the ferromagnetic side due to the deficit of electrons of minority spin [113].

The description of the scattering process involving a superconductor simplifies if the normal scattering can be spatially separated from the AR process [114], as illustrated in Fig. 4.2. The scattering in the normal region is determined by the scattering matrix [115]

$$\check{\mathbf{S}}_N(\epsilon) = \begin{pmatrix} \mathbf{S}(\epsilon) & 0 \\ 0 & \mathbf{S}^*(-\epsilon) \end{pmatrix} = \begin{pmatrix} \mathbf{S}(\epsilon) & 0 \\ 0 & \bar{\mathbf{S}}(\epsilon) \end{pmatrix}, \quad (4.8)$$

which captures the fact that there is no intrinsic coupling between electron-like and hole-like states in the normal metal N . The notation $\bar{f}(\epsilon) \stackrel{\text{def.}}{=} f^*(-\epsilon)$ is used to denote time reversed quantities.

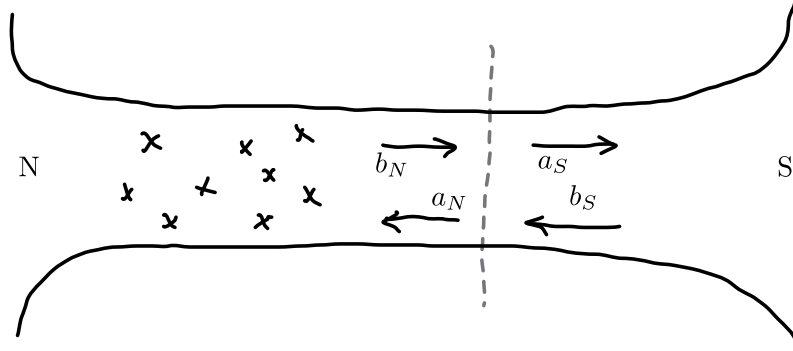


Figure 4.2: When normal scattering and Andreev reflection (AR) can be spatially separated, the scattering matrix in the presence of AR can be expressed in terms of the normal scattering matrix by identifying corresponding modes to the left and the right of the NS interface, as discussed in Ref. [114].

For subgap energies, $\epsilon < \Delta$, no single electrons can enter the superconductor, so AR is the only allowed scattering process. The scattering matrix associated with AR at the NS interface converts between electrons and holes without influencing the mode structure, so it can be written [29, 114, 115]

$$\check{S}_{\text{AR}}(\epsilon) = \begin{pmatrix} 0 & \nu \mathbf{1} \\ \nu \mathbf{1} & 0 \end{pmatrix}, \quad (4.9)$$

where the electron-hole conversion amplitude ν for subgap energies is¹ [29]

$$\nu = \frac{\epsilon}{\Delta} - i\sqrt{1 - \left(\frac{\epsilon}{\Delta}\right)^2}. \quad (4.11)$$

For energies close to the Fermi level, $\epsilon \rightarrow 0$, each AR leads to a phase shift of $-\pi/2$ due to the fact that $\nu \rightarrow -i$ [116]. At $\epsilon \gg \Delta$, the electron-hole conversion amplitude goes to zero, $\nu \rightarrow 0$, and we recover normal conduction.

Combining the scattering matrices in Eqs. (4.8) and (4.9) in a standard way by identifying corresponding modes on the two sides of the NS interface gives the following scattering matrix elements for the N side [29, 115]:

$$\mathbf{S}_{NN}^{ee} = \mathbf{r}_{NN} + \mathbf{t}_{NS}\nu\bar{\mathbf{r}}_{SS}\nu\mathbf{M}\mathbf{t}_{SN}, \quad (4.12)$$

$$\mathbf{S}_{NN}^{he} = \bar{\mathbf{t}}_{NS}\nu\mathbf{M}\mathbf{t}_{SN}, \quad (4.13)$$

¹There is a misprint in Eq. (14) of paper [3], the general expression should be [29]

$$\nu = \begin{cases} \frac{\epsilon}{\Delta} - \text{sign}(\epsilon)\sqrt{\left(\frac{\epsilon}{\Delta}\right)^2 - 1}, & |\epsilon| > \Delta, \\ \frac{\epsilon}{\Delta} - i\sqrt{1 - \left(\frac{\epsilon}{\Delta}\right)^2}, & |\epsilon| < \Delta. \end{cases} \quad (4.10)$$

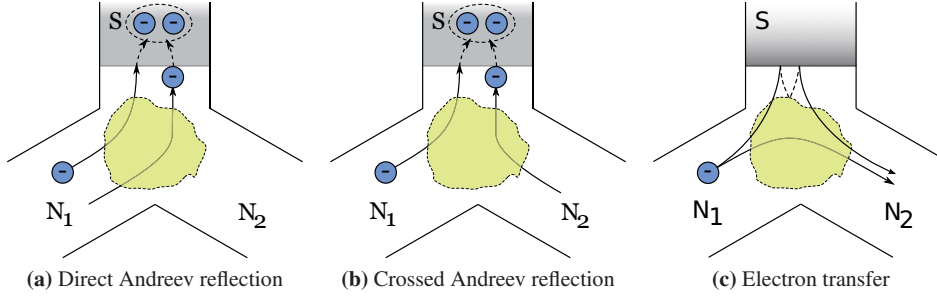


Figure 4.3: Basic transport processes in a multiterminal device with two normal metal contacts N_1 and N_2 and a superconducting contact S .

where the matrix

$$M = [\mathbf{1} - \nu r_{SS} \nu \bar{r}_{SS}]^{-1} \quad (4.14)$$

encodes the fact that AR must be taken into account to all orders at the NS interface. Using Eqs. (4.12) and (4.13) together with the unitarity of the scattering matrix, Beenakker [115] derived the following expression for the two terminal conductance of the NS junction in the presence of AR,

$$G_{NS}^{\text{AR}} = \frac{4e^2}{h} \sum_n \frac{T_n^2}{(2 - T_n)^2}. \quad (4.15)$$

Here T_n are the transmission eigenvalues associated with the normal state matrix $t_{1S}^\dagger t_{1S}$. This is the analogue of the standard formula of Eq. (2.15) for the conductance in a normal conductor when AR is taken into consideration.

From Eq. (4.15) it can be seen that for a good NS contact, in which the transmission eigenvalues of the M contributing modes are close to 1, the NS conductance doubles compared with the situation without a superconductor [105]:

$$G_{NS}^{\text{AR}} \approx \frac{4e^2}{h} \sum_{n=1}^M = \frac{4e^2}{h} M = 2G_N. \quad (4.16)$$

This doubling is due to the extra current carried by the Andreev reflected holes [106]. On the other hand, for a tunnel contact between N and S , the conductance (4.15) in the presence of a superconductor goes to zero faster than in the normal case, reflecting the vanishing density of states in the superconductor [117].

4.2.2 Crossed Andreev reflection

If two (or more) normal conductors are coupled to the superconductor, a non-local variant of AR can also occur in which the two electrons participating in AR originate from different

contacts. Non-local AR of this kind is called crossed Andreev reflection (CAR), and is key to using spin singlet superconductors as sources of entanglement [90].

A schematic illustration of CAR in a system with two normal contacts N_1 and N_2 and a superconductor S shown in Fig. 4.3. There are now two possible ways that AR can occur. If the two electrons involved in the production of a Cooper pair both originate from N_1 (Fig. 4.3a) the process is called direct Andreev reflection (DAR), or often simply AR. This process is analogous to regular AR occurring at a single NS interface, as discussed in Sec. 4.2.1. Alternatively, the two electrons can be taken from different contacts, N_1 and N_2 (Fig. 4.3b). This process, CAR, produces a current of incoming electrons in N_2 in response to the injected current in N_1 .

An important condition for observing CAR when the two normal contacts are connected directly to the superconductor is that contacts N_1 and N_2 must be closer than the superconducting coherence length ξ [108], the length scale over which the superconducting coherence between the electrons in the Cooper pair decays [118]. With direct contact between N_1 and N_2 , as in Fig. 4.3, CAR can be observed without this restriction.

4.2.3 Electron transfer

In a device with no direct contact between N_1 and N_2 , as considered by many previous works [107–109, 113, 119, 120], electrons can be transferred through the superconductor via a virtual excitation in the superconductor, a process known as electron co-tunnelling (EC) [108, 111]. While spin is conserved in EC, CAR requires the spin of the electron in N_2 to be opposite to that of the incoming electron from N_1 . The competition between CAR and EC can therefore be controlled by using ferromagnetic contacts [107, 119]. This was used experimentally by Beckmann *et al.* [113] to tune between CAR and EC by manipulating the relative magnetisation of two ferromagnets connected to the superconductor. With parallel alignment of the magnetisations, CAR is suppressed due to a deficit of minority spins for the spin singlet pairs. On the other hand, EC is suppressed for anti-parallel magnetisations [107, 119].

Calculations find that if both N_1 and N_2 are coupled to S by tunnel contacts, the contributions from CAR and EC will cancel exactly to linear response in the applied voltage [108]. At arbitrary coupling between the normal contacts and the superconductor, EC generally dominates CAR [111], although experiments demonstrate that CAR can also dominate [120, 121]. However, CAR domination only occurs beyond the regime of linear response, and theoretical suggestions suggest the effect could be due to either Coulomb interactions [101], the presence of an external AC bias [122], or quantum interference [123].

EC is of marginal relevance in geometries like those sketched in Fig. 4.3, where there is direct contact between N_1 and N_2 . Instead, the incoming electron in N_1 can be transferred to N_2 either directly or via multiple Andreev reflections at the superconductor in a more general process called electron transfer (ET), as sketched in Fig. 4.3c. As illustrated in Fig. 4.3c, ET competes with CAR by producing an outgoing electron current in N_2 in exactly the same way as EC. We find in papers [3, 4] that it is possible to have CAR dominated linear response transport when ET is suppressed.

4.3 Scattering formulation

The relative importance of CAR and ET can be analysed using a generalisation of the approach by Beenakker [115], as discussed in Sec. 4.2.1. For the device sketched in Fig. 4.3, the normal state scattering matrix which describes scattering in the non-superconducting (non-shaded) region of Fig. 4.3, can be written

$$\mathbf{S} = \begin{pmatrix} r_{11} & t_{12} & t_{1S} \\ t_{21} & r_{22} & t_{2S} \\ t_{S1} & t_{S2} & r_{SS} \end{pmatrix}. \quad (4.17)$$

Under assumptions similar to those leading to Eqs. (4.12) and (4.13), the non-local elements connecting N_1 and N_2 in the full scattering matrix of the three-terminal device, are

$$\mathbf{S}_{21}^{ee} = t_{21} + t_{2S}\nu\bar{r}_{SS}\nu\mathbf{M}t_{S1}, \quad (4.18)$$

$$\mathbf{S}_{21}^{he} = \bar{t}_{2S}\nu\mathbf{M}t_{S1}, \quad (4.19)$$

where, as before, $\mathbf{M} = [\mathbf{1} - \nu^2 r_{SS} \bar{r}_{SS}]^{-1}$ describes multiple back-reflection from the normal region to the superconductor with associated AR. The overbar notation denotes time reversal, as previously mentioned. At the Fermi level ($\epsilon = 0$), the normal scattering matrix fulfils $\bar{\mathbf{S}}_{ij} = \mathbf{S}_{ji}^\dagger$, where i, j are contact labels.

The non-local differential conductance between N_1 and N_2 , [124]

$$G_{21} = -\frac{\partial I_2}{\partial V_1} = G_{21}^{\text{ET}} - G_{21}^{\text{CAR}}, \quad (4.20)$$

can be expressed with the help of the scattering matrix by the relations [27, 105, 125]

$$G_{21}^{\text{ET}} = \text{Tr} \left[\mathbf{S}_{21}^{ee}(eV_1) \mathbf{S}_{21}^{ee\dagger}(eV_1) \right], \quad (4.21)$$

$$G_{21}^{\text{CAR}} = \text{Tr} \left[\mathbf{S}_{21}^{he}(eV_1) \mathbf{S}_{21}^{he\dagger}(eV_1) \right], \quad (4.22)$$

which can be derived as explained in Sec. 2.3. The negative sign for the CAR term in Eq. (4.20) reflects the fact that CAR induces an outgoing current in terminal N_2 , while ET produces an incoming current in N_2 . Inserting Eqs. (4.18) and (4.19), we get [3]

$$\begin{aligned} G_{21}^{\text{ET}} &= \text{Tr} \left[t_{21} t_{21}^\dagger \right] \\ &\quad + 2\text{Re} \text{Tr} \left[\nu^2 t_{2S} \bar{r}_{SS} \mathbf{M} t_{S1} t_{21}^\dagger \right] \\ &\quad + |\nu|^4 \text{Tr} \left[t_{2S} \bar{r}_{SS} \mathbf{M} t_{S1} t_{S1}^\dagger \mathbf{M}^\dagger \bar{r}_{SS}^\dagger t_{2S}^\dagger \right], \end{aligned} \quad (4.23)$$

$$G_{21}^{\text{CAR}} = |\nu|^2 \text{Tr} \left[\bar{t}_{2S} \mathbf{M} t_{S1} t_{S1}^\dagger \mathbf{M}^\dagger \bar{t}_{2S}^\dagger \right]. \quad (4.24)$$

These expressions illustrate the dependence the different processes involved in the transport on the electron-hole conversion amplitude ν . When AR is negligible, for example when $\epsilon \gg \Delta$,

the transport between N_1 and N_2 reduces to the first term in G_{21}^{ET} , which describes direct ET. However, for subgap energies $|\nu| = 1$ (see Eq. (4.11)), and both CAR and the processes in ET involving the superconductor contribute.

In paper [3] we find that a device which is symmetric in the normal state, such as the one shown in Fig. 4.3, will always be dominated by ET. However, it is possible to suppress ET in asymmetric devices, so that CAR dominated non-local transport can occur. We demonstrate ET suppression in paper [3] by engineering the geometry of the device. In paper [4] we show that one can also use a weak magnetic field to suppress ET and thereby achieve a clear CAR signal. The set-up proposed in paper [4] also has the benefit that the distance between N_1 and N_2 no longer has to be limited by the superconducting coherence length ξ [126], since the transport is not required to go through the superconductor as in the majority of earlier works. A somewhat similar set-up was proposed in Refs. [126, 127] where, however, a complicated dependence on quantum interference limits the possibility to distinguish between the signal due to AR and that due to quantum interference effects.

5 Conclusion

Transport in mesoscopic devices is a fascinating subject, due to the interplay between quantum and classical properties. It is also a field of research which is very close to applications, with current transistor technology operating with length scales of the same order that quantum effects are seen in experiments. The work in this thesis is concerned with two topics of general interest in the vast field of mesoscopic transport.

In papers [1] and [2], we study spin transport properties in graphene, a new and very promising two-dimensional carbon material. We find that spin polarisation can be induced in graphene using a ferromagnetic insulator [1]. In paper [2] we find that the spin-orbit coupling in highly doped graphene leads to behaviour similar to that found in a normal two-dimensional electron gas. The effect of the intrinsic spin-orbit coupling in graphene is dominated by the Zeeman effect at high doping. Since graphene was experimentally realized only six years ago, there is still much to be understood regarding the conduction properties of this material. Regarding spin transport in graphene, there is currently a discrepancy between theoretical and experimental results for the spin relaxation mechanism in graphene. Future work aimed at understanding the interplay of spin-orbit coupling and impurity scattering in graphene would therefore be of great value.

The second topic of this thesis is the use of superconducting correlations to create spatially separated spin entangled electron pairs. We have demonstrated in papers [3] and [4] the possibility of creating a detectable non-local signal between two normal contacts mediated by Andreev reflection (so called crossed Andreev reflection) in the linear response regime. Such a signal has previously only been detected at finite bias voltage. A natural next step from paper [4] would be to calculate the noise in the proposed set-up, as the broken time reversal symmetry due to the transverse magnetic field probably also modifies the noise spectrum.

Bibliography

- [1] H. Haugen, D. Huertas-Hernando & A. Brataas. *Spin transport in proximity-induced ferromagnetic graphene*. Phys. Rev. B **77**, 115406 (2008). doi:10.1103/PhysRevB.77.115406
- [2] H. Haugen & A. Brataas. *Spin transport in doped graphene* (2010). Unpublished manuscript.
- [3] H. Haugen, D. Huertas-Hernando, A. Brataas & X. Waintal. *Crossed Andreev reflection versus electron transfer in three-terminal graphene devices*. Phys. Rev. B **81**, 174523 (2010). doi:10.1103/PhysRevB.81.174523
- [4] H. Haugen, A. Brataas, G. E. W. Bauer & X. Waintal. *Focused crossed Andreev reflection* (2010). Submitted to Phys. Rev. Lett., arXiv:1007.4653
- [5] M. Alonso & E. J. Finn. *Physics* (Addison-Wesley, 1992). ISBN 0-201-56518-8
- [6] H. Goldstein, C. P. Poole & J. L. Safko. *Classical mechanics* (Addison Wesley, 2002). ISBN 0-201-65702-3
- [7] J. J. Brehm & W. J. Mullin. *Introduction to the structure of matter* (John Wiley & Sons, 1989). ISBN 0-471-60531-X
- [8] D. J. Griffiths. *Introduction to electrodynamics* (Prentice Hall, 1999)
- [9] H. Bruus & K. Flensberg. *Many-Body Quantum Theory in Condensed Matter Physics: An Introduction*. Oxford Graduate Texts (Oxford University Press, 2004). ISBN 0-19-856633-6
- [10] H. Haug & A. P. Jauho. *Quantum Kinetics in Transport and Optics of Semiconductors*, volume 123 of *Springer Series in Solid-State Sciences* (Springer-Verlag Berlin Heidelberg, 2008), 2nd edition. ISBN 978-3-540-73564-9. doi:10.1007/978-3-540-73564-9
- [11] S. Datta. *Electronic Transport in Mesoscopic Systems*. Number 3 in Cambridge Studies in Semiconductor Physics and Microelectronic Engineering (Cambridge University Press, 1997). ISBN 0521599431
- [12] Intel Corporation. *Intel to invest \$7 billion in U.S. manufacturing facilities [press release]*. <http://www.intel.com/pressroom/archive/releases/2009/20090210corp.htm> (10 February 2009). Accessed: 29 September 2010

- [13] *The 2010 Nobel Prize in Physics - Press Release*. Nobelprize.org (05 October 2010). URL http://nobelprize.org/nobel_prizes/physics/laureates/2010/press.html
- [14] K. v. Klitzing, G. Dorda & M. Pepper. *New method for high-accuracy determination of the fine-structure constant based on quantized hall resistance*. Phys. Rev. Lett. **45**, 494 (1980). doi:10.1103/PhysRevLett.45.494
- [15] D. C. Tsui, H. L. Stormer & A. C. Gossard. *Two-dimensional magneto-transport in the extreme quantum limit*. Phys. Rev. Lett. **48**, 1559 (1982). doi:10.1103/PhysRevLett.48.1559
- [16] R. B. Laughlin. *Anomalous quantum hall effect: An incompressible quantum fluid with fractionally charged excitations*. Phys. Rev. Lett. **50**, 1395 (1983). doi:10.1103/PhysRevLett.50.1395
- [17] G. J. Dolan & D. D. Osheroff. *Nonmetallic conduction in thin metal films at low temperatures*. Phys. Rev. Lett. **43**, 721 (1979). doi:10.1103/PhysRevLett.43.721
- [18] A. I. Ekimov & A. A. Onushchenko. *Quantum size effect in three-dimensional microscopic semiconductor crystals*. JETP Lett. **34**, 345 (1981)
- [19] S. Elliott. *The Physics and Chemistry of Solids* (John Wiley & Sons, 1998). ISBN 0-471-98195-8
- [20] N. W. Ashcroft & N. D. Mermin. *Solid State Physics* (Thomson Learning, London, UK, 1976). ISBN 0-03-083993-9
- [21] E. Akkermans & G. Montambaux. *Mesoscopic Physics of Electrons and Photons* (Cambridge University Press, 2007)
- [22] I. Žutić, J. Fabian & S. Das Sarma. *Spintronics: Fundamentals and applications*. Rev. Mod. Phys. **76**, 323 (2004). doi:10.1103/RevModPhys.76.323
- [23] R. Landauer. *Residual resistivity dipoles*. Z. Phys. B **21**, 247 (1975). doi:10.1007/BF01313304
- [24] M. Büttiker. *Four-terminal phase-coherent conductance*. Phys. Rev. Lett. **57**, 1761 (1986). doi:10.1103/PhysRevLett.57.1761
- [25] M. Büttiker. *Scattering theory of thermal and excess noise in open conductors*. Phys. Rev. Lett. **65**, 2901 (1990). doi:10.1103/PhysRevLett.65.2901
- [26] C. W. J. Beenakker. *Random-matrix theory of quantum transport*. Rev. Mod. Phys. **69**, 731 (1997). doi:10.1103/RevModPhys.69.731
- [27] M. Büttiker. *Scattering theory of current and intensity noise correlations in conductors and wave guides*. Phys. Rev. B **46**, 12485 (1992). doi:10.1103/PhysRevB.46.12485

- [28] Y. Tserkovnyak & A. Brataas. *Shot noise in ferromagnet–normal metal systems*. Phys. Rev. B **64**, 214402 (2001). doi:10.1103/PhysRevB.64.214402
- [29] G. B. Lesovik, A. L. Fauchère & G. Blatter. *Nonlinearity in normal-metal–superconductor transport: Scattering-matrix approach*. Phys. Rev. B **55**, 3146 (1997). doi:10.1103/PhysRevB.55.3146
- [30] M. Büttiker, Y. Imry, R. Landauer & S. Pinhas. *Generalized many-channel conductance formula with application to small rings*. Phys. Rev. B **31**, 6207 (1985). doi:10.1103/PhysRevB.31.6207
- [31] M. N. Baibich, J. M. Broto, A. Fert, F. N. Van Dau, F. Petroff, P. Etienne, G. Creuzet, A. Friederich & J. Chazelas. *Giant magnetoresistance of (001)fe/(001)cr magnetic superlattices*. Phys. Rev. Lett. **61**, 2472 (1988). doi:10.1103/PhysRevLett.61.2472
- [32] G. Binasch, P. Grünberg, F. Saurenbach & W. Zinn. *Enhanced magnetoresistance in layered magnetic structures with antiferromagnetic interlayer exchange*. Phys. Rev. B **39**, 4828 (1989). doi:10.1103/PhysRevB.39.4828
- [33] *The 2007 Nobel Prize in Physics - Press Release*. Nobelprize.org (9 October 2007). URL http://nobelprize.org/nobel_prizes/physics/laureates/2007/press.html
- [34] G. Schmidt, D. Ferrand, L. W. Molenkamp, A. T. Filip & B. J. van Wees. *Fundamental obstacle for electrical spin injection from a ferromagnetic metal into a diffusive semiconductor*. Phys. Rev. B **62**, 4790(R) (2000). doi:10.1103/PhysRevB.62.R4790
- [35] D. Huertas-Hernando, F. Guinea & A. Brataas. *Spin-orbit-mediated spin relaxation in graphene*. Phys. Rev. Lett. **103**, 146801 (2009). doi:10.1103/PhysRevLett.103.146801
- [36] N. Tombros, C. Józsa, M. Popinciuc, H. T. Jonkman & B. van Wees. *Electronic spin transport and spin precession in single graphene layers at room temperature*. Nature (London) **448**, 571 (2007). doi:10.1038/nature06037
- [37] N. Tombros, S. Tanabe, A. Veligura, C. Józsa, M. Popinciuc, H. T. Jonkman & B. J. van Wees. *Anisotropic spin relaxation in graphene*. Phys. Rev. Lett. **101**, 046601 (2008). doi:10.1103/PhysRevLett.101.046601
- [38] C. Józsa, T. Maassen, M. Popinciuc, P. J. Zomer, A. Veligura, H. T. Jonkman & B. J. van Wees. *Linear scaling between momentum and spin scattering in graphene*. Phys. Rev. B **80**, 241403 (2009). doi:10.1103/PhysRevB.80.241403
- [39] C. Beenakker & H. van Houten. *Quantum transport in semiconductor nanostructures*. In H. Ehrenreich & D. Turnbull (eds.) *Semiconductor Heterostructures and Nanostructures*, volume 44 of *Solid State Physics*, 1 (Academic Press, 1991). doi:10.1016/S0081-1947(08)60091-0

- [40] H. van Houten, C. W. J. Beenakker, J. G. Williamson, M. E. I. Broekaart, P. H. M. van Loosdrecht, B. J. van Wees, J. E. Mooij, C. T. Foxon & J. J. Harris. *Coherent electron focusing with quantum point contacts in a two-dimensional electron gas*. Phys. Rev. B **39**, 8556 (1989). doi:10.1103/PhysRevB.39.8556
- [41] H. X. Tang, F. G. Monzon, M. L. Roukes, F. J. Jedema, A. T. Filip & B. J. van Wees. *Semiconductor spintronics and quantum computation*, chapter Spin injection and transport in micro- and nanoscale devices, 35–95 (Springer Verlag, 2002). ISBN 9783540421764
- [42] S. Boulay, J. Dufouleur, P. Roche, U. Gennser, A. Cavanna & D. Mailly. *A reproducible process for mesoscopic superconducting indium contacts to GaAs/AlGaAs heterostructures*. J. Appl. Phys. **105**, 123919 (2009). doi:10.1063/1.3153983
- [43] L. Pfeiffer, K. West, H. Stormer & K. Baldwin. *Electron mobilities exceeding 10^7 cm²/Vs in modulation-doped GaAs*. Appl. Phys. Lett. **55**, 1888 (1989). doi:10.1063/1.102162
- [44] V. Umansky, R. de Picciotto & M. Heiblum. *Extremely high-mobility two dimensional electron gas: Evaluation of scattering mechanisms*. Appl. Phys. Lett. **71**, 683 (1997). doi:10.1063/1.119829
- [45] K. S. Novoselov, A. K. Geim, S. V. Morozov, D. Jiang, M. I. Katsnelson, I. V. Grigorieva, S. V. Dubonos & A. A. Firsov. *Two-dimensional gas of massless Dirac fermions in graphene*. Nature (London) **438**, 197 (2005). doi:10.1038/nature04233
- [46] Y. Zhang, Y.-W. Tan, H. L. Stormer & P. Kim. *Experimental observation of the quantum Hall effect and Berry's phase in graphene*. Nature (London) **438**, 201 (2005). doi:10.1038/nature04235
- [47] K. S. Novoselov, A. K. Geim, S. V. Morozov, D. Jiang, Y. Zhang, S. V. Dubonos, I. V. Grigorieva & A. A. Firsov. *Electric field effect in atomically thin carbon films*. Science **306**, 666 (2004). doi:10.1126/science.1102896
- [48] K. S. Novoselov, D. Jiang, F. Schedin, T. J. Booth, V. V. Khotkevich, S. V. Morozov & A. K. Geim. *Two-dimensional atomic crystals*. Proc. Natl. Acad. Sci. USA **102**, 10451 (2005). doi:10.1073/pnas.0502848102
- [49] P. R. Wallace. *The band theory of graphite*. Phys. Rev. **71**, 622 (1947). doi:10.1103/PhysRev.71.622
- [50] A. K. Geim & K. S. Novoselov. *The rise of graphene*. Nature Materials **6**, 183 (2007). doi:10.1038/nmat1849
- [51] A. Fasolino, J. H. Los & M. I. Katsnelson. *Intrinsic ripples in graphene*. Nature Materials **6**, 858 (2007). doi:10.1038/nmat2011

- [52] M. I. Katsnelson. *Graphene: carbon in two dimensions*. Materials Today **10**, 20 (2007). doi:10.1016/S1369-7021(06)71788-6
- [53] A. C. Ferrari, J. C. Meyer, V. Scardaci, C. Casiraghi, M. Lazzeri, F. Mauri, S. Piscanec, D. Jiang, K. S. Novoselov, S. Roth & A. K. Geim. *Raman spectrum of graphene and graphene layers*. Phys. Rev. Lett. **97**, 187401 (2006). doi:10.1103/PhysRevLett.97.187401
- [54] K. Bolotin, K. Sikes, Z. Jiang, M. Klima, G. Fudenberg, J. Hone, P. Kim & H. Stormer. *Ultrahigh electron mobility in suspended graphene*. Solid State Commun. **146**, 351 (2008). doi:10.1016/j.ssc.2008.02.024
- [55] X. Du, I. Skachko, A. Barker & E. Y. Andrei. *Approaching ballistic transport in suspended graphene*. Nature Nanotech. **3**, 491 (2008). doi:10.1038/nnano.2008.199
- [56] D. Gunlycke, H. M. Lawler & C. T. White. *Room-temperature ballistic transport in narrow graphene strips*. Phys. Rev. B **75**, 085418 (2007). doi:10.1103/PhysRevB.75.085418
- [57] F. Chen, J. Xia & N. Tao. *Ionic screening of charged-impurity scattering in graphene*. Nano Lett. **9**, 1621 (2009). doi:10.1021/nl803922m
- [58] F. Schedin, A. K. Geim, S. V. Morozov, E. W. Hill, P. Blake, M. I. Katsnelson & K. S. Novoselov. *Detection of individual gas molecules adsorbed on graphene*. Nature Materials **6**, 652 (2007). doi:10.1038/nmat1967
- [59] M. I. Katsnelson & A. K. Geim. *Electron scattering on microscopic corrugations in graphene*. Phil. Trans. R. Soc. A **366**, 195 (2008). doi:10.1098/rsta.2007.2157
- [60] J. C. Slonczewski & P. R. Weiss. *Band structure of graphite*. Phys. Rev. **109**, 272 (1958). doi:10.1103/PhysRev.109.272
- [61] S. Reich, J. Maultzsch, C. Thomsen & P. Ordejón. *Tight-binding description of graphene*. Phys. Rev. B **66**, 035412 (2002). doi:10.1103/PhysRevB.66.035412
- [62] D. Huertas-Hernando, F. Guinea & A. Brataas. *Spin-orbit coupling in curved graphene, fullerenes, nanotubes, and nanotube caps*. Phys. Rev. B **74**, 155426 (2006). doi:10.1103/PhysRevB.74.155426
- [63] D. P. DiVincenzo & E. J. Mele. *Self-consistent effective-mass theory for intralayer screening in graphite intercalation compounds*. Phys. Rev. B **29**, 1685 (1984). doi:10.1103/PhysRevB.29.1685
- [64] J. González, F. Guinea & M. A. H. Vozmediano. *The electronic spectrum of fullerenes from the Dirac equation*. Nucl. Phys. B **406**, 771 (1993). doi:10.1016/0550-3213(93)90009-E

- [65] N. H. Shon & T. Ando. *Quantum transport in two-dimensional graphite system*. J. Phys. Soc. Jpn. **67**, 2421 (1998). doi:10.1143/JPSJ.67.2421
- [66] A. H. Castro Neto, F. Guinea, N. M. R. Peres, K. S. Novoselov & A. K. Geim. *The electronic properties of graphene*. Rev. Mod. Phys. **81**, 109 (2009). doi:10.1103/RevModPhys.81.109
- [67] M. I. Katsnelson, K. S. Novoselov & A. K. Geim. *Chiral tunneling and the Klein paradox in graphene*. Nature Phys. **2**, 620 (2006). doi:10.1038/nphys384
- [68] G. W. Semenoff. *Condensed-matter simulation of a three-dimensional anomaly*. Phys. Rev. Lett. **53**, 2449 (1984). doi:10.1103/PhysRevLett.53.2449
- [69] K. S. Novoselov, Z. Jiang, Y. Zhang, S. V. Morozov, H. L. Stormer, U. Zeitler, J. C. Maan, G. S. Boebinger, P. Kim & A. K. Geim. *Room-temperature quantum hall effect in graphene*. Science **315**, 1379 (2007). doi:10.1126/science.1137201
- [70] L. A. Ponomarenko, F. Schedin, M. I. Katsnelson, R. Yang, E. W. Hill, K. S. Novoselov & A. K. Geim. *Chaotic dirac billiard in graphene quantum dots*. Science **320**, 356 (2008). doi:10.1126/science.1154663
- [71] V. M. Pereira & A. H. Castro Neto. *Strain engineering of graphene's electronic structure*. Phys. Rev. Lett. **103**, 046801 (2009). doi:10.1103/PhysRevLett.103.046801
- [72] C. L. Kane & E. J. Mele. *Quantum spin Hall effect in graphene*. Phys. Rev. Lett. **95**, 226801 (2005). doi:10.1103/PhysRevLett.95.226801
- [73] H. Min, J. E. Hill, N. A. Sinitsyn, B. R. Sahu, L. Kleinman & A. H. MacDonald. *Intrinsic and rashba spin-orbit interactions in graphene sheets*. Phys. Rev. B **74**, 165310 (pages 5) (2006). doi:10.1103/PhysRevB.74.165310
- [74] M. Popinciuc, C. Józsa, P. J. Zomer, N. Tombros, A. Veligura, H. T. Jonkman & B. J. van Wees. *Electronic spin transport in graphene field-effect transistors*. Phys. Rev. B **80**, 214427 (2009). doi:10.1103/PhysRevB.80.214427
- [75] K. Pi, W. Han, K. M. McCreary, A. G. Swartz, Y. Li & R. K. Kawakami. *Manipulation of spin transport in graphene by surface chemical doping*. Phys. Rev. Lett. **104**, 187201 (2010). doi:10.1103/PhysRevLett.104.187201
- [76] C. Ertler, S. Konschuh, M. Gmitra & J. Fabian. *Electron spin relaxation in graphene: The role of the substrate*. Phys. Rev. B **80**, 041405 (2009). doi:10.1103/PhysRevB.80.041405
- [77] M. Gmitra, S. Konschuh, C. Ertler, C. Ambrosch-Draxl & J. Fabian. *Band-structure topologies of graphene: Spin-orbit coupling effects from first principles*. Phys. Rev. B **80**, 235431 (2009). doi:10.1103/PhysRevB.80.235431

- [78] J. E. Tkaczyk & P. M. Tedrow. *Spin-polarized tunneling study of s - f exchange in superconductors*. Phys. Rev. Lett. **61**, 1253 (1988). doi:10.1103/PhysRevLett.61.1253
- [79] P. M. Tedrow, J. E. Tkaczyk & A. Kumar. *Spin-polarized electron tunneling study of an artificially layered superconductor with internal magnetic field: EuO-Al*. Phys. Rev. Lett. **56**, 1746 (1986). doi:10.1103/PhysRevLett.56.1746
- [80] X. Hao, J. S. Moodera & R. Meservey. *Thin-film superconductor in an exchange field*. Phys. Rev. Lett. **67**, 1342 (1991). doi:10.1103/PhysRevLett.67.1342
- [81] G. M. Roesler, M. E. Filipkowski, P. R. Broussard, Y. U. Idzerda, M. S. Osofsky & R. J. Soulen. *Epitaxial multilayers of ferromagnetic insulators with nonmagnetic metals and superconductors*. In I. Bozovic (ed.) *Superconducting Superlattices and Multilayers*, volume 2157 of *Proc. SPIE* (1994) 285
- [82] G. S. Painter. *Bonding of oxygen on aluminum: Relation between energy-band and cluster models*. Phys. Rev. B **17**, 662 (1978). doi:10.1103/PhysRevB.17.662
- [83] R. Feynman. *Simulating physics with computers*. Int. J. Theor. Phys. **21**, 467 (1982). doi:10.1007/BF02650179
- [84] D. R. Simon. *On the power of quantum computation*. In *Proceedings of the 35th Annual Symposium on Foundations of Computer Science* (IEEE Computer Society Press, 1994) 116–123. doi:10.1109/SFCS.1994.365701
- [85] P. W. Shor. *Algorithms for quantum computation: Discrete logarithms and factoring*. In *Proceedings of the 35th Annual Symposium on Foundations of Computer Science* (IEEE Computer Society Press, 1994) 124–134. doi:10.1109/SFCS.1994.365700
- [86] J. S. Bell. *Speakable and unspeakable in quantum mechanics: collected papers on quantum philosophy*. Collected papers on quantum philosophy (Cambridge University Press, 2004). ISBN 9780521523387
- [87] J. S. Bell. *On the Einstein Podolsky Rosen paradox*. Physics **1**, 195 (1964)
- [88] G. Burkard, D. Loss & E. V. Sukhorukov. *Noise of entangled electrons: Bunching and antibunching*. Phys. Rev. B **61**, R16303 (2000). doi:10.1103/PhysRevB.61.R16303
- [89] P. Recher, E. V. Sukhorukov & D. Loss. *Andreev tunneling, coulomb blockade, and resonant transport of nonlocal spin-entangled electrons*. Phys. Rev. B **63**, 165314 (2001). doi:10.1103/PhysRevB.63.165314
- [90] P. Recher & D. Loss. *Dynamical coulomb blockade and spin-entangled electrons*. Phys. Rev. Lett. **91**, 267003 (2003). doi:10.1103/PhysRevLett.91.267003
- [91] L. N. Cooper. *Bound electron pairs in a degenerate fermi gas*. Phys. Rev. **104**, 1189 (1956). doi:10.1103/PhysRev.104.1189

- [92] M. Tinkham. *Introduction to superconductivity* (McGraw-Hill, 1975). ISBN 0-07-064877-8
- [93] K. Fosheim & A. Sudbø. *Superconductivity: physics and applications* (John Wiley & Sons, 2004). ISBN 0-470-84452-3
- [94] H. Kamerlingh Onnes. *Further experiments with liquid helium. C. on the change of electric resistance of pure metals at very low temperatures etc. IV. the resistance of pure mercury at helium temperatures.* In *Proceedings*, volume 13 II of *Koninklijke Nederlandse Akademie van Wetenschappen* (1911) 1274–1276
- [95] W. Meissner & R. Ochsenfeld. *Ein neuer effekt bei eintritt der supraleitfähigkeit.* *Naturwissenschaften* **21**, 787 (1933). doi:10.1007/BF01504252
- [96] F. London & H. London. *The electromagnetic equations of the supraconductor.* *Proc. R. Soc. London, Ser. A* **149**, 71 (1935). doi:10.1098/rspa.1935.0048
- [97] V. L. Ginzburg & L. D. Landau. *On the theory of superconductivity.* *Zh. Eksp. Teor. Fiz.* **20**, 1064 (1950)
- [98] J. Bardeen, L. N. Cooper & J. R. Schrieffer. *Theory of superconductivity.* *Phys. Rev.* **108**, 1175 (1957). doi:10.1103/PhysRev.108.1175
- [99] G. D. Mahan. *Many-Particle Physics* (Kluwer Academic/Plenum Publishes, New York, 2000), 3rd edition. ISBN 0-306-46338-5
- [100] J. G. Bednorz & K. A. Müller. *Possible high t_c superconductivity in the ba-la-cu-o system.* *Z. Phys. B* **64**, 189 (1986). doi:10.1007/BF01303701
- [101] A. Levy Yeyati, F. S. Bergeret, A. Martín-Rodero & T. M. Klapwijk. *Entangled Andreev pairs and collective excitations in nanoscale superconductors.* *Nature Phys.* **3**, 455 (2007). doi:10.1038/nphys621
- [102] P. Anderson. *Theory of dirty superconductors.* *J. Phys. Chem. Solids* **11**, 26 (1959). doi:10.1016/0022-3697(59)90036-8
- [103] S. Datta & P. F. Bagwell. *Can the bogoliubov-de gennes equation be interpreted as a 'one-particle' wave equation?* *Superlattice. Microstruct.* **25**, 1233 (1999). doi:10.1006/spmi.1999.0747
- [104] Y. Nambu. *Quasi-Particles and gauge invariance in the theory of superconductivity.* *Phys. Rev.* **117**, 648 (1960). doi:10.1103/PhysRev.117.648
- [105] G. E. Blonder, M. Tinkham & T. M. Klapwijk. *Transition from metallic to tunneling regimes in superconducting microconstrictions: Excess current, charge imbalance, and supercurrent conversion.* *Phys. Rev. B* **25**, 4515 (1982). doi:10.1103/PhysRevB.25.4515

- [106] S. Datta, P. Bagwell & M. Anantram. *Scattering theory of transport for mesoscopic superconductors*. Technical report, School of Electrical and Computer Engineering, Purdue University, West Lafayette, IN 47907-1285. (1996). URL <http://docs.lib.purdue.edu/ecetr/107>
- [107] G. Deutscher & D. Feinberg. *Coupling superconducting-ferromagnetic point contacts by Andreev reflections*. Appl. Phys. Lett. **76**, 487 (2000). doi:10.1063/1.125796
- [108] G. Falci, D. Feinberg & F. W. J. Hekking. *Correlated tunneling into a superconductor in a multiprobe hybrid structure*. Europhys. Lett. **54**, 255 (2001). doi:10.1209/epl/i2001-00303-0
- [109] D. Feinberg. *Andreev scattering and cotunneling between two superconductor-normal metal interfaces: the dirty limit*. Eur. Phys. J. B **36**, 419 (2003). doi:10.1140/epjb/e2003-00361-6
- [110] A. F. Andreev. *Thermal conductivity of the intermediate state of superconductors*. Sov. Phys. JETP **19**, 1228 (1964)
- [111] J. P. Morten, A. Brataas & W. Belzig. *Circuit theory of crossed Andreev reflection*. Phys. Rev. B **74**, 214510 (2006). doi:10.1103/PhysRevB.74.214510
- [112] Y. V. Nazarov. *Circuit theory of andreev conductance*. Phys. Rev. Lett. **73**, 1420 (1994). doi:10.1103/PhysRevLett.73.1420
- [113] D. Beckmann, H. B. Weber & H. v. Löhneysen. *Evidence for crossed Andreev reflection in superconductor-ferromagnet hybrid structures*. Phys. Rev. Lett. **93**, 197003 (2004). doi:10.1103/PhysRevLett.93.197003
- [114] C. W. J. Beenakker. *Universal limit of critical-current fluctuations in mesoscopic Josephson junctions*. Phys. Rev. Lett. **67**, 3836 (1991). doi:10.1103/PhysRevLett.67.3836
- [115] C. W. J. Beenakker. *Quantum transport in semiconductor-superconductor microjunctions*. Phys. Rev. B **46**, 12841 (1992). doi:10.1103/PhysRevB.46.12841
- [116] C. W. J. Beenakker. *Quantum mesoscopic phenomena and mesoscopic devices in microelectronics*, volume 559 of *NATO science series*, chapter Why does a metal-superconductor junction have a resistance? (Kluwer Academic Publishers, 2000). ISBN 0-7923-6625-5. arXiv:cond-mat/9909293v2
- [117] I. Giaever. *Energy gap in superconductors measured by electron tunneling*. Phys. Rev. Lett. **5**, 147 (1960). doi:10.1103/PhysRevLett.5.147
- [118] F. W. J. Hekking & Y. V. Nazarov. *Subgap conductivity of a superconductor-normal-metal tunnel interface*. Phys. Rev. B **49**, 6847 (1994). doi:10.1103/PhysRevB.49.6847

- [119] R. Mélin & D. Feinberg. *Sign of the crossed conductances at a ferromagnet/superconductor/ferromagnet double interface*. Phys. Rev. B **70**, 174509 (2004). doi:10.1103/PhysRevB.70.174509
- [120] S. Russo, M. Kroug, T. M. Klapwijk & A. F. Morpurgo. *Experimental observation of bias-dependent nonlocal Andreev reflection*. Phys. Rev. Lett. **95**, 027002 (2005). doi:10.1103/PhysRevLett.95.027002
- [121] P. Cadden-Zimansky & V. Chandrasekhar. *Nonlocal correlations in normal-metal superconducting systems*. Phys. Rev. Lett. **97**, 237003 (2006). doi:10.1103/PhysRevLett.97.237003
- [122] D. S. Golubev & A. D. Zaikin. *Non-local Andreev reflection under ac bias*. Europhys. Lett. **86**, 37009 (2009). doi:10.1209/0295-5075/86/37009
- [123] D. S. Golubev, M. S. Kalenkov & A. D. Zaikin. *Crossed Andreev reflection and charge imbalance in diffusive normal-superconducting-normal structures*. Phys. Rev. Lett. **103**, 067006 (2009). doi:10.1103/PhysRevLett.103.067006
- [124] J. P. Morten, D. Huertas-Hernando, W. Belzig & A. Brataas. *Elementary charge transfer processes in a superconductor-ferromagnet entangler*. Europhys. Lett. **81**, 40002 (2008). doi:10.1209/0295-5075/81/40002
- [125] Y. Takane & H. Ebisawa. *Conductance formula for mesoscopic systems with a superconducting segment*. J. Phys. Soc. Jpn. **61**, 1685 (1992). doi:10.1143/JPSJ.61.1685
- [126] P. K. Polinák, C. J. Lambert, J. Koltai & J. Cserti. *Andreev drag effect via magnetic quasiparticle focusing in normal-superconductor nanojunctions*. Phys. Rev. B **74**, 132508 (2006). doi:10.1103/PhysRevB.74.132508
- [127] P. Rakytá, A. Kormanyos, Z. Kaufmann & J. Cserti. *Andreev edge channels and magnetic focusing in normal-superconductor systems: A semiclassical analysis*. Phys. Rev. B **76**, 064516 (2007). doi:10.1103/PhysRevB.76.064516

Paper [1]

Spin transport in proximity-induced ferromagnetic graphene

Physical Review B **77**, 115406 (2008)

Spin transport in proximity-induced ferromagnetic graphene

Håvard Haugen,* Daniel Huertas-Hernando, and Arne Brataas

Department of Physics, Norwegian University of Science and Technology, N-7491 Trondheim, Norway

(Received 27 July 2007; revised manuscript received 11 January 2008; published 5 March 2008)

Ferromagnetic insulators deposited on graphene can induce ferromagnetic correlations in graphene. We estimate that induced exchange splittings $\Delta \sim 5$ meV can be achieved by, e.g., using the magnetic insulator EuO. We study the effect of the induced spin splittings on the graphene transport properties. The exchange splittings in proximity-induced ferromagnetic graphene can be determined from the transmission resonances in the linear response conductance or, independently, by magnetoresistance measurements in a spin-valve device. The spin polarization of the current near the Dirac point increases with the length of the barrier, so that long systems are required to determine Δ experimentally.

DOI: 10.1103/PhysRevB.77.115406

PACS number(s): 72.25.-b, 73.23.Ad, 73.43.Jn

I. INTRODUCTION

The two-dimensional honeycomb lattice of graphene is a conceptual basis for describing carbon structures such as fullerenes, carbon nanotubes, and individual layers of graphite. The fabrication of free and stable monolayers of graphene a few years ago transformed this concept into an experimental reality that has attracted a tremendous interest from the research community.¹⁻³ The low energy excitations of charge carriers in graphene are similar to massless relativistic Dirac (or rather Weyl) particles. The Hamiltonian is^{4,5}

$$H = -i\hbar v \boldsymbol{\sigma} \cdot \nabla + U(\mathbf{r}), \quad (1)$$

where the velocity $v \approx 10^6$ m/s is the analog of the Dirac electron speed of light (in the sense of limiting velocity) in graphene and $\boldsymbol{\sigma} = (\sigma_x, \sigma_y)$ is a two-dimensional vector of Pauli matrices acting on two-spinor states related to the two triangular sublattices constituting graphene's honeycomb lattice. The approximate Hamiltonian (1) is valid near the Dirac points K and K' in the reciprocal lattice. The two inequivalent Dirac points introduce a twofold valley degeneracy.⁶

The carrier concentrations are typically in the range $10^{11} - 10^{12}$ cm⁻², corresponding to a Fermi wavelength of $\lambda_F \approx 50 - 100$ nm.^{3,7} The mean free path (mfp) has been reported to be of the order $l_{\text{mfp}} \approx 0.4$ μm .¹ With improved control over the fabrication process of graphene, we expect to see the realization of even cleaner samples with longer mean free paths.

Spintronics aim to inject, manipulate, and detect spins in electronic devices. Electrical spin injection in normal metals is routinely achieved by contacting ferromagnets like Fe, Ni, and Co with normal metals such as Cu and Al, and driving a current through the system. In semiconductors, electrical spin injection is more challenging because of the resistance mismatch between the semiconductor and possible ferromagnetic metal contacts.⁸ Nevertheless, spin injection into a semiconductor is feasible from a conventional ferromagnet when the interface resistance between the semiconductor and the ferromagnet is sufficiently large, as recently demonstrated by using Fe Schottky contacts in Ref. 9. Spin injection detected via the giant magnetoresistance effect in nanotubes contacted to ferromagnets has also been reported.¹⁰

Graphene is clearly an interesting candidate for spintronics applications since the carrier concentration can be controlled by gate voltages. Also, it has a very weak spin-orbit interaction, leading to the possibility of relatively long spin flip lengths.^{11,12} In a recent experiment on spin injection in single layer graphene, the spin flip (sf) length is found to be $l_{\text{sf}} \approx 1$ μm at room temperature in dirty samples.¹³ Cleaner samples are expected to have even longer spin flip lengths.

We explore another possibility of spin dependent transport by envisioning that graphene is put in close proximity to a magnetic insulator. Via the magnetic proximity effect, exchange splittings will be induced in graphene. Strong proximity induced exchange splittings due to ferromagnetic insulators have been observed at EuO/Al interfaces.¹⁴⁻¹⁶ The effect was attributed to the nonvanishing overlap between the wave functions of the localized moments in the magnetic insulator and the itinerant electrons in the metal.¹⁷ The electronic wave functions can be described by atomiclike wave functions at the surface of thin Al films.¹⁸ The spatial range is similar for the atomic wave functions in Al and graphene, so we expect the overlap between the localized moments and itinerant electrons in graphene at EuO/graphene interfaces to induce exchange interactions comparable to those observed for EuO/Al. Based on the results reported in Refs. 15-17 and 19, we roughly estimate that exchange splittings in graphene due to the ferromagnetic insulator EuO could be of the order of 5 meV (see Appendix A for details).

In this paper, we show that proximity-induced splittings can be observed in the tunneling conductance associated with a tunable barrier created by the ferromagnetic insulator gate on top of graphene. First, for highly doped barriers, we demonstrate that the splitting Δ can be directly observed from the transmission resonances in the conductance.^{7,20,21} Moreover, for low doping of the barrier, we show that the spin polarization of the tunneling current, directly related to the spin splitting Δ , increases with increasing length of the barrier. The spin polarization can be studied by magnetoresistance (MR) measurements in a spin-valve device where two magnetic gates are deposited in series. Such MR measurements could also allow us to independently determine the induced spin splitting Δ .

This paper is organized as follows: We present a model of a magnetic gate in Sec. II. Section III reminds the reader of the results obtained in Refs. 7 and 22 for the conductance of

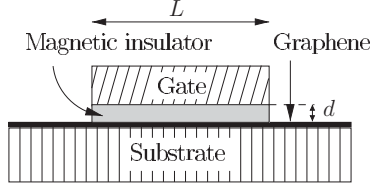


FIG. 1. A ferromagnetic insulator on top of graphene induces an exchange splitting in graphene. A metallic gate on top of the insulator controls the electrostatic potential.

a square barrier in graphene. Then we discuss how to obtain analytical expressions for the conductance both far from and close to the Dirac point. We extend the spinless situation to a spin dependent barrier with an exchange splitting Δ between the two spin channels in Sec. IV. First, we discuss the possibilities for extracting the splitting Δ directly from the conductance of a single highly doped barrier. Second, we study the dependence of the current spin polarization on the barrier height and length. Section V discusses the MR effect in a double barrier spin-valve device and discusses how it can be used to extract Δ . Finally, our conclusions are in Sec. VI.

II. MODEL

A possible way to construct a ferromagnetic gate is to deposit a magnetic insulator, such as EuO, on top of a graphene sample with a metallic gate above it (see Fig. 1). So far, experimental efforts have focused on depositing non-magnetic gates on graphene.^{23,24} The presence of a magnetic insulator will induce an exchange splitting in graphene. The normal metal gate allows us to control the Fermi level locally, i.e., to create a tunable barrier in graphene. In this way, both control of the charge and spin carrier concentrations can be achieved.

We assume in this paper that the normal metal gate induces a sharp potential barrier below it. This is a reasonable assumption provided the distance d between the gate and the graphene layer is much shorter than the Fermi wavelength λ_F , which is relatively long in graphene, $\lambda_F \approx 50-100$ nm.⁷ Recently, a method for manufacturing top gates where the distance from the gate to the graphene layer is of the order of λ_F has been demonstrated.²³ Observation of resonance effects due to sharp potential steps, therefore, seems feasible in graphene.

The exchange interaction between the localized magnetic moments in the ferromagnetic insulator and the spins of the electrons creates an additional spin dependent offset of the barrier potential, leading to the possibility of spin dependent tunneling. We estimate in Appendix A that the exchange splitting due to the magnetic insulator EuO can be around 5 meV. Here, we assume that the exchange interaction is not affected by the gate voltage of the top metallic gate.

III. TUNNELING PROBABILITY

For completeness, we first review the results for tunneling through a square barrier in graphene, and follow the deriva-

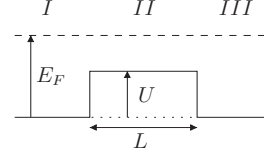


FIG. 2. Square barrier of length L .

tion in Refs. 7 and 22. We will later extend this discussion to a spin dependent barrier. The charge carriers we consider are Dirac quasiparticles, described by the Hamiltonian (1). These quasiparticles originate from reservoirs to the left and to the right of the ballistic graphene sample. E_F is the Fermi energy measured with respect to the Dirac point of the undoped graphene layer. At zero temperature, the transport properties are governed by quasiparticles that approach a square barrier of height U and length L (see Fig. 2) at energy E_F . We assume ballistic transport across the barrier, and also that the spin flip length l_{sf} is much longer than the other length scales of the problem. Given the values for l_{mfp} and l_{sf} reported for graphene,^{1,11,13} this regime should be realistic.

The Hamiltonian (1) has the following plane wave solutions in regions I, II, and III of Fig. 2, respectively:^{7,22}

$$\psi_{(I)} = \left[\begin{pmatrix} 1 \\ \alpha e^{i\theta} \end{pmatrix} e^{ik_x x} + r \begin{pmatrix} 1 \\ -\alpha e^{-i\theta} \end{pmatrix} e^{-ik_x x} \right] e^{ik_y y}, \quad (2)$$

$$\psi_{(II)} = \left[a \begin{pmatrix} 1 \\ \beta e^{i\phi} \end{pmatrix} e^{iq_x x} + b \begin{pmatrix} 1 \\ -\beta e^{-i\phi} \end{pmatrix} e^{-iq_x x} \right] e^{iq_y y}, \quad (3)$$

$$\psi_{(III)} = \begin{pmatrix} 1 \\ \alpha e^{i\theta} \end{pmatrix} e^{ik_x(x-L)} e^{ik_y y}. \quad (4)$$

The momentum of the incident particle makes an angle $\theta = \arctan(k_y/k_x)$ with the x axis. The angle of refraction, i.e., the corresponding angle inside the barrier, is $\phi = \arctan(q_y/q_x)$. We consider only elastic scattering at the interfaces and define

$$k_F \equiv (k_x^2 + k_y^2)^{1/2} = (\hbar v)^{-1} |E_F| \quad (5)$$

$$\text{and } q_F \equiv (q_x^2 + q_y^2)^{1/2} = (\hbar v)^{-1} |E_F - U|. \quad (6)$$

The parameters $\alpha = \text{sign}(E_F)$ and $\beta = \text{sign}(E_F - U)$ determine the wave function in the corresponding regions as either electronlike (positive sign) or holelike (negative sign). Translational invariance in the transverse (y) direction implies conservation of transverse momentum:

$$k_y = q_y \Rightarrow k_F \sin \theta = q_F \sin \phi. \quad (7)$$

It is convenient to introduce the dimensionless variable

$$\xi = \frac{E_F - U}{E_F} \quad (8)$$

as a measure of the gate voltage U . $\xi=1$ corresponds to the case of no barrier. Throughout the rest of the paper, we will

make the substitution $u = \sin \theta$, and we recall that by definition $\alpha k_F = E_F / \hbar v$ and $\beta q_F = (E_F - U) / \hbar v$.

Matching the wave functions at the interfaces, $\psi_{(I)}(x=0) = \psi_{(II)}(x=0)$ and $\psi_{(II)}(x=L) = \psi_{(III)}(x=L)$, and solving for t give the transmission probability $T \equiv |t|^2$ for a given incoming angle θ :^{7,22}

$$T(u) = \frac{(\xi^2 - u^2)(1 - u^2)}{(\xi^2 - u^2)(1 - u^2) + u^2(1 - \xi)^2 \sin^2(q_x L)}, \quad (9)$$

where

$$q_x L = k_F L \sqrt{\xi^2 - \sin^2 \theta}. \quad (10)$$

Both t and T are invariant under the transformation $k_y \rightarrow -k_y$ as a consequence of the continuity condition (7).

In a real device, the sample has a finite width W . The allowed incoming angles θ are, therefore, determined by the channel index n , due to the quantization of the transverse modes. This quantization condition is, for the infinite mass boundary condition, $k_y \rightarrow k_n = (n + \frac{1}{2}) / W$, where n are integers in the range $0 - N_{\max} = \lfloor k_F W / \pi - 1/2 \rfloor$, and the transverse states are superpositions of states with positive and negative k_y .^{22,25} Provided that the transverse momentum is conserved across the barrier interfaces, Eq. (9) is valid for systems of both finite and infinite width.²²

The conductance through the barrier for each spin independent channel is given in the Landauer-Büttiker formalism as

$$G = g_v \frac{e^2}{h} \sum_{n=0}^{N_{\max}} T_n, \quad (11)$$

where $g_v = 2$ is the valley degeneracy and T_n is the transmission probability [Eq. (9)] for a given transverse channel k_n . When the number of channels N becomes large, i.e., $k_F W \gg 1$, we can replace the summation over channels with an integration over transverse momenta, such that the conductance becomes

$$G = \mathcal{G}_0 \int_0^1 du T(u) = \mathcal{G}_0 g, \quad (12)$$

with \mathcal{G}_0 defined as

$$\mathcal{G}_0 = \frac{2e^2 k_F W}{h \pi}. \quad (13)$$

The dimensionless conductance g in Eq. (12) is plotted in Fig. 3 as a function of the dimensionless gate voltage ξ .

From Eq. (10), we see that the longitudinal momenta in the barrier region, q_x , can be either purely real ($\xi^2 > u^2$) or purely imaginary ($\xi^2 < u^2$), corresponding to propagating and evanescent modes, respectively.²² The contribution to the conductance from the evanescent modes becomes dominant around $\xi = 0$, and the scaling of the conductance with length at this point resembles that of a diffusive system.^{22,26} For $|\xi| < 1$, the conductance (12) can be split into the contributions from propagating and evanescent modes:

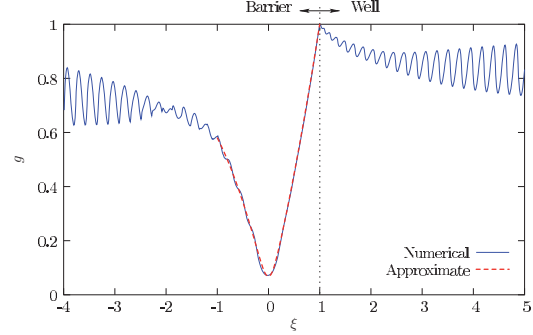


FIG. 3. (Color online) Conductance $g = G / \mathcal{G}_0$ as a function of $\xi = (E_F - U) / E_F$ normalized to one spin channel when $k_F L = 14$. The solid (blue) line shows the numerical result using Eq. (12), while the dashed (red) line is computed using the approximation (17). $\mathcal{G}_0 = 2e^2 k_F W / h \pi$.

$$g = \int_0^{|\xi|} du T(u) + \int_{|\xi|}^1 du T(u) = g_{\text{prop}} + g_{\text{evan}}, \quad (14)$$

from which it is readily seen that the evanescent modes dominate in the region near $\xi = 0$ as long as $T(u) > 0$ for at least some $u > |\xi|$ (see Appendix B for details). For $k_F L \gg 1$ and setting $\xi = 0$ in Eq. (9):

$$T(u) \approx \frac{1}{\cosh^2(k_F L u)}. \quad (15)$$

This corresponds to the limit $N_{\max} \gg W/L$ in Ref. 22. Upon insertion of Eq. (15) into the integral (12), we find that the conductance at the Dirac point is inversely proportional to the system length:

$$g \approx \frac{1}{k_F L}. \quad (16)$$

This corresponds to the so-called minimal conductivity $g_s G \times L/W = g_s g_v e^2 / h \pi$,²² $g_s = 2$ being the spin degeneracy.

For $|\xi| < 1$ and $k_F L \gg 1$, we can approximate the conductance by the expression

$$g \approx (a_1 + a_2 \xi) |\xi| + \frac{1}{k_F L} \exp(-k_F L |\xi|), \quad (17)$$

with $a_1 = 0.79$ and $a_2 = 0.21$ (see Appendix C for details and Fig. 3 for a comparison with the exact solution). Equation (17) reduces to Eq. (16) when $\xi \rightarrow 0$.

For $|\xi| > 1$, corresponding to a well or a large barrier, only propagating modes contribute, and we would expect to see resonances in the conductance due to quasibound²⁷ states in the barrier region. In the limit $|\xi| \gg 1$, using that $u^2 \leq 1$, the tunneling probability (9) becomes

$$T(u) \approx \frac{1 - u^2}{1 - u^2 \cos^2(k_F L \xi)}, \quad (18)$$

resulting in the expression

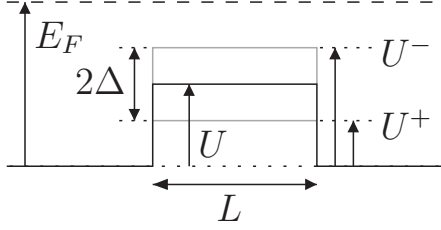


FIG. 4. Ferromagnetic proximity effect splits the barrier according to spin such that $U^\pm = U \mp \Delta$.

$$g \approx \frac{|\cos(k_F L \xi)| - \sin^2(k_F L \xi) \operatorname{arctanh}[\cos(k_F L \xi)]}{|\cos(k_F L \xi)|^3} \quad (19)$$

for the dimensionless conductance (see Appendix B for details). The period of g as a function of ξ is $\pi/k_F L$. Also g oscillates between $2/3$ and 1 . The transmission probability analogous to Eq. (9) for a square barrier in a nonchiral two-dimensional system,⁷

$$T_{\text{nonchiral}} = \frac{4(\xi^2 - u^2)(1 - u^2)}{4(\xi^2 - u^2)(1 - u^2) + (1 - \xi^2)^2 \sin^2(q_x L)}, \quad (20)$$

also gives oscillation with the same periodicity, but, in this case, the conductance oscillates between 0 and 1 . The fact that the conductance given by Eq. (19) oscillates between $2/3$ and 1 is due to the perfect tunneling of carriers near normal incidence in graphene. Another difference between graphene and a nonchiral system is that the transmission probability of the latter [Eq. (20)] is symmetric around $\xi=0$, while the transmission probability for graphene [Eq. (9)] depends also on the sign of ξ through the $(1-\xi)$ factor in the denominator. The asymmetry for the case of graphene can readily be seen in Fig. 3.

IV. SPIN DEPENDENT BARRIER

We now turn to a situation where the two spin channels see barriers of different heights, i.e., the bottom of the conduction band at the barrier is shifted differently according to spin. Such a shift can arise through a Zeeman interaction due to an in-plane magnetic field or exchange field.

The exchange term Δ splits the system into two separate subsystems according to spin. For an external magnetic field B , the splitting is given by $\Delta \approx 2\mu_B B$. We introduce the spin dependent variables

$$\xi^\pm = \xi \pm \delta = \frac{E_F - U}{E_F} \pm \frac{\Delta}{E_F}, \quad (21)$$

where \pm denotes spins parallel (+) or anti parallel (−) to the exchange field (see Fig. 4). In the following, we will let $g^{+(-)}$ denote the spin resolved conductance for spins parallel (antiparallel) to the exchange field. Assuming no spin flip, $l_{sf} \gg L$, the total conductance g_T across the barrier is given by the sum:

$$g_T = g^+ + g^- = g(\xi^+) + g(\xi^-). \quad (22)$$

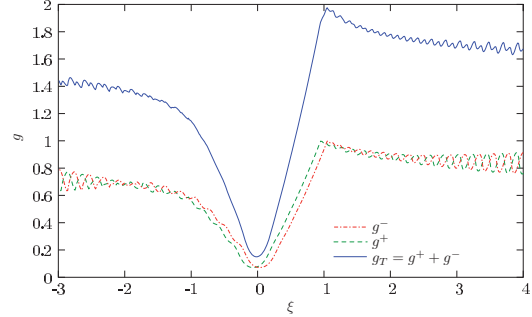


FIG. 5. (Color online) Spin resolved conductance through a square barrier for $k_F L = 14$ and $\delta = \Delta/E_F = 0.05$. The normalization of conductance is chosen as in Fig. 3 to correspond to $g(1) = 1$ for each spin channel.

Because $\Delta/B \approx 5.8 \times 10^{-2}$ meV/T, a direct interaction of the spins with an external magnetic field gives only a very weak effect (about 1 meV per 20 T), and one will have to rely on more indirect effects to observe such spin splittings.

We propose depositing a ferromagnetic insulator, e.g., EuO, on top of the graphene sample to induce an exchange splitting in graphene. A normal gate on top of the insulator allows us to control the Fermi level in the same region. The resulting potential profile is sketched in Fig. 4. A rough estimate suggests that the splitting energy can be of order $\Delta \approx 5$ meV at EuO/graphene interfaces (see Appendix A).

As can be seen from Fig. 5, the effect of the splitting is simply to shift the conductance of each spin channel with respect to the other, leading to a broadening of the dip in the total conductance g_T near the Dirac point $\xi=0$. To be able to observe the splitting directly in the g_T near the Dirac point, the magnitude of the splitting must be larger than the width of the dip of each spin resolved conductance, $g^{+(-)}$. A measure $w = (k_F L)^{-1}$ of the width of the dip is discussed in Appendix C, leading to the condition

$$L > \frac{\hbar v}{|\Delta|} \quad (23)$$

for observation of the splitting directly in g_T at the Dirac point. However, the broadening of the dip due to a spin splitting would be difficult to distinguish from a broadening due to other effects.

From Fig. 5, it is apparent that the spin splitting has a more dramatic effect on the total conductance g_T at large barrier doping, since, due to the transmission resonances, g^+ and g^- can differ substantially at a given ξ . The asymptotic expression (19) for $|\xi| \gg 1$ implies that g_T has periodicity $\pi/k_F L$ in ξ for $\delta=0$, as shown at the bottom of Fig. 6. With increasing δ , each peak of g_T gradually splits into two spin resolved peaks. The splitting measured from the conductance 2δ equals $2\Delta/E_F$ (see Fig. 6), so, in principle, Δ can be determined directly from the total conductance across the barrier in this way.

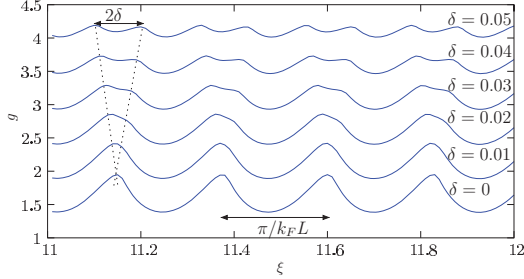


FIG. 6. (Color online) Total conductance $g_T = g^+ + g^-$ when $|\xi| \gg 1$ for a range of different splittings $\delta = \Delta/E_F$. For clarity the curves are shifted upward in steps of 0.5 with increasing δ .

On the other hand, it is also possible to study the splitting by examining the spin polarization across the barrier.

We define a normalized spin polarization p along the direction of the exchange field as

$$p = \frac{g^+ - g^-}{g^+ + g^-}. \quad (24)$$

Inserting the approximate expression for the conductance from Eq. (17) and comparing to exact numerical calculations, we find good agreement in the whole region $|\xi| < 1$ (see Fig. 7).

Equation (17) implies that the polarization becomes more pronounced with increasing barrier length L (see Fig. 8), owing to the fact that the evanescent modes are increasingly suppressed as L increases.

V. MAGNETORESISTANCE

Placing two magnetic gates a distance D apart in the graphene sample is a possible way to probe the polarization p in Eq. (24). We assume either that D is much larger than the mean free path l_{mfp} (but still much shorter than l_{sf}), or that the experimental setup is realized as a three-terminal experiment, where the middle terminal completely randomizes the momenta between the two barriers (see Fig. 9).

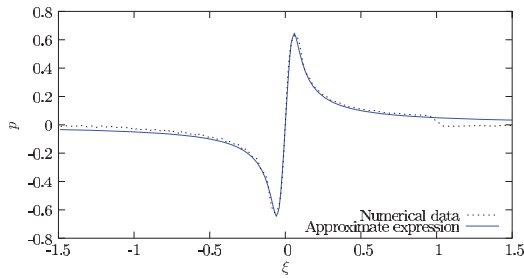


FIG. 7. (Color online) The polarization p from the approximation (17) compared to the exact numerical result obtained directly from Eq. (12). Both plots are for $k_F L = 14$ and $\delta = 0.05$.

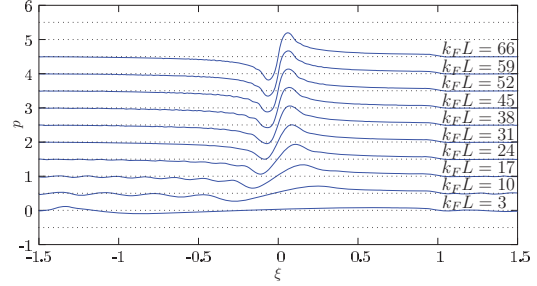


FIG. 8. (Color online) Polarization p as a function of $\xi = (E_F - U)/E_F$ for different barrier lengths L with $\delta = 0.05$.

Assuming that no spin flip processes take place in the sample, the conductance for each spin channel is found by treating the two barriers as resistors connected in series. Arranging the magnetizations of the ferromagnetic barriers parallel or antiparallel to each other gives different conductances $g_{\uparrow\uparrow}$ and $g_{\uparrow\downarrow}$, corresponding to the two situations in Fig. 9, respectively. We study the polarization using the “pessimistic” definition of the magnetoresistance: $\text{MR} = (g_{\uparrow\uparrow} - g_{\uparrow\downarrow})/g_{\uparrow\uparrow}$. For the general case of different left (L) and right (R) barriers, we obtain

$$\text{MR} = \frac{4p_L g_L p_R g_R}{(g_L + g_R)^2 - (p_L g_L - p_R g_R)^2}, \quad (25)$$

assuming that the resistance of the region D between the barriers is negligible compared to the typical resistances of the barriers. For clarity, we have suppressed the subscript T denoting total conductance of the left (right) barrier: $g_{L(R)} \equiv g_{L(R)}^+ + g_{L(R)}^-$.

For identical barriers, MR reduces to the simple expression

$$\text{MR} = p^2. \quad (26)$$

The combination of Eqs. (17), (24), and (25) allows us to experimentally determine Δ from magnetoresistance measurements. The change of sign in the polarization, shown in

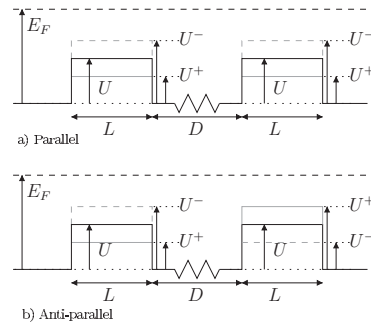


FIG. 9. Measuring tunneling magnetoresistance by placing two short barriers a distance $D \gg l_{\text{mfp}}$ apart.

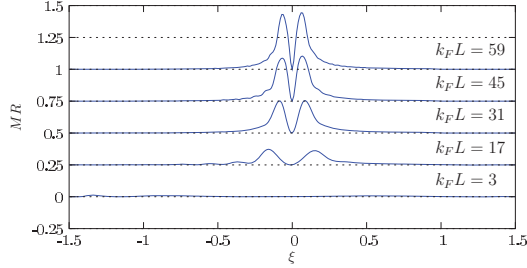


FIG. 10. (Color online) Magnetoconductance for two barriers of equal height. The curves are shifted upward in steps of 0.25 for clarity.

Fig. 8, is directly related to the relative shift of the conductances corresponding to each spin channel. The coefficient MR is proportional to p^2 , which produces the double peak structure seen in Figs. 10 and 11. The condition for observing MR effects is also given by Eq. (23), $L > \hbar v / |\Delta|$. However, since the MR signal is only sensitive to the spin degree of freedom, we expect MR experiments to be a more direct probe of a spin induced splitting. Any broadening of the dip introduced by sources other than Δ will also be less important, since the polarization p changes sign around $\xi=0$.

For a splitting of $\Delta=5$ meV, the condition in Eq. (23) gives $L > 110$ nm (or, equivalently, $k_F L > 20$). As can be seen in Fig. 8, the features in the polarization becomes sharper when increasing the length above this value. This also translates into a clearer signal in the magnetoconductance, which is plotted in Figs. 10 and 11 for barriers of equal and unequal heights, respectively.

Finally, even if the top gate creates a smooth tunable barrier, far from the perfectly square potential discussed here, magnetoconductance measurements should still provide an experimental demonstration of proximity-induced ferromagnetism in graphene, as the magnetic insulator still creates a sharp splitting of the spin up and spin down states in the region underneath the magnetic insulator. The exact dependence of the polarization p on the splitting Δ may be different in this case than the one presented here.

VI. CONCLUSIONS

We suggest using magnetic insulators deposited on top of graphene to create ferromagnetic graphene. The exchange

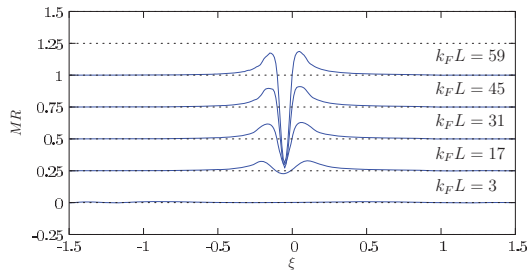


FIG. 11. (Color online) Same as in Fig. 10, with one barrier being lower than the other ($|\xi_L - \xi_R| = 0.1$).

interaction between electrons in graphene and the localized magnetic moments in the insulator will give rise to a proximity-induced exchange splitting Δ . We have estimated that the graphene exchange splitting due to the magnetic insulator EuO in close proximity can be around $\Delta=5$ meV.

We have studied how the conductance of a square barrier in graphene is modified by the presence of a ferromagnetic insulator. We show that for large barriers or deep wells, $|\xi| \gg 1$, the splitting Δ can be determined directly from the total conductance across the barrier, provided that the barrier is sharp enough for transmission resonances to appear. For a barrier of length $L > \hbar v / |\Delta|$, where v is the Fermi velocity of the charge carriers in graphene, Δ should be observable in the polarization of the tunneling current near the Dirac point of the barrier, irrespective of whether the barrier is smooth or sharp.

Demonstration of proximity-induced ferromagnetism in graphene should be possible through magnetoconductance measurements both for smooth and sharp barriers.

Note added. Recently, we became aware of a related work by Semenov *et al.*,²⁸ where a similar system with a magnetic gate is considered. Their work discusses the possibility of a spin field effect transistor, the feasibility of which relies on variations of the spin splitting across the sample of the same order of magnitude as our estimate for the splitting itself.

ACKNOWLEDGMENTS

We thank G. E. W. Bauer, M. F. Craciun, F. Guinea, Yu. V. Nazarov, E. Prada, and S. Russo for discussions. This work was supported by EC Contract No. IST-033749 ‘‘DynaMax’’ and The Research Council of Norway through Grant No. 167498/V30 and No. 162742/V30.

APPENDIX A: ESTIMATION OF EXCHANGE SPLITTING AT EuO/ GRAPHENE INTERFACES

Experiments on depairing at EuO/Al interfaces suggest that the superconducting quasiparticles of Al experience an exchange field due to the Eu^{2+} moments.^{14,19} This interaction is short ranged; essentially, only the nearest layer of Eu^{2+} ions contributes. It has been shown that the exchange interaction between Eu^{2+} ions and charge carriers can be described as a Zeeman splitting^{14–17,19}

$$\Delta \approx cJ\langle S_z \rangle, \quad (\text{A1})$$

where c is the fractional density of Eu^{2+} ions to that of itinerant electrons in Al at the interface, J is the spatial average of the exchange integral, and $\langle S_z \rangle$ is the average spin of Eu^{2+} ions at a given temperature.

Perpendicular to the surface of thin Al films, the electronic wave functions can be well approximated by atomic-like wave functions.¹⁸ The spatial range of an atomic wave function is determined by the ratio Z/n ,²⁹ where Z is the atomic number and n is the energy level. Since this ratio is approximately the same for the $3s$ and $3p$ orbitals in Al ($Z/n=13/3 \approx 4.3$) and the $2p$ orbitals in graphene ($Z/n=6/2=3$), we expect the overlap between the wave functions of localized moments and itinerant electrons at EuO/

graphene interfaces to be comparable to those for EuO/Al. Accordingly, we assume that the exchange interaction between Eu^{2+} ions and itinerant electrons are the same at EuO/Al and EuO/graphene interfaces. Reference 17 reports the value $J=15$ meV for Eu/Al interfaces, which also agrees with the exchange energy $h_{\text{ex}}=0.1$ meV estimated in Ref. 19.

Using a nearest neighbor distance in graphene of 1.42 \AA ,³⁰ we obtain for the areal density of itinerant electrons $n_C \approx 40 \text{ nm}^{-2}$. Similarly, the areal density of Eu^{2+} ions at the surface of EuO is $n_{\text{Eu}^{2+}} \approx 4 \text{ nm}^{-2}$. Together this gives $c=n_{\text{Eu}^{2+}}/n_C \approx 10^{-1}$.

The temperature dependence of the average spin of Eu^{2+} ions in EuO is calculated in Ref. 31, showing that $3.5 \geq \langle S_z \rangle \geq 3$ for $0 < T < 30$ K.

Collecting all together, we arrive at the estimate

$$\Delta \approx 5 \text{ meV} \quad (\text{A2})$$

for the exchange splitting in graphene due to EuO. We stress that this is a very rough estimate which needs to be tested experimentally.

APPENDIX B: LIMITING CASES FOR THE CONDUCTANCE

1. Large potential

For large barriers or deep wells, $|E_F - U| \gg |E_F|$, $\xi^{-1} \ll 1$. The transmission probability (9) then becomes

$$T(u) \approx \frac{1 - u^2}{1 - u^2 \cos^2(k_F L \xi)}. \quad (\text{B1})$$

The conductance in this case is

$$g \approx \int_0^1 du \frac{1 - u^2}{1 - u^2 \cos^2(k_F L \xi)} = \frac{|\cos(k_F L \xi)| - \sin^2(k_F L \xi) \text{arctanh}[\cos(k_F L \xi)]}{|\cos(k_F L \xi)|^3}, \quad (\text{B2})$$

which oscillates between the values $2/3$ and 1 with period $\pi/k_F L$ as a function of ξ .

2. Evanescent modes

When $|E_F - U| \ll |E_F|$, the evanescent modes dominate the transport so we neglect the contribution from the propagating modes. Using that $|\xi| \leq u$ for evanescent modes, and that $|\xi| \ll 1$, we find

$$T(u) \approx \frac{1}{\cosh^2(k_F L u)}, \quad (\text{B3})$$

which is valid for $k_F L \gg 1$. The conductance then becomes

$$g \approx \int_0^1 \frac{1}{\cosh^2(k_F L u)} \approx \frac{1}{k_F L}. \quad (\text{B4})$$

APPENDIX C: DIP OF THE TUNNELING CONDUCTANCE AROUND THE DIRAC POINT

We study how the width of the dip in the conductance around the Dirac point scales with barrier length L . The contributions from both evanescent and propagating modes must be considered when $|\xi| < 1$.

The conductance due to propagating modes can be written as

$$g_{\text{prop}} = f(\xi) |\xi|, \quad (\text{C1})$$

where

$$f(\xi) = \int_0^1 dv \frac{1}{1 + \frac{v^2(1 - \xi)^2}{(1 - v^2)(1 - \xi^2 v^2)} \sin^2(k_F L \xi \sqrt{1 - v^2})}. \quad (\text{C2})$$

When $k_F L \gg 1$, $f(\xi)$ is well approximated by a linear curve $a_1 + a_2 \xi$ for all $|\xi| < 1$. The function $f(\xi)$ deviates from linearity in an oscillatory fashion in a small region around $|\xi|=0$, but $f(\xi)$ is always of order unity. For $k_F L \gg 1$, the conductance due to propagating waves in the region $|\xi| < 1$ can, therefore, be approximated by

$$g_{\text{prop}} \approx (a_1 + a_2 \xi) |\xi|, \quad (\text{C3})$$

where the value of the constants $a_1=0.79$ and $a_2=0.21$ depend weakly on $k_F L$ when $k_F L \gg 1$, and are found by fitting Eq. (C3) to numerical calculations.

We have not been able to obtain an analytical expression for the contribution due to evanescent modes. However, we note that the contribution from $T(u)$ in Eq. (9) to evanescent modes can be well approximated by a decaying exponential function. We have fitted our numerical calculations of $g_{\text{evan}} = \int_{|\xi|}^1 du T(u)$ to an exponentially decaying function of $|\xi|$:

$$g_{\text{evan}} \sim A e^{-B|\xi|}. \quad (\text{C4})$$

The constant A is found to be $1/k_F L$ by letting $\xi \rightarrow 0$ and comparing with Eq. (16). Numerical evidence suggest that $B = C k_F L$, with C of order unity.

We define the width w of the dip in the conductance at the Dirac point as $w = 2|\xi_c|$, where $|\xi_c|$ is the value of $|\xi|$ for which $g_{\text{prop}}(\xi_c) = g_{\text{evan}}(\xi_c)$. Taking advantage of the fact that g_{evan} decays rapidly away from $|\xi|=0$, we ignore the second order term in the expression for g_{prop} for the purpose of estimating the width w . We find that

$$w = 2|\xi_c| \approx \frac{1}{k_F L}, \quad (\text{C5})$$

using $2\mathcal{W}(1/a_1) \approx 1$, where \mathcal{W} is the Lambert W function.

*havard.haugen@ntnu.no

- ¹K. S. Novoselov, A. K. Geim, S. V. Morozov, D. Jiang, Y. Zhang, S. V. Dubonos, I. V. Grigorieva, and A. A. Firsov, *Science* **306**, 666 (2004).
- ²K. S. Novoselov, A. K. Geim, S. V. Morozov, D. Jiang, M. I. Katsnelson, I. V. Grigorieva, S. V. Dubonos, and A. A. Firsov, *Nature (London)* **438**, 197 (2005).
- ³Y. Zheng, Y.-W. Tan, H. L. Stormer, and P. Kim, *Nature (London)* **438**, 201 (2005).
- ⁴J. González, F. Guinea, and M. A. H. Vozmediano, *Nucl. Phys. B* **406**, 771 (1993).
- ⁵K. Nomura and A. H. MacDonald, *Phys. Rev. Lett.* **98**, 076602 (2007).
- ⁶A. F. Morpurgo and F. Guinea, *Phys. Rev. Lett.* **97**, 196804 (2006).
- ⁷M. I. Katsnelson, K. S. Novoselov, and A. K. Geim, *Nat. Phys.* **2**, 620 (2006).
- ⁸G. Schmidt, D. Ferrand, L. W. Molenkamp, A. T. Filip, and B. J. van Wees, *Phys. Rev. B* **62**, R4790 (2000).
- ⁹X. Lou, C. Adelman, S. A. Crooker, E. S. Garlid, J. Zhang, S. M. Reddy, S. D. Flexner, C. J. Palmstrom, and P. A. Crowell, *Nat. Phys.* **3**, 197 (2007).
- ¹⁰B. W. Alphenaar, K. Tsukagoshi, and M. Wagner, *J. Appl. Phys.* **89**, 6863 (2001).
- ¹¹D. Huertas-Hernando, F. Guinea, and A. Brataas, *Eur. Phys. J. Spec. Top.* **148**, 177 (2007).
- ¹²D. Huertas-Hernando, F. Guinea, and A. Brataas, *Phys. Rev. B* **74**, 155426 (2006).
- ¹³N. Tombros, C. Jozsa, M. Popinciuc, H. T. Jonkman, and B. van Wees, *Nature (London)* **448**, 571 (2007).
- ¹⁴P. M. Tedrow, J. E. Tkaczyk, and A. Kumar, *Phys. Rev. Lett.* **56**, 1746 (1986).
- ¹⁵J. E. Tkaczyk and P. M. Tedrow, *Phys. Rev. Lett.* **61**, 1253 (1988).
- ¹⁶X. Hao, J. S. Moodera, and R. Meservey, *Phys. Rev. Lett.* **67**, 1342 (1991).
- ¹⁷G. M. Roesler, M. E. Filipkowski, P. R. Broussard, Y. U. Idzerda, M. S. Osofsky, and R. J. Soulen, *Proc. SPIE* **2157**, 285 (1994).
- ¹⁸G. S. Painter, *Phys. Rev. B* **17**, 662 (1978).
- ¹⁹T. Tokuyasu, J. A. Sauls, and D. Rainer, *Phys. Rev. B* **38**, 8823 (1988).
- ²⁰V. V. Cheianov, V. Fal'ko, and B. L. Altshuler, *Science* **315**, 1252 (2007).
- ²¹J. M. Pereira, Jr., P. Vasilopoulos, and F. M. Peeters, *Appl. Phys. Lett.* **90**, 132122 (2007).
- ²²J. Tworzydło, B. Trauzettel, M. Titov, A. Rycerz, and C. W. J. Beenakker, *Phys. Rev. Lett.* **96**, 246802 (2006).
- ²³B. Özyilmaz, P. Jarillo-Herrero, D. Efetov, D. A. Abanin, L. S. Levitov, and P. Kim, *Phys. Rev. Lett.* **99**, 166804 (2007).
- ²⁴B. Huard, J. A. Sulpizio, N. Stander, K. Todd, B. Yang, and D. Goldhaber-Gordon, *Phys. Rev. Lett.* **98**, 236803 (2007).
- ²⁵M. V. Berry and R. J. Mondragon, *Proc. R. Soc. London, Ser. A* **412**, 53 (1987).
- ²⁶E. Prada, P. San-Jose, B. Wunsch, and F. Guinea, *Phys. Rev. B* **75**, 113407 (2007).
- ²⁷P. G. Silvestrov and K. B. Efetov, *Phys. Rev. Lett.* **98**, 016802 (2007).
- ²⁸Y. G. Semenov, K. W. Kim, and J. M. Zavada, *Appl. Phys. Lett.* **91**, 153105 (2007).
- ²⁹J. J. Brehm and W. J. Mullin, *Introduction to the Structure of Matter* (Wiley, New York, 1989).
- ³⁰P. R. Wallace, *Phys. Rev.* **71**, 622 (1947).
- ³¹W. Nolting, W. Borgiel, and G. Borstel, *Phys. Rev. B* **35**, 7025 (1987).

Paper [2]

Spin transport in doped graphene

Unpublished manuscript (2010)

Spin transport in doped graphene

Håvard Haugen and Arne Brataas

Department of Physics, Norwegian University of Science and Technology, N-7491 Trondheim, Norway

(Dated: October 12, 2010)

We study spin transport in graphene and find an effective kinetic equation for highly doped graphene with intrinsic and Rashba-like spin-orbit interaction. The kinetic equation incorporates precession about a spin-orbit induced field, analogous to the situation in two-dimensional electron gases with Rashba spin-orbit interaction, as well as the spin precession induced by a transverse magnetic field. At high doping, the effects of the intrinsic spin-orbit coupling are small compared to that induced by the extrinsic Rashba coupling of graphene. In a perpendicular magnetic field, the intrinsic spin-orbit coupling, which contributes to the spin precession around an out-of-plane axis, is masked by the Zeeman effect.

PACS numbers: 71.70.Ej, 73.23.-b

I. INTRODUCTION

The low dimensionality and gate-controllable doping makes graphene a promising material for electronics applications.¹ Graphene exhibits high mobilities over a wide range of carrier densities and temperatures, leading to ballistic transport on sub-micron scales.² Due to the low atomic number of carbon, the spin-orbit (SO) interaction in graphene is rather weak, making graphene also a promising candidate for spintronics applications,^{3,4} where the aim is to exploit the spin of the electrons in addition to the charge.⁵

Crucial to the application of graphene for spintronics is a clear understanding of spin dynamics and relaxation. The relevant spin relaxation mechanisms in graphene are the Elliot-Yafet (EY) and D'yakonov-Perel (DP) mechanisms.⁶ In the EY mechanism there is a finite probability of spin flip in an impurity scattering event, since in the presence of SO coupling the electronic eigenstates are mixtures of spin up and spin down states.⁵ The DP mechanism is present in crystals lacking inversion symmetry. In these systems the SO coupling introduces a momentum dependent effective magnetic field about which the spins precess. When momentum changes in a scattering event, the effective magnetic field also changes, leading eventually to a loss of spin coherence.⁵ Theoretical works on spin relaxation in graphene have concluded that the main source of intrinsic spin relaxation is through the DP mechanism,⁷ although scattering at extrinsic defects could lead to EY scattering.

Experiments with relatively dirty graphene samples find spin relaxation times τ_s in the range 100 – 200 ps.^{3,4,8} These times are much shorter than theoretically estimated values.^{6,9,10} In several experiments, the spin relaxation time is found to be proportional to the momentum scattering time τ , indicating that the EY mechanism is dominating spin relaxation.^{4,11} However, a recent experimental work, addressing the role of charged impurities for spin transport, reports that the spin and momentum relaxation rates are not proportional, indicating that charged impurity scattering is not necessarily the dominant factor in spin relaxation.¹² The relaxation

time in this work was still found to be comparable to those in earlier experiments.

A recent first-principles calculation¹⁰ suggests that the intrinsic SO coupling is stronger by an order of magnitude than was previously assumed,^{6,13} making the intrinsic and the Rashba-like SO coupling in graphene comparable in magnitude for typical experimental conditions.¹⁰

The aim of this work is to investigate spin transport in doped graphene in the presence of both intrinsic and Rashba-like SO coupling. We focus on the ballistic limit, discussing the influence of a finite intrinsic SO coupling on the spin dynamics in the presence of a perpendicular magnetic field.

II. HAMILTONIAN

The low energy Hamiltonian of graphene with SO interaction is

$$\mathcal{H} = \mathcal{H}_0 + \mathcal{H}_R + \mathcal{H}_I + \mathcal{H}_Z + V, \quad (1)$$

where V is the impurity potential and^{14–16}

$$\mathcal{H}_0 = v\boldsymbol{\sigma} \cdot \hat{\mathbf{p}} \quad (2)$$

$$\mathcal{H}_R = \frac{\Delta_R}{2} (\boldsymbol{\sigma} \times \mathbf{s})_z = -\frac{\Delta_R}{2} \boldsymbol{\sigma} \cdot \boldsymbol{\eta} \quad (3)$$

$$\mathcal{H}_I = \Delta_I \sigma_z s_z \quad (4)$$

$$\mathcal{H}_Z = -\frac{g\mu_B}{2} s_z B, \quad (5)$$

with $\boldsymbol{\eta} = \hat{\mathbf{z}} \times \mathbf{s}$. The form of the Hamiltonian (1) can be derived from symmetry considerations alone¹⁴ or explicitly from a tight binding model of graphene taking into account hybridization and atomic SO coupling.¹⁵ The Pauli matrices $\boldsymbol{\sigma}$ and \mathbf{s} operate on sublattice and spin space, respectively, and $\hat{\mathbf{p}} = -i\hbar\nabla + e\mathbf{A}$ is the momentum operator. We consider a magnetic field pointing out of the plane, and choose the symmetric gauge, $\mathbf{A}(\mathbf{r}) = \frac{1}{2}(\mathbf{B} \times \mathbf{r})$, which simplifies the derivation of the kinetic equation.^{17,18} The Hamiltonian (1) acts on spinors of the type $\Psi = (\Psi_K, \Psi_{K'})^T$,

with $\Psi_K = (\psi_{KA\uparrow}, \psi_{KA\downarrow}, \psi_{KB\uparrow}, \psi_{KB\downarrow})^T$ and $\Psi_{K'} = (\psi_{K'B\uparrow}, \psi_{K'B\downarrow}, -\psi_{K'A\uparrow}, -\psi_{K'A\downarrow})^T$.¹⁹ In the absence of intervalley scattering the K and K' valleys are degenerate. Note that the roles of the B and A sublattices are reversed at K' compared to K . In this paper we consider long range impurity scattering, which typically arises due to charged impurities trapped near the graphene layer.^{20,21} Since the momentum transfer associated with long range scatterers is small, the two valleys K and K' are not coupled by impurity scattering, and V can be treated as a scalar potential for each valley.

The intrinsic SO interaction Δ_I is dominated by the coupling between d and p_z orbitals of neighboring carbon atoms in the graphene lattice.¹⁰ The intrinsic SO interaction was previously assumed to be small compared to the extrinsic interaction Δ_R ,^{15,16} and calculations of spin relaxation have therefore focused mainly on the effect of the latter.⁶ The extrinsic Rashba SO interaction Δ_R arises from $\sigma - \pi$ band mixing induced by local curvature of the graphene sheet or a transverse electric field.^{10,15} The values inferred from the first-principles calculation¹⁰ indicates that Δ_I and Δ_R can be of comparable magnitude for realistic experimental conditions.

A recent calculation suggests that the spin relaxation time can be determined from a generalized EY mech-

anism due to the intrinsic spin-orbit coupling.²² However, the value of Δ_I found by fitting to experiments is two orders of magnitude larger than what the theory reports.¹⁰ Furthermore, short-range impurities seem to have been implicitly assumed by Ref. 22, although never explicitly stated. It has been suggested that hybridization due to adsorbed impurities can lead to a large increase in the SO coupling,²³ consistent with observations of large anisotropic spin splitting observed for graphene on a substrate.^{24,25}

To study the spin transport in doped graphene, we generalize the procedure of Ref. 13 by including the intrinsic SO interaction. We consider the stationary situation, and expand the Schrödinger equation explicitly in sublattice space at the Fermi energy ϵ_F ,

$$\begin{pmatrix} \epsilon_F - V(\mathbf{r}) - \Lambda_- s_z & -v\bar{p}_- - i\Delta_R s_- \\ -v\bar{p}_+ + i\Delta_R s_+ & \epsilon_F - V(\mathbf{r}) + \Lambda_+ s_z \end{pmatrix} \begin{pmatrix} \psi_{KA} \\ \psi_{KB} \end{pmatrix} = 0. \quad (6)$$

Here $\Lambda_{\pm} = \Delta_I \pm \Delta_Z$ and the Zeeman energy is defined as $\Delta_Z = \frac{g}{2}\mu_B B$. We have used the definitions $\bar{p}_{\pm} = \bar{p}_x \pm i\bar{p}_y$ and $s_{\pm} = (s_x \pm is_y)/2$. The energy ϵ_F is measured from the charge neutrality (Dirac) point of graphene. Rearranging the two equations in Eq. (6), we get effective Hamiltonians for ψ_{KA} and ψ_{KB} which depend parametrically on ϵ_F :

$$H_{K(A/B)}^{\text{eff}} = \frac{v^2}{\epsilon_F - V(\mathbf{r}) \pm \Lambda_{\pm} s_z} [\bar{\mathbf{p}}^2 \pm e\hbar B] - \frac{v\Delta_R}{\epsilon_F - V(\mathbf{r}) \pm \Lambda_{\pm}} \boldsymbol{\eta} \cdot \bar{\mathbf{p}} + \frac{\Delta_R^2}{\epsilon_F - V(\mathbf{r}) \pm \Lambda_{\pm}} \frac{(1 \mp s_z)}{2} \pm \Lambda_{\mp} s_z + V(\mathbf{r}) - \frac{i\hbar v [\partial_{\pm} V(\mathbf{r})]}{[\epsilon_F - V(\mathbf{r}) \pm \Lambda_{\pm} s_z]^2} (v\bar{p}_{\pm} \mp i\Delta_R s_{\pm}), \quad (7)$$

where the upper and lower sign corresponds to the A and B sublattice, respectively. These expressions for the effective Hamiltonians are exact and valid when none of the denominators in (7) vanish. The quadratic momentum dependence and the presence of a Rashba SO term proportional to $\boldsymbol{\eta} \cdot \bar{\mathbf{p}}$ is analogous to a normal 2DEG with SO coupling.²⁶

III. KINETIC EQUATION

We express the kinetic equation in terms of the Wigner function $\check{g}_{p\epsilon}(\mathbf{R}, T)$, which is related to the two point Green's functions through a Fourier transform over the fast variables,¹⁸

$$\check{G}(\mathbf{r}_1 t_1, \mathbf{r}_2 t_2) = \int \frac{d\mathbf{p}}{(2\pi)^3} \frac{d\epsilon}{2\pi} e^{\frac{i}{\hbar}[(\mathbf{p} - e\mathbf{A}(\mathbf{R})) \cdot \mathbf{r} - \epsilon t]} \check{g}_{p\epsilon}(\mathbf{R}, T). \quad (8)$$

The Wigner coordinates are defined in a standard way as

$$x_{1(2)} = \frac{1}{2}X + (-)x \quad (9)$$

where x is either a position or time coordinate. We consider a stationary system,

$$\check{G}(\mathbf{r}_1 t_1, \mathbf{r}_2 t_2) = \check{G}(\mathbf{r}_1, \mathbf{r}_2; t_1 - t_2) \quad (10)$$

so

$$\check{g}_{p\epsilon}(\mathbf{R}, T) = \check{g}_{p\epsilon}(\mathbf{R}). \quad (11)$$

The kinetic equation is derived from the Keldysh formalism,^{18,26}

$$[G^R]^{-1} G^K - G^K [G^A]^{-1} = \Sigma^K G^A - G^R \Sigma^K, \quad (12)$$

where convolution products are implied between the factors. The superscripts R , A , and K denote, respectively, the retarded, advanced, and Keldysh component of the Green's function. Collecting the self energy terms on the right hand side, we get an equation of the form

$$\begin{aligned} & [G_0^{-1}] G^K - G^K [G_0^{-1}]^\dagger \\ & = \Sigma^R G^K - G^K \Sigma^A + \Sigma^K G^A - G^R \Sigma^K, \end{aligned} \quad (13)$$

where the bare Green's function G_0 , obeys

$$[\epsilon_F - H_{AK}^{\text{eff}}(\mathbf{r}_1)] G_0(\mathbf{r}_1, \mathbf{r}_2) = \delta(\mathbf{r}_1 - \mathbf{r}_2) \quad (14)$$

in the position representation.

The impurity potential $V(\mathbf{r})$ enters non-linearly in the effective Hamiltonian (7) and will, especially at low doping where $\epsilon_F \sim V(\mathbf{r})$, lead to non-perturbative behavior. However, at high doping such that $\epsilon_F \gg V(\mathbf{r})$, we can expand terms of the type $[\epsilon_F - V(\mathbf{r}) \pm \Lambda_{\pm} s_z]^{-1}$ in powers of $u(\mathbf{r}) = V(\mathbf{r})/\epsilon_F$. To lowest order, the effective Hamiltonian is linear in $V(\mathbf{r})$. In this linearized regime, the effect of impurity scattering can be taken into account by a standard self energy method based on the Dyson equation.¹⁸ The dominant terms in the self energies on the right hand side of in Eq. (13) are proportional to the impurity density n_{imp} . We focus here on the clean limit, $n_{\text{imp}} \approx 0$, in which case the self energy terms in Eq. (13) vanish. Ballistic transport has been demonstrated in suspended graphene²⁷ Suppression of charged impurity scattering in graphene on a substrate has been achieved by ionic screening of the graphene layer.^{28,29} We briefly discuss the implications of impurity scattering in Appendix A.

In the clean limit the kinetic equation is

$$\begin{aligned} & \frac{1}{2} \left[v_a^{A/B}, \tilde{\nabla} g^K \right]_+ + i \left[\omega^{A/B}, g^K \right]_- \\ & \mp \frac{i}{4\hbar} \left[\Lambda_{\pm} s_z, \frac{\hbar^2 v^2}{\epsilon_F^2 - \Lambda_{\pm}^2} \tilde{\nabla}^2 g^K \right]_- \approx 0. \end{aligned} \quad (15)$$

Following a previous calculation of the spin dynamics in a normal 2DEG,²⁶ we have defined the anomalous velocity

$$\mathbf{v}_a^{A/B} = v \left(\frac{2\epsilon_p}{\epsilon_F \pm \Lambda_{\pm} s_z} \hat{\mathbf{p}} - \frac{\Delta_R}{\epsilon_F \pm \Lambda_{\pm}} \boldsymbol{\eta} \right) \quad (16)$$

and the precession vector

$$\begin{aligned} \hbar \boldsymbol{\omega}^{A/B} = & -\frac{\epsilon_p \Delta_R}{\epsilon_F \pm \Lambda_{\pm}} \boldsymbol{\eta} \cdot \hat{\mathbf{p}} \\ & \mp \left(\frac{\epsilon_p^2 \pm \Delta_B^2}{\epsilon_F^2 - \Lambda_{\pm}^2} \Lambda_{\pm} + \frac{1}{2} \frac{\Delta_R^2}{\epsilon_F \pm \Lambda_{\pm}} - \Lambda_{\mp} \right) s_z, \end{aligned} \quad (17)$$

where $\epsilon_p = vp$, $\Delta_B = \sqrt{e\hbar v^2 |B|} \approx \sqrt{|B|/T} \times 25$ meV, and $\hat{\mathbf{p}}$ is the unit vector in the direction of \mathbf{p} .

The last term in the generalized gradient operator in Eq. (15),

$$\tilde{\nabla} = \nabla_{\mathbf{R}} - e(\mathbf{B} \times \nabla_{\mathbf{p}}) \quad (18)$$

generates the Lorentz force.

In the high doping limit $\epsilon_F \gg \Delta_I, \Delta_R, \Delta_Z$, where $\epsilon_p \approx \epsilon_F$, the velocity is independent of the SO coupling,

$$\mathbf{v}^{A/B} \approx 2v\hat{\mathbf{p}}. \quad (19)$$

However, the precession vector still depends on the SO parameters

$$\begin{aligned} \hbar \boldsymbol{\omega}^{A/B} = & -\Delta_R \boldsymbol{\eta} \cdot \hat{\mathbf{p}} \\ & - \left[2\Delta_Z + \left(\frac{\Delta_B}{\epsilon_F} \right)^2 (\Delta_I \pm \Delta_Z) \right] s_z. \end{aligned} \quad (20)$$

The spin precession governed by Δ_R is proportional to the direction of momentum. This is analogous to a normal 2DEG with Rashba SO interaction,²⁶ and in the presence of scattering will lead to spin relaxation by the DP mechanism. The out-of-plane component of the precession vector is governed by the Zeeman effect at low magnetic fields. At higher magnetic fields, there is a competition between the Zeeman energy Δ_Z and the intrinsic spin-orbit coupling. From the exact dispersion relation of graphene with SO coupling,^{9,14} one sees that at high doping the intrinsic SO coupling Δ_I contributes to second order, while Δ_R is a first order effect. This is reflected in Eq. (20), where Δ_I only contributes to the precession for strong magnetic fields at high doping.

Assuming that density variations occur on a length scale much longer than the Fermi wavelength, we can approximate the last term of Eq. (15) by

$$\begin{aligned} & \frac{i}{4\hbar} \left[\Lambda_{\pm} s_z, \frac{\hbar^2 v^2}{\epsilon_F^2 - \Lambda_{\pm}^2} \tilde{\nabla}^2 g^K \right]_- \\ & \approx \frac{i}{4} \left[\Lambda_{\pm} s_z, \frac{\hbar v^2 e^2 B^2}{\epsilon_F^2} \nabla_{\mathbf{p}}^2 g^K \right]_- \\ & = \frac{i}{4\hbar} \left(\frac{\Delta_B}{\epsilon_F} \right)^2 \Lambda_{\pm} \left[s_z, \frac{\hbar^2}{l_B^2} \nabla_{\mathbf{p}}^2 g^K \right]_-, \end{aligned} \quad (21)$$

where $l_B = \sqrt{\hbar/e|B|} \sim (|B|/T)^{-1/2} \times 25$ nm is the magnetic length. The contribution in Eq. (21) describes how the behavior of the system is modified for high magnetic fields when the magnetic length l_B becomes comparable to the Fermi wave length $\lambda_F^2 g^K \sim \hbar^2 \nabla_{\mathbf{p}}^2 g^K$, *i.e.* at the onset of Landau level quantization.

As can be seen from Eq. (20), the Zeeman energy

$$\Delta_Z = \frac{g\mu_B}{2} B \approx \frac{B}{T} \times 0.06 \text{ meV}, \quad (22)$$

competes with the intrinsic SO coupling for high magnetic fields. For a reasonable Fermi energy in doped graphene, $\epsilon_F \approx 100$ meV,³⁰ we get $(\Delta_B/\epsilon_F) \approx 0.25 \times |B|/T$. This means that the competition between the intrinsic SO coupling and the Zeeman effect will be difficult to detect, since Δ_Z will dominate Δ_I for magnetic fields where the competition between the two is noticeable. However, it is worth noting from Eq. (20) that in a strong magnetic field, spin precession is different on the two sublattices. The Zeeman energy and the intrinsic SO coupling are comparable in magnitude when $B \approx 0.4$ T, if the value $\Delta_I \sim 24$ μeV from the first-principles calculation is correct.¹⁰ To get a large contribution from this competition in the precession one needs

$\Delta_B/\epsilon_F \sim 1$, which corresponds to $|B| \approx 4$ T with the above Fermi energy. In this case the Zeeman energy is $\Delta_Z \sim 0.24$ meV $\approx 10\Delta_I$, so it is unlikely that the effect of Δ_I can be distinguished at high magnetic fields in doped graphene.

IV. CONCLUSION

In summary, the effect of SO coupling in highly doped graphene has several similarities with that in normal 2DEGs. As was discussed in Ref. 6, the Rashba spin-orbit coupling induces an in-plane component to the spin precession axis, which in the presence of scattering will lead to spin relaxation by the DP mechanism. We provided a way to see these effects directly by developing an effective 2×2 kinetic equation in spin space.

We find that the Rashba spin-orbit coupling Δ_R is the dominant contribution to the spin dynamics at high doping, while the intrinsic spin-orbit coupling Δ_I only contributes at large magnetic fields as a minor correction to the spin precession induced by the Zeeman splitting. These conclusions are based on effective stationary kinetic equations derived for the two sublattices in highly doped graphene, where we have taken into account both intrinsic and extrinsic spin-orbit coupling, and also the effect of a perpendicular magnetic field through the Zeeman effect and an orbital contribution. We assume values for the spin-orbit coupling constants as reported in a recent first-principles calculation.¹⁰

Further work is needed to clarify the respective roles of the two spin-orbit mechanisms in graphene at low densities. At such densities, the formalism used here becomes cumbersome, and it would be better to start directly from the 8×8 Hamiltonian in spin, sublattice and valley space (1). A detailed calculation of the self energy in the presence of spin-orbit coupling, comparing short-range and long-range disorder potentials, would provide valuable insight into the possible importance of the EY mechanisms in graphene.

ACKNOWLEDGMENTS

We thank Eugene Mischchenko for valuable discussions. This work was supported by Research Council of Norway through grant no. 167498/V30.

Appendix A: Effect of impurities

In this appendix we briefly outline the effect of impurities in the kinetic equation. We consider the dilute limit, and evaluate the self energy matrix in the Born approximation for the situation without a magnetic field. The terms containing the gradient of the impurity potential in Eq. (7) are seen to give rise to an anisotropic momentum relaxation rate.

The Fermi wave length λ_F in doped graphene is typically 50 – 100 nm.³¹ Impurity scattering in graphene is dominated by charged impurities trapped a small distance L away from the graphene layer.^{9,20,32} This corresponds to a quasi short-range regime, where the characteristic length scale $L \sim Q^{-1}$ associated with impurity scattering is smaller than the Fermi wave length, but still larger than the lattice constant, so that

$$k_F \ll Q \ll K, \quad (\text{A1})$$

where $K \sim a^{-1}$ is the momentum transfer associated with inter-valley scattering, and $a = 2.461$ Å is the lattice constant of graphene.³³ In the regime of Eq. (A1), we can model the impurities as short-range scatterers on the scale of the Fermi wave length, $V(\mathbf{r}) = \sum_i \alpha \delta(\mathbf{r} - \mathbf{R}_i)$, neglecting any valley mixing.³⁴ We also neglect the modulation of Δ_R induced by the local electric field variations due to the impurities,⁹ assuming that the back gate which is used to adjust the doping dominates Δ_R .

The self energy in the self-consistent Born approximation is^{35,36}

$$\tilde{\Sigma}(1, 2) = \langle U(\mathbf{r}_1) \check{G}(1, 2) U(\mathbf{r}_2) \rangle_{\text{imp}}, \quad (\text{A2})$$

where $U(\mathbf{r}) = U^V(\mathbf{r}) + U^{\partial V}(\mathbf{r})$ has contributions from the two last terms in Eq. (7). The first term $U^V(\mathbf{r}) = V(\mathbf{r})$ gives rise to the regular self energy,

$$\check{\Sigma}_\epsilon^{[VV]}(\mathbf{R}) = n_{\text{imp}} |\alpha|^2 \int \frac{d\mathbf{q}}{(2\pi)^2} \check{g}_{\mathbf{q}\epsilon}(\mathbf{R}), \quad (\text{A3})$$

which is independent of momentum.

The term proportional to the derivative of the impurity potential,

$$U^{\partial V}(\mathbf{r}) = \frac{-i\hbar v [\partial_\mp V(\mathbf{r})]}{[\epsilon_F \pm \Lambda_\pm s_z]^2} (v\bar{p}_\pm \mp i\Delta_R s_\pm), \quad (\text{A4})$$

leads in general to an anisotropic self energy through the term $v\bar{p}_\pm$, and to spin flip processes due to $\Delta_R s_\pm$. The latter will contribute to EY relaxation. At high doping, however, the spin flip contribution is highly suppressed due to the small prefactor Δ_R/ϵ_F .

In the absence of a magnetic field at high doping, and neglecting gradients of $g_{\mathbf{q}\epsilon_F}(\mathbf{R})$, we find that the contri-

butions to the anisotropic part of the self energy are

$$\begin{aligned} \check{\Sigma}_{\mathbf{q}\epsilon_F}^{[\partial V\partial V]} &= \left\langle [U_{\partial V}\check{G}U_{\partial V}]_{\mathbf{q}\epsilon_F} \right\rangle_{\text{imp}} \\ &\approx n_{\text{imp}} |\alpha|^2 \\ &\times \int \frac{d\mathbf{k}}{(2\pi)^2} \frac{(\hbar v)^4 [(\mathbf{q} - \mathbf{k})^2 k^2]}{\epsilon_F^4} \check{g}_{\mathbf{k}\epsilon_F}, \end{aligned} \quad (\text{A5})$$

$$\begin{aligned} \check{\Sigma}_{\mathbf{q}\epsilon_F}^{[V\partial V]} &= \left\langle [U_V\check{G}U_{\partial V}]_{\mathbf{q}\epsilon_F} \right\rangle_{\text{imp}} \\ &\approx n_{\text{imp}} |\alpha|^2 \\ &\times \int \frac{d\mathbf{k}}{(2\pi)^2} \frac{(\hbar v)^2 [(\mathbf{q} - \mathbf{k}) \cdot \mathbf{k} \mp i(\mathbf{q} \times \mathbf{k})]}{\epsilon_F^2} \check{g}_{\mathbf{k}\epsilon_F}, \end{aligned} \quad (\text{A6})$$

$$\begin{aligned} \check{\Sigma}_{\mathbf{q}\epsilon_F}^{[\partial VV]} &= \left\langle [U_{\partial V}\check{G}U_V]_{\mathbf{q}\epsilon_F} \right\rangle_{\text{imp}} \\ &\approx n_{\text{imp}} |\alpha|^2 \\ &\times \int \frac{d\mathbf{k}}{(2\pi)^2} \frac{(\hbar v)^2 [(\mathbf{q} - \mathbf{k}) \cdot \mathbf{k} \pm i(\mathbf{q} \times \mathbf{k})]}{\epsilon_F^2} \check{g}_{\mathbf{k}\epsilon_F}. \end{aligned} \quad (\text{A7})$$

The dominant contribution to the self energy at high doping is therefore

$$\begin{aligned} \check{\Sigma}_{\mathbf{q}\epsilon_F} &= \check{\Sigma}_{\mathbf{q}\epsilon_F}^{[VV]} + \check{\Sigma}_{\mathbf{q}\epsilon_F}^{[V\partial V]} + \check{\Sigma}_{\mathbf{q}\epsilon_F}^{[\partial VV]} + \check{\Sigma}_{\mathbf{q}\epsilon_F}^{[\partial V\partial V]} \\ &\approx n_{\text{imp}} |\alpha|^2 \int \frac{d\mathbf{k}}{(2\pi)^2} f(\mathbf{q}, \mathbf{k}) \check{g}_{\mathbf{k}\epsilon_F}, \end{aligned} \quad (\text{A8})$$

with

$$\begin{aligned} f(\mathbf{q}, \mathbf{k}) &= 1 + 2 \left(\frac{\hbar v}{\epsilon_F} \right)^2 (\mathbf{q} - \mathbf{k}) \cdot \mathbf{k} \\ &+ \left(\frac{\hbar v}{\epsilon_F} \right)^4 (\mathbf{q} - \mathbf{k})^2 k^2. \end{aligned} \quad (\text{A9})$$

With the Hamiltonian in Eq. (7), the retarded Green's function has the general structure

$$g_{\mathbf{k}\epsilon_F}^R = A_{\epsilon_F}(k) + B_{\epsilon_F}(k) \boldsymbol{\eta} \cdot \mathbf{k} + C_{\epsilon_F}(k) s_z, \quad (\text{A10})$$

where $k = |\mathbf{k}|$. We can perform the angular integrals in Eq. (A8), finding

$$\begin{aligned} \begin{bmatrix} I_A \\ I_C \end{bmatrix} (k, \mathbf{q}) &= \int \frac{d\Omega(\mathbf{k})}{(2\pi)^2} f(\mathbf{q}, \mathbf{k}) \begin{bmatrix} A_{\epsilon_F} \\ C_{\epsilon_F} \end{bmatrix} (k) \\ &= \frac{1}{2\pi} [1 + \nu_k^2 (\nu_k^2 + \nu_q^2 - 2)] \begin{bmatrix} A_{\epsilon_F} \\ C_{\epsilon_F} \end{bmatrix} (k), \end{aligned} \quad (\text{A11})$$

$$\begin{aligned} I_B(k, \mathbf{q}) &= \int \frac{d\Omega(\mathbf{k})}{(2\pi)^2} f(\mathbf{q}, \mathbf{k}) B_{\epsilon_F}(k) \boldsymbol{\eta} \cdot \mathbf{k} \\ &= \frac{1}{2\pi} [\nu_k^2 (1 - \nu_k^2)] B_{\epsilon_F}(k) \boldsymbol{\eta} \cdot \mathbf{q}, \end{aligned} \quad (\text{A12})$$

where ν_q and ν_k are defined as $\nu_k = \epsilon_k/\epsilon_F = \hbar v k/\epsilon_F$. The term in Eq. (A12) shows that the curvature terms in the effective Hamiltonian (7) lead to an anisotropic momentum relaxation rate. The spin dependence of the scattering rate associated with the anisotropy will lead to spin relaxation via the EY mechanism.

- ¹ A. H. Castro Neto, F. Guinea, N. M. R. Peres, K. S. Novoselov, and A. K. Geim, *Rev. Mod. Phys.*, **81**, 109 (2009).
- ² A. K. Geim and K. S. Novoselov, *Nature Materials*, **6**, 183 (2007).
- ³ N. Tombros, C. Jozsa, M. Popinciuc, H. T. Jonkman, and B. J. van Wees, *Nature*, **448**, 571 (2007).
- ⁴ M. Popinciuc, C. Józsa, P. J. Zomer, N. Tombros, A. Veligura, H. T. Jonkman, and B. J. van Wees, *Phys. Rev. B*, **80**, 214427 (2009).
- ⁵ I. Žutić, J. Fabian, and S. Das Sarma, *Rev. Mod. Phys.*, **76**, 323 (2004).
- ⁶ D. Huertas-Hernando, F. Guinea, and A. Brataas, *Phys. Rev. Lett.*, **103**, 146801 (2009).
- ⁷ Y. Zhou and M. W. Wu, *Phys. Rev. B*, **82**, 085304 (2010), 1004.0638.
- ⁸ N. Tombros, S. Tanabe, A. Veligura, C. Jozsa, M. Popinciuc, H. T. Jonkman, and B. J. van Wees, *Phys. Rev. Lett.*, **101**, 046601 (2008).
- ⁹ C. Ertler, S. Konschuh, M. Gmitra, and J. Fabian, *Phys. Rev. B*, **80**, 041405 (2009), 0905.0424.
- ¹⁰ M. Gmitra, S. Konschuh, C. Ertler, C. Ambrosch-Draxl, and J. Fabian, *Phys. Rev. B*, **80**, 235431 (2009).
- ¹¹ C. Józsa, T. Maassen, M. Popinciuc, P. J. Zomer, A. Veligura, H. T. Jonkman, and B. J. van Wees, *Phys. Rev. B*, **80**, 241403 (2009).
- ¹² K. Pi, W. Han, K. M. McCreary, A. G. Swartz, Y. Li, and R. K. Kawakami, *Phys. Rev. Lett.*, **104**, 187201 (2010).
- ¹³ E. I. Rashba, "Graphene with structure-induced spin-orbit coupling: Spin-polarized states, spin zero modes, and quantum hall effect," (2009), preprint, 0902.3806.
- ¹⁴ C. L. Kane and E. J. Mele, *Phys. Rev. Lett.*, **95**, 226801 (2005).
- ¹⁵ D. Huertas-Hernando, F. Guinea, and A. Brataas, *Phys. Rev. B*, **74**, 155426 (2006).
- ¹⁶ H. Min, J. E. Hill, N. A. Sinitsyn, B. R. Sahu, L. Kleinman, and A. H. MacDonald, *Phys. Rev. B*, **74**, 165310 (2006).
- ¹⁷ J. Rammer, *Quantum Transport Theory* (Perseus Books, 1998).
- ¹⁸ J. Rammer and H. Smith, *Rev. Mod. Phys.*, **58**, 323 (1986).
- ¹⁹ I. L. Aleiner and K. B. Efetov, *Phys. Rev. Lett.*, **97**, 236801 (2006).
- ²⁰ S. Adam and S. Das Sarma, **146**, 356 (2008), ISSN 0038-1098.
- ²¹ A. Deshpande, W. Bao, F. Miao, C. N. Lau, and B. J. LeRoy, *Phys. Rev. B*, **79**, 205411 (2009).
- ²² F. Simon, F. Muranyi, and B. Dora, "Electron spin dynamics and electron spin resonance in graphene," (2010),

- arXiv:1004.0210, 1004.0210.
- ²³ A. H. Castro Neto and F. Guinea, *Phys. Rev. Lett.*, **103**, 026804 (2009).
- ²⁴ I. Gierz, J. H. Dil, F. Meier, B. Slomski, J. Osterwalder, J. Henk, R. Winkler, C. R. Ast, and K. Kern, "Giant anisotropic spin splitting in epitaxial graphene," (2010), arxiv:1004.1573, 1004.1573.
- ²⁵ A. Varykhalov, J. Sánchez-Barriga, A. M. Shikin, C. Biswas, E. Vescovo, A. Rybkin, D. Marchenko, and O. Rader, *Phys. Rev. Lett.*, **101**, 157601 (2008).
- ²⁶ E. G. Mishchenko, A. V. Shytov, and B. I. Halperin, *Phys. Rev. Lett.*, **93**, 226602 (2004).
- ²⁷ X. Du, I. Skachko, A. Barker, and E. Y. Andrei, *Nature Nanotechnology*, **3**, 491 (2008), ISSN 1748-3387.
- ²⁸ F. Chen, J. Xia, and N. Tao, *Nano Lett.*, **9**, 1621 (2009).
- ²⁹ F. Chen, J. Xia, D. K. Ferry, and N. Tao, *Nano Lett.*, **9**, 2571 (2009).
- ³⁰ Y. Zhang, Y.-W. Tan, H. L. Stormer, and P. Kim, *Nature*, **438**, 201 (2005).
- ³¹ M. I. Katsnelson, K. S. Novoselov, and A. K. Geim, *Nature Physics*, **2**, 620 (2006).
- ³² K. Nomura and A. H. MacDonald, *Phys. Rev. Lett.*, **98**, 076602 (2007).
- ³³ S. Reich, J. Maultzsch, C. Thomsen, and P. Ordejón, *Phys. Rev. B*, **66**, 035412 (2002).
- ³⁴ N. H. Shon and T. Ando, *J. Phys. Soc. Jpn.*, **67**, 2421 (1998).
- ³⁵ G. D. Mahan, *Many-Particle Physics*, 3rd ed. (Kluwer Academic/Plenum Publishes, New York, 2000).
- ³⁶ H. Bruus and K. Flensberg, *Many-Body Quantum Theory in Condensed Matter Physics*, Oxford Graduate Texts (Oxford University Press, 2004) ISBN 0198566336.

Paper [3]

Crossed Andreev reflection versus electron transfer in three-terminal graphene devices

Physical Review B **81**, 174523 (2010)

Crossed Andreev reflection versus electron transfer in three-terminal graphene devices

Håvard Haugen, Daniel Huertas-Hernando, and Arne Brataas

Department of Physics, Norwegian University of Science and Technology, N-7491 Trondheim, Norway

Xavier Waintal

SPSMS-INAC-CEA, 17 rue des Martyrs, 38054 Grenoble Cedex 9, France

(Received 28 September 2009; revised manuscript received 25 February 2010; published 24 May 2010)

We investigate the transport properties of three-terminal graphene devices, where one terminal is superconducting and two are normal metals. The terminals are connected by nanoribbons. Electron transfer (ET) and crossed Andreev reflection (CAR) are identified via the nonlocal signal between the two normal terminals. Analytical expressions for ET and CAR in symmetric devices are found. We compute ET and CAR numerically for asymmetric devices. ET dominates CAR in symmetric devices, but CAR can dominate ET in asymmetric devices, where only the zero-energy modes of the zigzag nanoribbons contribute to the transport.

DOI: [10.1103/PhysRevB.81.174523](https://doi.org/10.1103/PhysRevB.81.174523)

PACS number(s): 74.45.+c, 73.63.-b, 73.23.-b, 74.25.F-

I. INTRODUCTION

Graphene, a two-dimensional honeycomb lattice of carbon atoms, has recently been experimentally realized.¹⁻³ It exhibits intriguing electron transport properties such as a very high mobility,¹⁻³ gate-voltage tunable electron doping,¹ anomalous quantum Hall effect,³ Klein tunneling,⁴ “relativistic” Dirac-like linear energy-momentum dispersion,⁵ and possible integration with other adatoms and electrical contacts.^{6,7} Graphene can be contacted to superconductors and a supercurrent in graphene Josephson junctions has been measured.⁸⁻¹⁰

Nonlocal transport in three-terminal devices with one superconducting lead and two normal metals has been extensively studied, both theoretically¹¹⁻¹⁶ and experimentally.¹⁷⁻²⁰ At energies lower than the superconducting gap, the current in one normal terminal caused by a voltage applied between another normal terminal and the superconductor is governed by a competition between electron transfer (ET) and crossed Andreev reflection (CAR). ET is the emission of an electron from one normal metal terminal to another normal metal terminal, possibly after interacting with the superconductor. In CAR, an electron from one normal terminal enters the superconductor together with an electron from a second normal terminal or, equivalently, an electron is emitted into one normal terminal while a hole is emitted into another normal terminal. This process creates a spatially entangled electron-hole pair which has a fundamental interest and can be used as an entangler.²¹⁻²³ The relative magnitude of ET and CAR can be tuned by using ferromagnetic contacts,^{14,24} but our focus here is on their intrinsic relative value when normal metals are used. The ET and CAR processes contribute with opposite signs to the nonlocal current. Experimentally, it has been measured that ET often dominates CAR, but at finite bias voltage a CAR dominated signal²⁰ was also seen. First theories in the lowest order tunneling limit predict that ET and CAR exactly cancel each other.¹⁴ Also, relaxing the assumption of tunneling barriers by allowing barriers of arbitrary strength in semiclassical N-S circuits, ET generally dominates CAR.¹⁵ Recent theoretical suggestions to explain the experiment in Ref. 20 are Coulomb interaction effects,²⁵ an external ac bias,²⁶ and quantum interference effects.²⁷

Theoretically, graphene-superconductor junctions have been investigated by several workers.²⁸⁻³⁰ In graphene there is an additional new quasiparticle to supercurrent conversion process denoted specular Andreev reflection, where states above and below the Dirac point are coupled by Andreev scattering (interband coupling).²⁸ In specular Andreev reflection, the holes emitted from the superconductor no longer follow the parallel time-reversed path of the incoming electron as they do in direct Andreev reflection, but are specularly reflected at an angle which equals the angle of incidence. Although fundamentally interesting, as it could enhance CAR processes,^{31,32} specular Andreev reflection is only visible in ultra clean and homogeneous systems, since the Dirac point must be well-defined throughout the region of interest, or the superconducting pair potential Δ must be much larger than the typical variation in the Dirac point. Also, it is necessary to control the doping such that the Fermi energy is considerably smaller than the superconducting gap. The small magnitude of the proximity induced superconducting gap in graphene, $\Delta \approx 0.1$ meV,⁸ means this could only be realized in ultra small structures at very low doping level in well controlled systems.

In this paper we investigate the influence of a superconducting terminal on devices built from graphene zigzag ribbons. We are interested in studying how ET and CAR depend on the features of the nanoribbons *e.g.* on their widths, number of terminals, and relative angle where ribbons connected to various terminals intersect. The choice of zigzag ribbons is the most relevant one, as the boundary conditions for ribbons with generic boundaries have been shown to reduce to the boundary conditions for zigzag terminations in most cases.^{33,34} Such nanoribbons have some unique electronic features, such as supporting current carrying zero-modes localized along the edges.³⁴⁻³⁶ Also, for low energies, states carrying current in opposite directions along the zigzag ribbon is associated with different eigenstates, and there is an absence of backscattering due to the small overlap between the states carrying current in opposite directions.³⁷

The paper is organized as follows: in Sec. II we define our model and in Sec. III we express the scattering matrix in terms of the normal-state scattering matrix. This enables us to identify the ET and CAR contributions to the nonlocal

signal. Section IV describes the properties of symmetric three-terminal devices, and in Sec. VI we present numerical results showing a dominance of CAR over ET in an asymmetric device. Finally we conclude our paper in Sec. VII.

II. MODEL AND METHOD

Our description of superconducting ribbons starts with the nearest-neighbor hopping Hamiltonian of graphene,

$$H = - \sum_{\langle i,j \rangle, \sigma} \gamma c_{i\sigma}^\dagger c_{j\sigma} - E_F \sum_{i,\sigma} c_{i\sigma}^\dagger c_{i\sigma}, \quad (1)$$

where $\gamma \approx 2.7$ eV is the nearest-neighbor hopping energy,^{7,38,39} and $c_{i\sigma}^\dagger$ creates an electron with spin σ at site i . In the superconducting terminal, we assume a superconductor on top of the graphene sheet which by proximity induces superconducting properties in graphene. We consider spin singlet pairing described by the BCS Hamiltonian \hat{H} .⁴⁰ The superconducting pair potential Δ_i is local to site i and chosen to be real since we only have one superconductor. We write \hat{H} in Nambu form

$$\hat{H} = \sum_{i,j} \Psi_j^\dagger \left[\begin{pmatrix} H_{ij} & 0 \\ 0 & -H_{ij}^* \end{pmatrix} + \delta_{ij} \begin{pmatrix} 0 & \Delta_i \\ \Delta_i & 0 \end{pmatrix} \right] \Psi_i, \quad (2)$$

where $\Psi_i^\dagger = (c_{i,1}^\dagger, c_{i,-1})$ and H_{ij} are elements of the normal-state Hamiltonian in Eq. (1).

We are interested in the transport properties which can be expressed via the scattering matrix of the system. Following Ref. 41, we find that the differential conductance matrix is⁴²

$$G_{ab}(eV_b) = (-1)^{(1-\delta_{ab})} \left. \frac{\partial I_a}{\partial V_b} \right|_{V_b} = \begin{cases} N_b - G_{bb}^{\text{ER}} + G_{bb}^{\text{DAR}}, & b = a \\ G_{ab}^{\text{ET}} - G_{ab}^{\text{CAR}}, & a \neq b, \end{cases} \quad (3)$$

where $N_b(\varepsilon)$ is the number of propagating modes in lead b at energy ε , and the conductance matrix elements are defined in terms of the Nambu space scattering matrix

$$S = \begin{pmatrix} S^{ee} & S^{eh} \\ S^{he} & S^{hh} \end{pmatrix} \quad (4)$$

as

$$G_{bb}^{\text{ER}} = \text{Tr}[S_{bb}^{ee}(eV_b)S_{bb}^{e\dagger}(eV_b)], \quad (5)$$

$$G_{bb}^{\text{DAR}} = \text{Tr}[S_{bb}^{he}(eV_b)S_{bb}^{h\dagger}(eV_b)], \quad (6)$$

$$G_{ab}^{\text{ET}} = \text{Tr}[S_{ab}^{ee}(eV_b)S_{ab}^{e\dagger}(eV_b)], \quad (a \neq b), \quad (7)$$

$$G_{ab}^{\text{CAR}} = \text{Tr}[S_{ab}^{he}(eV_b)S_{ab}^{h\dagger}(eV_b)], \quad (a \neq b). \quad (8)$$

The conductances in Eqs. (5)–(8) describe, respectively, local electron reflection (ER), direct Andreev reflection (DAR), nonlocal ET, and CAR.

All energies are measured with respect to the equilibrium chemical potential of the superconductor, and all conduc-

tances in this paper are in units of two times (for spin) the conductance quantum $2G_0 = 2e^2/h$. The current I_a is defined as incoming from reservoir a .

III. SCATTERING MATRIX OF A THREE-TERMINAL DEVICE WITH ONE SUPERCONDUCTING TERMINAL

In the following we will study the nonlocal signal in a three-terminal device, where terminal 1 is superconducting and terminals 2 and 3 are normal metals. The nonlocal conductance^{14,15}

$$G_{32}(eV_2) = G_{32}^{\text{ET}}(eV_2) - G_{32}^{\text{CAR}}(eV_2) \quad (9)$$

is positive when dominated by ET and negative when dominated by CAR.

We compute G_{32}^{CAR} and G_{32}^{ET} in two ways: (i) S^{ee} and S^{he} are computed directly in Nambu space using the Hamiltonian (2), and G_{32}^{CAR} and G_{32}^{ET} are found from Eqs. (7) and (8). We refer to this as the *Nambu* approach. (ii) We relate S^{ee} and S^{he} to the scattering matrix s in the normal state and numerically compute the latter using the Hamiltonian (1). We call this the *Normal* approach. Our results using both methods agree when applicable. Let us first review how the scattering matrix can be related to the normal-state properties.

Following Ref. 43, if the scattering region is well separated from the superconducting terminal, we can express the scattering matrix S when terminal 1 is superconducting in terms of the scattering matrix

$$s = \begin{pmatrix} s_{11} & s_{12} & s_{13} \\ s_{21} & s_{22} & s_{23} \\ s_{31} & s_{32} & s_{33} \end{pmatrix} = \begin{pmatrix} r_{11} & t_{12} & t_{13} \\ t_{21} & r_{22} & t_{23} \\ t_{31} & t_{32} & r_{33} \end{pmatrix} \quad (10)$$

when the whole device is in the normal state. As long as the device is appreciably smaller than the superconducting coherence length ξ , the normal approach is applicable. For graphene, the induced superconducting gap is small, $\Delta \sim 0.1$ meV,⁸ so that the coherence length ξ is on the order of micrometers.

With terminal 1 superconducting, the scattering matrix between the normal metal terminals 3 and 2 is^{43,44}

$$S_{32}^{ee} = t_{32} + t_{31} \nu^2 \bar{r}_{11} M t_{12}, \quad (11)$$

$$S_{32}^{he} = \bar{t}_{31} \nu M t_{12}, \quad (12)$$

where the matrix M is

$$M = [I - \nu^2 r_{11} \bar{r}_{11}]^{-1}. \quad (13)$$

The amplitude ν , associated with electron-hole conversion at the normal-superconducting interface, is⁴⁴

$$\nu = \frac{\varepsilon}{\Delta} - \text{sgn}(\varepsilon) \sqrt{\left(\frac{\varepsilon}{\Delta}\right)^2 - 1}, \quad (14)$$

and the bar (\bar{g}) corresponds to time reversal, defined for an arbitrary quantity $g(\varepsilon)$ as

$$\bar{g} = \bar{g}(\varepsilon) = g^*(-\varepsilon). \quad (15)$$

The matrix M corresponds to all orders of the process where a hole emitted from the superconductor returns to the

superconductor. At zero energy, holes propagating with amplitude \bar{r}_{11} between successive interactions with the superconductor retrace exactly the reverse path of the electrons with amplitude r_{11} . Thus, at zero energy, holes and electrons do not acquire a phase relative to each other upon interacting with the scattering region. However, at nonzero energy, there is a mismatch between the wave vectors of electronlike and holelike states, so the time reverse paths described by the scattering matrices r_{11} and \bar{r}_{11} will not be exactly opposite to each other. This means that the term $r_{11}\bar{r}_{11}$ in M contains many different phases, which will depend strongly on the disorder configuration. There is therefore some loss of coherence at nonzero energy due to phase randomization.

For the ET process, described by the scattering matrix element in Eq. (11), there is an interference of two types of processes: (1) Going directly from 2 to 3 without interacting with the superconductor, and (2) processes involving any number of electron-hole-electron conversions at the interface to the superconductor. Similarly, the Andreev process described by Eq. (12) involves an odd number of electron-hole conversions at the NS interface.

In the absence of a magnetic field, time-reversal symmetry dictates⁴⁵

$$\bar{s}_{ab}(\varepsilon) = s_{ab}^*(-\varepsilon) = s_{ba}^\dagger(-\varepsilon). \quad (16)$$

The energy scale of the normal-state scattering matrix s_{ab} is the subband energy, which is determined by the hopping energy γ and the width of the ribbon. For the ribbons considered in this paper, the subband energy is larger than the superconducting pair potential Δ by several orders of magnitude. The Fermi energy is comparable to the subband energies in magnitude. Since, in the regime we consider, s_{ab} is independent of energy on the scale of Δ , we write $s_{ab}(\varepsilon) = s_{ab}(0) = s_{ab}$ and $\bar{s}_{ab} = s_{ba}^\dagger$.

The nonlocal ET and CAR conductances therefore simplify to

$$G_{32}^{\text{ET}} = \text{Tr}[t_{32}t_{32}^\dagger] + 2 \text{Re } \nu^2 \text{Tr}[t_{12}t_{32}^\dagger t_{31}r_{11}^\dagger M] + |\nu|^4 \text{Tr}[r_{11}t_{31}^\dagger t_{31}r_{11}^\dagger M t_{12}t_{12}^\dagger M^\dagger], \quad (17)$$

$$G_{32}^{\text{CAR}} = |\nu|^2 \text{Tr}[t_{13}t_{13}^\dagger M t_{12}t_{12}^\dagger M^\dagger], \quad (18)$$

where all energy dependence is due to the electron-hole conversion amplitude ν .

When $\varepsilon \gg \Delta$, Eq. (14) gives $\nu \rightarrow 0$, and we recover the normal-state behavior where only the first term of Eq. (17) contributes. However, in the subgap limit $\varepsilon \ll \Delta$, $\nu \rightarrow i$, and the interaction with the superconductor contributes. The second term in Eq. (17) is due to interference between processes involving direct transfer of electrons from 2 to 3, and interaction with the superconducting terminal 1.

In our numerical studies, we calculate the retarded Green's-function matrix $\mathcal{G} = [E\hat{I} - \hat{H} - \hat{\Sigma}^R]^{-1}$ and extract the elements \mathcal{G}_{ab} involving the terminals a and b . The calculation of \mathcal{G} uses the recursive method described in Ref. 46. In this method, the Green's function of the whole system is found by adding the sites of the Hamiltonian (1) to the system one by one, updating all relevant Green's-function elements via the Dyson equation. The method has the advantage that it

can easily be applied to structures of arbitrary geometry and any number of terminals. After the Green's function has been found, the scattering matrix S_{ab} is extracted via the Fischer-Lee relations,^{45,47}

$$S_{ab} = -\mathcal{I}_a \delta_{ab} + i\Gamma_a^{1/2} \mathcal{G}_{ab} \Gamma_b^{1/2}. \quad (19)$$

Here \mathcal{I}_a is the identity matrix (operator) and $\Gamma_a = i(\Sigma_a - \Sigma_a^\dagger)$ is the linewidth matrix which depends on the self energy Σ_a of terminal a .

IV. SYMMETRIC THREE-TERMINAL DEVICE

The simplest three-terminal device is completely symmetric where the normal-state scattering matrix [Eq. (10)] simplifies to

$$s = \begin{pmatrix} r & t & t \\ t & r & t \\ t & t & r \end{pmatrix}. \quad (20)$$

Unitarity of s gives rise to the relations

$$I = rr^\dagger + 2tt^\dagger \quad (21)$$

and

$$0 = tr^\dagger + rt^\dagger + tt^\dagger \quad (22)$$

that we make use of in Eqs. (17) and (18) to find the nonlocal conductance. We can express the conductance matrix of such a symmetric device in terms of the eigenvalues $0 \leq R_n \leq 1$ of the reflection probability matrix rr^\dagger ,

$$G_{32}^{\text{ET}} = \sum_n \frac{(1-R_n)}{4(1+R_n)^2} (3+5R_n), \quad (23)$$

$$G_{32}^{\text{CAR}} = \sum_n \frac{(1-R_n)^2}{4(1+R_n)^2}. \quad (24)$$

It follows from this that the nonlocal conductance of a symmetric structure,

$$G_{32} = G_{32}^{\text{ET}} - G_{32}^{\text{CAR}} = \sum_n \frac{(1-R_n)}{2(1+R_n)^2} (1+3R_n), \quad (25)$$

is always ET dominated (positive). By a completely analogous calculation we also find that the local conductance,

$$G_{22} = \sum_n \frac{(1-R_n)}{2(1+R_n)^2} [3+R_n(2-R_n)], \quad (26)$$

is naturally also positive.

A few simple conclusions can be drawn from these expressions. First, when the device is perfectly transparent for the N_2 contributing modes at the Fermi energy, the contributing modes have $R_n \approx 0$, the others have $R_n \approx 1$. The local and nonlocal conductances become

$$G_{22} \approx \frac{3}{2} N_2, \quad (27)$$

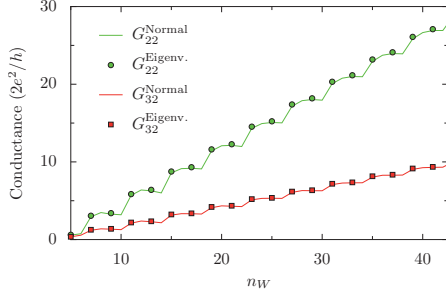


FIG. 1. (Color online) Local and nonlocal conductance of a symmetric device as a function of the ribbon width n_W . Comparing calculations done directly from the scattering matrix (lines) with calculations using the eigenvalues of the reflection matrix (symbols), we see that the two methods give identical results.

$$\bar{G}_{32} \approx \frac{1}{2}N_2, \quad (28)$$

where N_2 is the number of modes contributing to the current at the Fermi energy. These results have the following simple explanation: when the voltage is raised in terminal 2, N_2 conducting modes are injected into the structure via this terminal. Since the device is symmetric, half of these modes go directly to terminal 3, producing a current $N_2/2$ in this terminal. The other half of the N_2 incoming modes interact with the superconductor at terminal 1, and are Andreev reflected back to terminal 2 as holes. These modes contribute $2(N_2/2)$ to the current in terminal 2. The total current in terminal 2 is therefore $(2+1)(N_2/2) = 3/2N_2$. At low bias the Andreev reflected holes retrace exactly the trajectory of the incoming electrons because of time-reversal symmetry, and they therefore only contribute to the current in terminal 2.

When all the terminals are connected to the central device with tunnel contacts, we can expand the local and nonlocal conductances in the $\delta = (1 - R_n)/2 \ll 1$ for the contributing modes. We find that

$$G_{22} = N_2\delta + O(\delta^2), \quad (29)$$

$$G_{32} = N_2\delta + O(\delta^2), \quad (30)$$

so we recover the normal-state results, where both the local and nonlocal signals vanish linearly with δ . Transport between terminals 2 and 3 involving the superconductor involves higher orders in δ and does therefore not contribute in this limit.

We check the consistency between eigenvalue expressions (25) and (26) and our numerical routines by calculating the local and nonlocal conductances G_{22} and G_{32} in a symmetric three-terminal graphene device, as explained further in Sec. V. As can be seen from Fig. 1, where the conductances are plotted as a function of the width n_W of the nanoribbons, we have excellent agreement between the eigenvalue expressions (symbols) and the results found directly from Eq. (3) (lines). Note that Eq. (3) is valid for any width n_W , while only even n_W give a truly symmetric device when built from

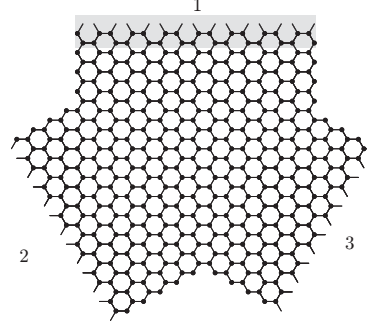


FIG. 2. Three-terminal graphene fork consisting of three semi-infinite graphene zigzag nanoribbons connected together. The top lead is allowed to become superconducting by inserting a nonzero pair potential Δ in this region, according to the Hamiltonian in Eq. (2).

zigzag nanoribbons, so only such data points are shown. However, we find that the results found from using the eigenvalue expressions when n_W is odd are also very close to the numerical results. This is not surprising since as long as many modes contribute to the current, small alterations of the geometry should not have a big impact on the total current.

V. ASYMMETRIC THREE-TERMINAL DEVICE

Having found that ET dominates nonlocal transport in a symmetric device, we turn our investigation to asymmetric devices. We do this numerically, by calculating the scattering matrix in a three-terminal device obtained by joining three semi-infinite zigzag graphene nanoribbons as shown in Fig. 2.

The width of a zigzag graphene nanoribbon, $W = \sqrt{3}an_W/2$, is determined by the minimal number of bonds n_W that must be broken to cut the ribbon.³⁵ a is the lattice constant of graphene, $a = 2.46 \text{ \AA}$.³⁹

For a wide ribbon, $n_W \gg 1$, the energy of the m th transverse subband is to a good approximation⁴⁸

$$E_m = \left(m + \frac{1}{2}\right) \frac{\pi\gamma}{n_W}, \quad m = 1, 2, \dots, \quad (31)$$

where γ is the nearest-neighbor hopping energy on the graphene lattice. The superconducting coherence length

$$\xi = \frac{\hbar v_F}{\Delta} = \frac{\sqrt{3}}{2} \frac{\gamma}{\Delta} a \quad (32)$$

will typically be of the order of micrometers, so the normal approach should be applicable for nanoribbons up to $1 \mu\text{m}$ wide or $n_W \sim 10^4$.

A. Consistency checks

In Fig. 3 we compare the conductance extracted from the normal-state scattering matrix s to that found by direct evalu-

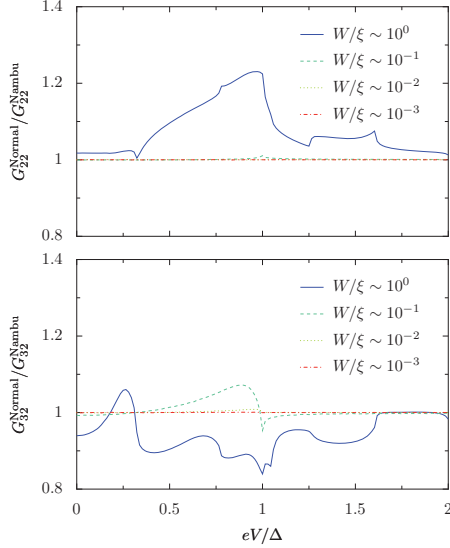


FIG. 3. (Color online) Ratio of conductance calculated with the normal method (extracted from the normal-state scattering matrix) to conductance calculated directly with the Nambu space Hamiltonian. When $W \ll \xi$ the two methods give identical results. The situation considered in this paper corresponds to $W/\xi \sim 10^{-4}$. Upper (lower) panel: local (nonlocal) conductance.

ation of the full scattering matrix S in Nambu space. The calculations are done for a device of the type shown in Fig. 2. The leads are all semi-infinite zigzag ribbons, and we set $\Delta=0$ everywhere except in terminal 1 (shaded area in Fig. 2). As can be seen from Fig. 3, where we show the ratio between the conductance calculated with the two methods, $G_{ij}^{\text{Normal}}/G_{ij}^{\text{Nambu}}$, the agreement between the two methods is excellent as long as $W/\xi \ll 10^{-1}$, where W is the width of the ribbons and ξ is the superconducting coherence length.

Also, since $\xi \gg W$, the exact position of the boundary between the normal ($\Delta=0$) and superconducting ($\Delta \neq 0$) regions does not influence our results. This can be seen explicitly from Figs. 4(a) and 4(b), where we compare the conductance matrices for systems when the scattering region is, respectively, entirely mixed with, or separated from, the superconducting region. There is no dependence on the exact position of the NS interface, as should be expected.

B. Varying the width of the superconductor

We now turn to the numerical calculations of the local and nonlocal conductances for an asymmetric device. We first vary the width W_1 of the superconducting lead, keeping the width of the normal terminals fixed, $W_2=W_3$. The doping throughout the device is set to a high value to ensure that many modes contribute to the transport. The conductances involving the normal terminals are calculated when the top terminal is superconducting (superscript S) and compared for reference to the conductance when the whole device is in the normal state (superscript N). As seen in Fig. 5, when the

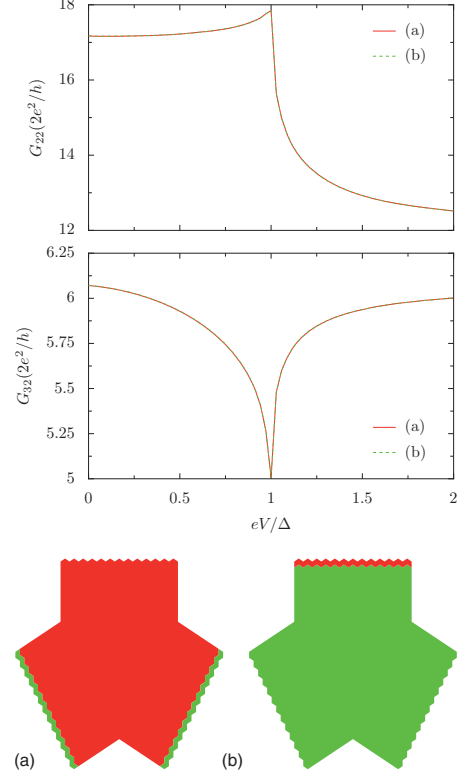


FIG. 4. (Color online) Dependence of local and nonlocal conductance on the position of the normal-superconductor (NS) interface. In (a), Δ is nonzero in the whole scattering region, while in (b) Δ is nonzero only in the top terminal. The conductances calculated for the two cases are identical, implying that the exact position of the NS interface is not important.

superconducting lead is very narrow, there is very little coupling via the induced superconducting order parameter, so $G_{22}^S \approx G_{22}^N$. However, as the width of the superconducting lead increases, more of the incoming quasiparticles are coupled via the induced superconducting order parameter, and the local conductance asymptotically approaches twice the normal-state conductance, $G_{22}^S \approx 2G_{22}^N$. In other words, the interaction with the superconductor essentially involves all the incoming modes, which are therefore Andreev reflected. This resembles the situation in a strongly coupled two-terminal NS junction.⁴³ From Fig. 5 we see that the contribution of Andreev reflection to the local conductance has reached its asymptotic value when $W_1/W_{2,3} \approx 2$.

The picture is essentially unchanged if we allow for different doping levels in the central device and the terminals [see Fig. 5(b)], as long as the number of contributing modes in the central region is still large. Contrary to what is seen for the local conductance, the nonlocal conductance G_{32} is only weakly influenced by the presence of the superconductor. Except for a slight enhancement of the signal around $W_1/W_{2,3} \approx 2$, the nonlocal conductance remains essentially

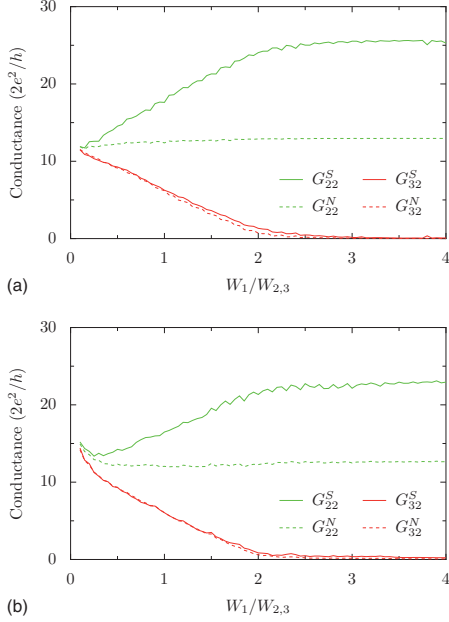


FIG. 5. (Color online) Local and nonlocal conductances as functions of the width W_1 of the superconducting lead. $W_2=W_3$ is kept fixed ($n_{W_{2,3}}=20$). For comparison we show the conductance both when the top lead is in the normal state (dashed) and when it is superconducting (solid).

unchanged when turning on the superconductor. This is in accordance with what was found for the symmetric device in Sec. IV, namely, that the Andreev reflected holes retrace the path of the incoming electrons, giving a negligible contribution to the nonlocal conductance. Again, different doping levels in the central device and the terminals do not change the picture qualitatively, as seen from Fig. 5(b).

C. Varying the width of normal terminal 3

We also vary the width W_3 of the normal terminal 3, keeping the widths of the voltage terminal 2 and the superconducting terminal 1 fixed. As can be seen from Fig. 6 the nonlocal conductance, G_{32} , is (nearly) zero when terminal 3 is very narrow. This is natural since the subband energies in terminal 3 increase as the terminal is made narrower, hindering any modes from carrying current at the Fermi energy. As the normal lead 3 widens, more and more channels in this lead are opened, and we get an increase in the conductance due to the opening of new subbands. The current in terminal 3 saturates when all available subbands participate in the transport. We observe that the superconductor has very little influence on the nonlocal conductance. As in Sec. V B, these results persist if we allow for different doping levels in the central device and the terminals, demonstrating the robustness of the results.

In contrast to the nonlocal conductance G_{32} , the local conductance G_{22} is strongly affected by the superconductor. G_{22}^S

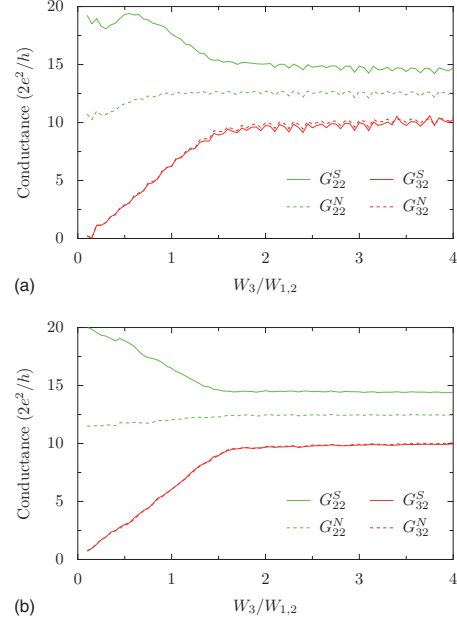


FIG. 6. (Color online) Local and nonlocal conductance as a function of the width W_3 of the right normal lead. $W_1=W_2$ is kept fixed ($n_{W_{1,2}}=20$). Doping levels and numerical method is the same as in Fig. 5.

doubles compared to the normal-state value G_{22}^N when the other normal lead becomes vanishingly small, $W_3/W_{1,2} \rightarrow 0$. This is as expected, since we are effectively left with a strongly coupled two-terminal NS junction involving only normal terminal 2 and superconducting terminal 1. In the opposite limit, when $W_3/W_{1,2} \gg 1$, the ratio G_{22}^S/G_{22}^N approaches an asymptotic value due to the fact that only a certain fraction of the finite number N_2 of incoming modes still interact with the superconductor, although the majority of these incoming modes are transferred directly to terminal 3 in this limit.

VI. NONLOCAL CONDUCTANCE DOMINATED BY CAR

A. Zero modes of zigzag nanoribbons

A zigzag graphene ribbon supports special current carrying zero-energy modes. When the doping is low (close to the Dirac point), the density of the zero-energy modes is localized along the ribbon edges,^{35,36} while the current is distributed approximately uniformly across the width of the ribbon.^{49–51} Associated with the zero-energy modes is a quantum number called pseudoparity, arising from the fact that the unit cell of the honeycomb lattice contains two atoms.^{37,52,53} The conservation of pseudoparity in a zigzag ribbon has dramatic consequences for the transport in a normal-superconducting (NS) junction when only the zero modes contribute, i.e., for Fermi energies below the first subband energy E_1 . In this regime each lead only supports one

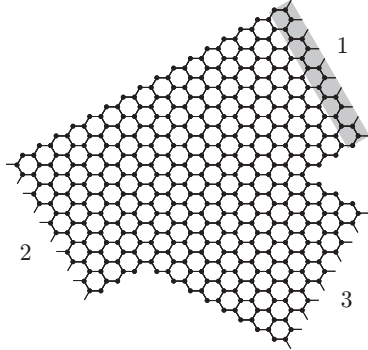


FIG. 7. Zigzag ribbon with a third terminal at 120° , where the top lead (shaded) be superconducting. The depicted structure corresponds to $n_W^{\text{ribbon}} = n_W^{\text{leg}} = 10$.

incoming and one outgoing mode. These two modes have either the same or opposite pseudoparities, depending on whether n_W is even or odd, respectively.³⁷ As a consequence of this, in a zigzag ribbon NS junction, either normal reflection or direct Andreev reflection will be entirely suppressed, depending on the value of n_W (modulo 2).³⁷ In a three-terminal device, pseudoparity is not a good quantum number, but when the transport involves only the zero modes, traces of even/odd effects can still be seen in the contributions due to Andreev reflection.

B. CAR dominance

Motivated by the results of Refs. 54–56, where it was found that a 120° kink in a graphene ribbon can in certain situations completely block the electron flow, we construct a device as depicted in Fig. 7, consisting of a zigzag ribbon with a third terminal protruding at an angle of 120° . The top terminal (1) is superconducting, while the left (2) and lower right (3) terminals are normal. We define $n_W^{\text{ribbon}} = n_W^1 = n_W^2$ and $n_W^{\text{leg}} = n_W^3$ and set $n_W^{\text{ribbon}} = n_W^{\text{leg}} = n_W$ in this section. The superconductor is heavily doped, while the doping in the nonsuperconducting part of the structure is kept close to the Dirac point. We study the transport properties as a function of back gate voltage V_g , which specifies the overall doping of the device, in the regime where only the zero modes contribute in the normal part of the device, $|V_g| < E_1$.

The numerical results in Fig. 8 show that the zero bias nonlocal conductance G_{32} changes sign several times in the regime $|eV_g| < E_1$. This demonstrates that CAR can in principle dominate ET in rather specific geometries. The nonlocal conductance changes sign due to close competition between ET and CAR. The oscillatory pattern is determined by the distance between the superconducting terminal and the scattering centre at the junction between the ribbon and terminal 3. The contribution from Andreev reflection is insensitive to this length, as seen from Fig. 8. Also, we observe that when $|eV_g| > E_1$, a new subband starts contributing to ET, while CAR remains approximately unchanged.

Finally, we also make a short comment on the even or odd behavior of our three-terminal device. By comparing our re-

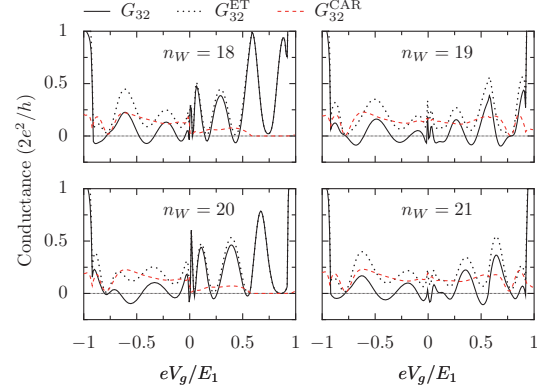


FIG. 8. (Color online) Nonlocal conductance G_{32} (solid black line) at zero bias as a function of back gate voltage V_g . The conductance changes sign due to the competition between ET (dotted black line) and CAR (dashed red line). A negative G_{32} corresponds to CAR dominating ET. The second subband starts to contribute when $|eV_g| > E_1$.

sults with the conductance $g_{22} = 2g_{22}^{\text{DAR}}$ in a two terminal NS ribbon (similar to the device in Fig. 7, but without terminal 3), we see that the even/odd behavior of g_{22}^{DAR} is reflected in G_{32}^{CAR} and G_{22}^{DAR} , as can be seen from Fig. 9. According to the results of Ref. 37, incoming carriers at positive and negative V_g have opposite (identical) pseudoparities in a ribbon with n_W even (odd). With our chosen doping in the superconductor, this leads to a blocking of Andreev reflection for positive V_g in the two-terminal ribbon (solid green line) when n_W is even. This feature is still manifest in the local DAR (dotted red line) and nonlocal CAR (dashed red line) contributions to the conductance in the three-terminal device.

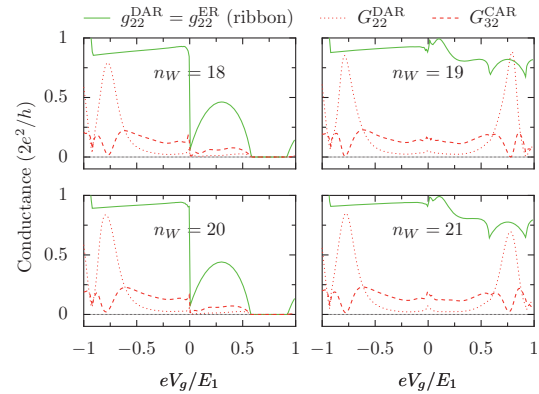


FIG. 9. (Color online) Comparison of Andreev reflection in a two terminal NS ribbon and in a three-terminal device as that shown in Fig. 7. The general behavior of direct Andreev reflection in the NS ribbon, g_{22}^{DAR} (solid green line), is reflected in the three-terminal crossed and direct Andreev reflection conductance G_{32}^{CAR} (dashed red line) and G_{22}^{DAR} (dotted red line).

VII. CONCLUSION

In this work we have studied the contribution from CAR and ET to the nonlocal transport in a device having two normal metal terminals and one superconducting terminal.

ET dominates CAR in a symmetric three-terminal device when the superconducting coherence length ξ greatly exceeds the device dimensions. The Andreev conversion process then contributes almost exclusively to direct Andreev reflection due to vanishing wave vector mismatch between electrons and back-reflected holes. This regime is relevant for ballistic transport in graphene nanoribbons devices of dimensions up to the micrometer scale.

Superconductivity can be induced in such structures via the proximity effect.

For most asymmetric systems ET dominates the nonlocal conductance. However, for asymmetric devices where the direct ET contribution can be suppressed, marginal CAR dominated charge transport is possible. The crossover from CAR to ET dominated transport in such a device can be induced by varying the overall doping of the device via a back gate.

ACKNOWLEDGMENT

This work was supported by the Research Council of Norway through Grant No. 167498/V30.

-
- ¹K. S. Novoselov, A. K. Geim, S. V. Morozov, D. Jiang, Y. Zhang, S. V. Dubonos, I. V. Grigorieva, and A. A. Firsov, *Science* **306**, 666 (2004).
- ²K. S. Novoselov, A. K. Geim, S. V. Morozov, D. Jiang, M. I. Katsnelson, I. V. Grigorieva, S. V. Dubonos, and A. A. Firsov, *Nature (London)* **438**, 197 (2005).
- ³Y. Zhang, Y.-W. Tan, H. L. Stormer, and P. Kim, *Nature (London)* **438**, 201 (2005).
- ⁴M. I. Katsnelson, K. S. Novoselov, and A. K. Geim, *Nat. Phys.* **2**, 620 (2006).
- ⁵G. W. Semenoff, *Phys. Rev. Lett.* **53**, 2449 (1984).
- ⁶A. K. Geim and K. S. Novoselov, *Nature Mater.* **6**, 183 (2007).
- ⁷A. H. Castro Neto, F. Guinea, N. M. R. Peres, K. S. Novoselov, and A. K. Geim, *Rev. Mod. Phys.* **81**, 109 (2009).
- ⁸H. B. Heersche, P. Jarillo-Herrero, J. B. Oostinga, L. M. van der Pijpen, and A. F. Morpurgo, *Solid State Commun.* **143**, 72 (2007).
- ⁹X. Du, I. Skachko, and E. Y. Andrei, *Phys. Rev. B* **77**, 184507 (2008).
- ¹⁰B. M. Kessler, C. O. Girit, A. Zettl, and V. Bouchiat, *Phys. Rev. Lett.* **104**, 047001 (2010).
- ¹¹G. Bignon, M. Houzet, F. Pistolesi, and F. W. J. Hekking, *Europhys. Lett.* **67**, 110 (2004).
- ¹²J. M. Byers and M. E. Flatté, *Phys. Rev. Lett.* **74**, 306 (1995).
- ¹³G. Deutscher and D. Feinberg, *Appl. Phys. Lett.* **76**, 487 (2000).
- ¹⁴G. Falci, D. Feinberg, and F. W. J. Hekking, *Europhys. Lett.* **54**, 255 (2001).
- ¹⁵J. P. Morten, A. Brataas, and W. Belzig, *Phys. Rev. B* **74**, 214510 (2006).
- ¹⁶J. P. Morten, D. Huertas-Hernando, W. Belzig, and A. Brataas, *Phys. Rev. B* **78**, 224515 (2008).
- ¹⁷D. Beckmann, H. B. Weber, and H. v. Löhneysen, *Phys. Rev. Lett.* **93**, 197003 (2004).
- ¹⁸P. Cadden-Zimansky and V. Chandrasekhar, *Phys. Rev. Lett.* **97**, 237003 (2006).
- ¹⁹A. Kleine, A. Baumgartner, J. Trbovic, and C. Schonenberger, *EPL* **87**, 27011 (2009).
- ²⁰S. Russo, M. Kroug, T. M. Klapwijk, and A. F. Morpurgo, *Phys. Rev. Lett.* **95**, 027002 (2005).
- ²¹N. M. Chtchelkatchev, G. Blatter, G. B. Lesovik, and T. Martin, *Phys. Rev. B* **66**, 161320(R) (2002).
- ²²P. Recher and D. Loss, *Phys. Rev. Lett.* **91**, 267003 (2003).
- ²³P. Recher, E. V. Sukhorukov, and D. Loss, *Phys. Rev. B* **63**, 165314 (2001).
- ²⁴R. Mélin, *J. Phys.: Condens. Matter* **13**, 6445 (2001).
- ²⁵A. Levy Yeyati, F. S. Bergeret, A. Martín-Rodero, and T. M. Klapwijk, *Nat. Phys.* **3**, 455 (2007).
- ²⁶D. S. Golubev and A. D. Zaikin, *EPL* **86**, 37009 (2009).
- ²⁷D. S. Golubev, M. S. Kalenkov, and A. D. Zaikin, *Phys. Rev. Lett.* **103**, 067006 (2009).
- ²⁸C. W. J. Beenakker, *Phys. Rev. Lett.* **97**, 067007 (2006).
- ²⁹P. Buset, A. Levy Yeyati, and A. Martín-Rodero, *Phys. Rev. B* **77**, 205425 (2008).
- ³⁰M. Titov and C. W. J. Beenakker, *Phys. Rev. B* **74**, 041401(R) (2006).
- ³¹C. Benjamin and J. K. Pachos, *Phys. Rev. B* **78**, 235403 (2008).
- ³²J. Cayssol, *Phys. Rev. Lett.* **100**, 147001 (2008).
- ³³A. R. Akhmerov and C. W. J. Beenakker, *Phys. Rev. B* **77**, 085423 (2008).
- ³⁴A. Rycerz, *Phys. Status Solidi A* **205**, 1281 (2008).
- ³⁵M. Fujita, K. Wakabayashi, K. Nakada, and K. Kusakabe, *J. Phys. Soc. Jpn.* **65**, 1920 (1996).
- ³⁶K. Nakada, M. Fujita, G. Dresselhaus, and M. S. Dresselhaus, *Phys. Rev. B* **54**, 17954 (1996).
- ³⁷D. Rainis, F. Taddei, F. Dolcini, M. Polini, and R. Fazio, *Phys. Rev. B* **79**, 115131 (2009).
- ³⁸S. Reich, J. Maultzsch, C. Thomsen, and P. Ordejón, *Phys. Rev. B* **66**, 035412 (2002).
- ³⁹P. R. Wallace, *Phys. Rev.* **71**, 622 (1947).
- ⁴⁰J. Bardeen, L. N. Cooper, and J. R. Schrieffer, *Phys. Rev.* **108**, 1175 (1957).
- ⁴¹M. Büttiker, *Phys. Rev. B* **46**, 12485 (1992).
- ⁴²G. E. Blonder, M. Tinkham, and T. M. Klapwijk, *Phys. Rev. B* **25**, 4515 (1982).
- ⁴³C. W. J. Beenakker, *Phys. Rev. B* **46**, 12841 (1992).
- ⁴⁴G. B. Lesovik, A. L. Fauch'ere, and G. Blatter, *Phys. Rev. B* **55**, 3146 (1997).
- ⁴⁵S. Datta, *Electronic Transport in Mesoscopic Systems*, Cambridge Studies in Semiconductor Physics and Microelectronic Engineering No. 3 (Cambridge University Press, Cambridge, England, 1995).

- ⁴⁶K. Kazymyrenko and X. Waintal, *Phys. Rev. B* **77**, 115119 (2008).
- ⁴⁷D. S. Fisher and P. A. Lee, *Phys. Rev. B* **23**, 6851 (1981).
- ⁴⁸A. Rycerz, J. Tworzydło, and C. W. J. Beenakker, *Nat. Phys.* **3**, 172 (2007).
- ⁴⁹F. Muñoz-Rojas, D. Jacob, J. Fernández-Rossier, and J. J. Palacios, *Phys. Rev. B* **74**, 195417 (2006).
- ⁵⁰L. P. Zarbo and B. K. Nikolic, *EPL* **80**, 47001 (2007).
- ⁵¹S. Nakakura, Y. Nagai, and D. Yoshioka, *J. Phys. Soc. Jpn.* **78**, 065003 (2009).
- ⁵²A. R. Akhmerov, J. H. Bardarson, A. Rycerz, and C. W. J. Beenakker, *Phys. Rev. B* **77**, 205416 (2008).
- ⁵³A. Cresti, G. Grosso, and G. P. Parravicini, *Phys. Rev. B* **77**, 233402 (2008).
- ⁵⁴A. Iyengar, T. Luo, H. A. Fertig, and L. Brey, *Phys. Rev. B* **78**, 235411 (2008).
- ⁵⁵M. I. Katsnelson and F. Guinea, *Phys. Rev. B* **78**, 075417 (2008).
- ⁵⁶A. Rycerz and C. W. J. Beenakker, arXiv:0709.3397 (unpublished).

Paper [4]

Focused crossed Andreev reflection

Submitted to Physical Review Letters (2010)

Focused Crossed Andreev Reflection

Håvard Haugen and Arne Brataas

Department of Physics, Norwegian University of Science and Technology, N-7491 Trondheim, Norway

Xavier Waintal

SPSMS-INAC-CEA, 17 rue des Martyrs, 38054 Grenoble CEDEX 9, France

Gerrit E. W. Bauer

Kavli Institute of NanoScience, Delft University of Technology, 2628 CJ Delft, The Netherlands

(Dated: October 14, 2010)

We consider non-local transport mediated by Andreev reflection in a two-dimensional electron gas (2DEG) connected to one superconducting and two normal metal terminals. A robust scheme is presented for observing crossed Andreev reflection (CAR) between the normal metal terminals based on electron focusing by weak perpendicular magnetic fields. At slightly elevated temperatures the CAR signature can be easily distinguished from a background of quantum interference fluctuations. The CAR induced entanglement between electrons can be switched on and off over large distances by the magnetic field.

PACS numbers: 74.45.+c, 73.23.-b

Andreev reflection (AR) is a signature sub-gap scattering phenomena at normal-superconductor (NS) interfaces. Two electrons (at energies symmetrically around the chemical potential of the superconductor) enter the superconducting condensate as a Cooper pair, resulting in a retro-reflected hole on the normal side of the interface. The superconducting coherence length ξ determines the spatial extent of the Cooper pairs and is therefore believed to govern the scale of the largest possible separation between the incoming electron and the retro-reflected hole.

When two normal metal contacts N_1 and N_2 are connected to a superconductor, the Andreev reflected holes due to incoming electrons in N_1 may leave the structure through N_2 [1–4]. This non-local process, called crossed Andreev reflection (CAR), creates a spatially separated phase-coherent electron-hole pair, and is therefore a candidate for a solid state entangler [5]. In this Letter, we show that CAR can be enhanced using electron focusing. In most previous works [1–8], the superconductor is attached to the two normal contacts in such a way that electron transfer (ET) between the normal electrodes only happens through co-tunneling via virtual states in the superconductor. This process normally competes with CAR and typically dominates in linear response [3, 9] such that CAR can dominate only beyond linear response or in the presence of interactions [8, 10, 12, 13]. In contrast, we spatially separate the superconductor and normal contacts, thus suppressing electron co-tunneling between the normal contacts while magnetic focusing allows to control the respective weights of ET and CAR processes.

Under direct coupling between the normal contacts and the superconductor, CAR can only be detected when the separation between the normal contacts is smaller than

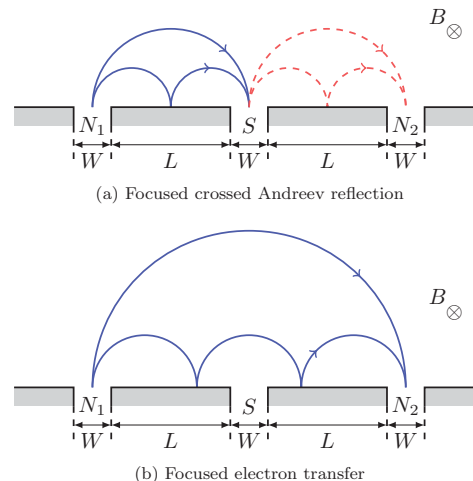


FIG. 1. (Color online) Illustration of focused crossed Andreev reflection in the device sketched in the inset of (a). (a) When the separation between N_1 and N_2 is an even multiple of the cyclotron diameter d_c , electron focusing enhances CAR and leads to a negative non-local conductance. (b) When the separation is an odd multiple of d_c , ET is enhanced and we expect a positive peak in the non-local conductance.

the superconducting coherence length ξ [2, 3, 5, 7, 11, 14]. Here we use the term CAR to describe all processes causing electron-hole entanglement between two normal metal contacts that are mediated by Andreev reflection, even when the contact separation is much larger than ξ . In our device, CAR competes with electron transfer

(ET), in which electrons travel between the normal contacts either directly (direct ET) or via multiple Andreev reflections.

Our system of choice is a high-mobility two-dimensional electron gas (2DEG) [15]. For a similar system Refs. [23, 24] reported electron focusing-induced negative non-local signal produced by resonant enhancement of AR. The resonances depend on the magnetic field such that fluctuations in the non-local signal due to AR are difficult to distinguish from quantum interference effects. Our approach is shown below to be more robust and better suited for entanglement creation.

Andreev reflection in the presence of a magnetic field has been thoroughly studied in the literature [19–24]. Electron focusing was used for the first direct observation of Andreev reflection at an NS interface [19, 22]. Recently, an Andreev interferometer was used to demonstrate phase coherence of CAR and ET [11].

Our scheme is illustrated in Fig. 1, which shows a 2DEG connected to a single superconducting contact S between two normal contacts N_1 and N_2 . Electrons are injected from the left contact N_1 by a small voltage bias. For weak magnetic fields, the motion of the electrons and holes can be understood in terms of semi-classical cyclotron orbits [15, 19]. For certain magnetic fields (Fig. 1(a)), the electrons from N_1 are focused on the superconducting center contact S , at which an Andreev reflected hole is emitted. Since AR changes the sign of both charge and effective mass, the holes will feel the same Lorentz force as the electrons and are therefore focused on contact N_2 to the right of S at the same distance as N_1 [19–21]. At these magnetic fields, direct ET is suppressed in favor of CAR. A contribution to ET at these fields from multiple Andreev reflections is suppressed by the magnetic field together with back-scattering towards the superconductor. On the other hand, ET is enhanced when the incoming electrons are focused on N_1 such that the skipping orbits do not interact with the superconductor (Fig. 1(b)).

The physics of electron focusing can be best understood in a semi-classical picture. The length scale associated with the motion of electrons with momentum $\hbar k_F$ in a magnetic field B is the cyclotron diameter, $d_c = 2\hbar k_F/eB$, where we assume ballistic kinetics or $d_c \ll l_{mf}$ [15]. Electron focusing between the normal contacts in Fig. 1 occurs when the distance $2L$ between N_1 and N_2 obeys $2L = nd_c$, where n is a positive integer. ET is enhanced for odd and CAR for even n . The field [15]

$$B_{\text{focus}} = \frac{2\hbar k_F}{eL} \quad (1)$$

determines the scale for which focusing features can be expected.

For strong magnetic fields the system enters the quantum Hall (QH) regime, in which the charge carriers are

better described as chiral edge states than semi-classical skipping orbits [16]. The characteristic length scale associated with the QH regime is the magnetic length l_B , which is the radius of the disc that encloses one flux quantum, $\pi l_B^2 B = \Phi_0 = h/2e$. In the semi-classical regime the magnetic flux density $n_B = 1/(\pi l_B^2)$ should be substantially lower than the electron density $n = k_F^2/(2\pi)$, giving $B \ll \frac{h}{2e} n \approx 7$ T, for typical values for the electron density in a 2DEG, $n \approx 3.5 \times 10^{15} \text{ m}^{-2}$ (corresponding to $\lambda_F \approx 40$ nm) [15]. We expect CAR to be enhanced also in the QH regime, since the edge states will be forced to interact with the superconductor on the way from N_1 to N_2 . This regime should be experimentally accessible since superconductors with upper critical fields above 10 T are readily available [25].

We will now confirm the semi-classical predictions by a numerical quantum simulation of the non-local transport properties of the device shown in Fig. 1. The competition between CAR and ET is studied through the non-local conductance [3, 9],

$$G_{21} \stackrel{\text{def}}{=} -\frac{\partial I_2}{\partial V_1} = G_{21}^{\text{ET}} - G_{21}^{\text{CAR}}, \quad (2)$$

where I_2 is the current response in contact N_2 due to the application of a voltage V_1 in the normal metal contact N_1 while N_2 and S are grounded. The overall minus sign is due to the definition of the currents to be positive when electrons leave the reservoirs. The difference in sign of G_{21}^{ET} and G_{21}^{CAR} in Eq. (2) is due to the fact that the outgoing current in N_2 produced by ET consists of negatively charged electrons, while CAR contributes with positively charged holes.

In our calculation we employ the standard 2DEG Hamiltonian

$$\mathcal{H}(\mathbf{r}) = \frac{\mathbf{p}^2}{2m} + V(\mathbf{r}) - \mu, \quad (3)$$

where $\mathbf{p} = -i\hbar\nabla + e\mathbf{A}(\mathbf{r})$ is the momentum and m the effective mass. The Hamiltonian (3) is extended to Nambu space [26]

$$H = \int d\mathbf{r} \Psi^\dagger(\mathbf{r}) \begin{pmatrix} \mathcal{H}(\mathbf{r}) & \Delta(\mathbf{r}) \\ \Delta^*(\mathbf{r}) & -\mathcal{H}^*(\mathbf{r}) \end{pmatrix} \Psi(\mathbf{r}), \quad (4)$$

where at the contact S the superconducting pair potential $\Delta(\mathbf{r})$ is assumed to vary abruptly on the scale of the Fermi wavelength λ_F , and is therefore modelled as step function which is non-zero only inside the center contact S . All energies are measured from the chemical potential μ of the superconductor. The Nambu spinor Ψ is defined in terms of the field operators ψ as $\Psi = (\psi, \psi^\dagger)^T$. A perpendicular magnetic field $\mathbf{B} = \nabla \times \mathbf{A} = B\mathbf{e}_z$ is included everywhere except in the superconductor [27]. We consider only elastic scattering.

At zero temperature, quantum interference due to scattering at the sharp boundaries close to the contacts can

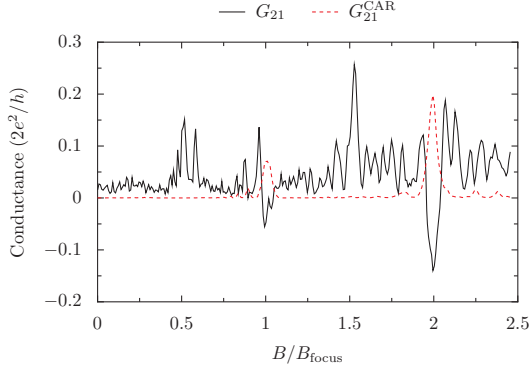


FIG. 2. (Color online) Non-local conductance G_{21} (solid black) for a device with quantum point contacts ($W \approx \lambda_F/2$). The magnetic field is given in units of the focusing field $B_{\text{focus}} = 0.406$ T. The plot of G_{21}^{CAR} (dashed red) demonstrates that the negative peaks in G_{21} at integer multiples of B/B_{focus} are a direct consequence of $G_{21}^{\text{CAR}} > G_{21}^{\text{ET}}$ in Eq. (2).

mask the electron focusing effect [15]. We therefore calculate the non-local differential conductance at finite temperature, using the standard formula,

$$G_{21} = \int d\varepsilon G_{21}(\varepsilon) \left(-\frac{\partial n_F(\varepsilon)}{\partial \varepsilon} \right), \quad (5)$$

where n_F is the Fermi-Dirac distribution function.

We use the knitting algorithm presented in Ref. 28 to calculate the self energies and retarded and advanced Green functions. Standard expressions relate the conductance and current density to these quantities. The device used in the simulations is sketched in the inset of Fig. 1(a), where the two auxiliary contacts N_3 and N_4 are drains for the electrons that do not contribute to the resonances. All edges cause specular electron scattering only.

Figure 2 shows the calculated non-local conductance from Eq. (5) as a function of perpendicular magnetic field at a temperature of $T = 1$ K. The value chosen for the pair potential Δ corresponds to Pb, which has a critical temperature of $T_c \approx 7$ K $\gg T$ [29]. Also, since $T < T_c/2$, we disregard the temperature dependence of the pair potential, $\Delta(T) \approx \Delta(0)$ [30].

The injector N_1 , superconducting S , and collector N_2 contacts are point contacts with width $W \approx \lambda_F/2$, so that only a single mode contributes to the current [16]. The distance $L = 500$ nm between the contacts corresponds to a focusing field of $B_{\text{focus}} = (0.39 \pm 0.02)$ T, where the uncertainty is due to the finite width W of the contacts relative to L . The value found in the simulation agrees with the expectations within this uncertainty.

In Fig. 2 the total non-local conductance G_{21} is shown together with the conductance contribution due to CAR.

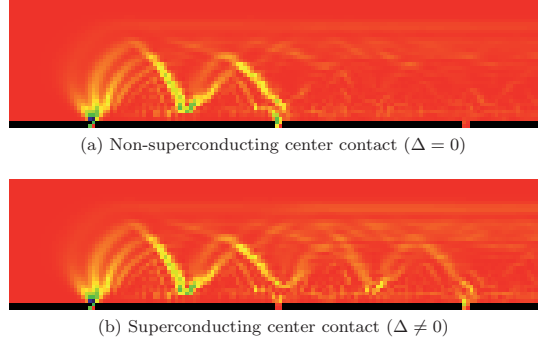


FIG. 3. (Color online) Electronic current density in a perpendicular magnetic field at $T = 1$ K. Two skipping orbits, corresponding to a magnetic field $B \approx 2B_{\text{focus}}$, are clearly visible. (a) With a non-superconducting center contact S , a large portion of the current injected through contact N_1 leaves the structure through S . (b) When S is superconducting, the Andreev reflected holes from S contribute to the current from S to N_2 .

The negative peaks in G_{21} at integer values of the focusing field are consistent with the semi-classical interpretation presented earlier, and demonstrate that ET is completely dominated by CAR for such fields. The expected enhancement of ET at half-integer B/B_{focus} is somewhat masked by quantum interference, but positive peaks in G_{21} when B/B_{focus} equals $1/2$ and $3/2$ are clearly visible. The field associated with focusing can easily be adjusted to be well separated from the scale of quantum interference by changing the distance L between the contacts. As the magnetic field increases beyond $2.5 B_{\text{focus}}$, the system gradually enters the QH regime.

The enhancement of CAR at $B/B_{\text{focus}} = 1, 2$ can be visualized by calculating the charge current density due to electrons injected from contact N_1 . This is shown in Fig. 3, where we have set $B \approx 2B_{\text{focus}}$. A skipping orbit between N_1 and S is clearly visible. Also visible is the diffraction of the incoming current through N_1 , which leads to a broadening of the skipping orbit trajectories. In Fig. 3(a) the center contact S is normal ($\Delta = 0$) and a large portion of the injected current leaves through S . In contrast, when S is in the superconducting state, as shown in Fig. 3(b), the current density increases substantially between S and N_2 due to CAR.

Electron focusing over length scales for which AR mediated electron-hole correlations can be observed is limited by the mean free path l_{mf} rather than the superconducting coherence length ξ [23]. For typical superconductors, $\xi \sim 10 - 100$ nm, [12] whereas l_{mf} can reach several microns in 2DEGs [16]. Very high mobilities have also been reported for graphene [17, 18], which is another candidate for focused CAR. The tuning between CAR and ET is possible only below the critical magnetic

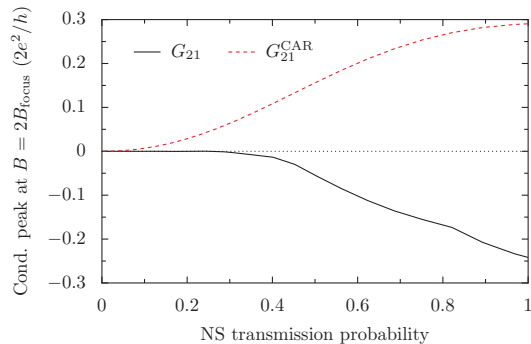


FIG. 4. (Color online) G_{21} and G_{21}^{CAR} at $B/B_{\text{focus}} = 2$ as a function of transmission probability of the interface between the 2DEG and the superconductor. The conductance is calculated at zero temperature.

field of the superconductor, and should also not introduce spin selectivity of the contacts. Since electron focusing clearly discriminates between CAR and ET, our device can maximize entanglement generation in artificial solid state devices.

Contacts between superconducting metals and 2DEGs has been fabricated for several types of heterostructures [31, 32]. Although experimentally challenging due to the presence of Schottky barriers, fairly high transparencies have been reported (for instance transmission probability ~ 0.55 with a critical field of 2T in the In-GaAs heterostructures presented in Ref. 32). In Fig. 4, we plot the height of the CAR peak at $B/B_{\text{focus}} = 2$ (at $T = 0$) as a function of the transmission probability of the NS contact. The CAR peak diminishes with decreasing quality of the interface but not dramatically so. We conclude that the effect should be observable with the available technology.

In conclusion, we have shown that electron focusing can be used to enhance CAR relative to quantum interference effects over the length scale of the mean free path l_{mf} [23], which can be several orders of magnitude larger than ξ [12, 15]. CAR is enhanced at the cost of ET for magnetic fields that are integer multiples of the focusing field in Eq. (1), producing a clear, negative non-local conductance signal. At half integer multiples of the focusing field, CAR plays a negligible role since the electron orbits avoid the superconducting contact. Instead ET is enhanced as in normal electron focusing [15]. The necessary magnetic field is relatively weak, and should be an easily accessible experimental “knob” for controlling the CAR enhancement.

CAR has been proposed as a means to create a solid state entangler, using the natural entanglement of Cooper pairs. However, in most systems quasiparticle backscattering into the injector contacts is a serious lim-

itation [33]. This difficulty does not exist in our scheme.

This work was supported by The Research Council of Norway through grant no. 167498/V30.

-
- [1] J. M. Byers and M. E. Flatté, Phys. Rev. Lett., **74**, 306 (1995).
 - [2] G. Deutscher and D. Feinberg, Appl. Phys. Lett., **76**, 487 (2000).
 - [3] G. Falci, D. Feinberg, and F. W. J. Hekking, Europhys. Lett., **54**, 255 (2001).
 - [4] D. Feinberg, Eur. Phys. J. B, **36**, 419 (2003).
 - [5] P. Recher, E. V. Sukhorukov, and D. Loss, Phys. Rev. B, **63**, 165314 (2001).
 - [6] S. G. den Hartog, C. M. A. Kapteyn, B. J. van Wees, T. M. Klapwijk, and G. Borghs, Phys. Rev. Lett., **77**, 4954 (1996).
 - [7] D. Beckmann, H. B. Weber, and H. v. Löhneysen, Phys. Rev. Lett., **93**, 197003 (2004).
 - [8] S. Russo, M. Kroug, T. M. Klapwijk, and A. F. Morpurgo, Phys. Rev. Lett., **95**, 027002 (2005).
 - [9] J. P. Morten, A. Brataas, and W. Belzig, Phys. Rev. B, **74**, 214510 (2006); J. P. Morten, D. Huertas-Hernando, W. Belzig, and A. Brataas, *ibid.*, **78**, 224515 (2008).
 - [10] P. Cadden-Zimansky and V. Chandrasekhar, Phys. Rev. Lett., **97**, 237003 (2006).
 - [11] P. Cadden-Zimansky, J. Wei, and V. Chandrasekhar, Nat. Phys., **5**, 393 (2009).
 - [12] A. Levy Yeyati, F. S. Bergeret, A. Martín-Rodero, and T. M. Klapwijk, Nat. Phys., **3**, 455 (2007).
 - [13] D. S. Golubev, M. S. Kalenkov, and A. D. Zaikin, Phys. Rev. Lett., **103**, 067006 (2009).
 - [14] J. Wei and V. Chandrasekhar, Nat. Phys., **6**, 494 (2010).
 - [15] H. van Houten, C. W. J. Beenakker, J. G. Williamson, M. E. I. Broekaart, P. H. M. van Loosdrecht, B. J. van Wees, J. E. Mooij, C. T. Foxon, and J. J. Harris, Phys. Rev. B, **39**, 8556 (1989).
 - [16] C. W. J. Beenakker, H. van Houten, and B. J. van Wees, Superlattices Microstruct., **5**, 127 (1989).
 - [17] K. Bolotin, K. Sikes, Z. Jiang, M. Klima, G. Fudenberg, J. Hone, P. Kim, and H. Stormer, Solid State Commun., **146**, 351 (2008).
 - [18] F. Chen, J. Xia, and N. Tao, Nano Lett., **9**, 1621 (2009).
 - [19] P. A. M. Benistant, H. van Kempen, and P. Wyder, Phys. Rev. Lett., **51**, 817 (1983).
 - [20] V. S. Tsoi, J. Bass, and P. Wyder, Rev. Mod. Phys., **71**, 1641 (1999).
 - [21] F. Giazotto, M. Governale, U. Zülicke, and F. Beltram, Phys. Rev. B, **72**, 054518 (2005).
 - [22] S. I. Bozhko, V. S. Tsoi, and S. E. Yakovlev, Pis'ma Zh. Eksp. Teor. Fiz, **36**, 123 (1982), [JETP Lett. 36, 152 (1982)].
 - [23] P. K. Polinák, C. J. Lambert, J. Koltai, and J. Cserti, Phys. Rev. B, **74**, 132508 (2006).
 - [24] P. Rakytá, A. Kormányos, Z. Kaufmann, and J. Cserti, Phys. Rev. B, **76**, 064516 (2007).
 - [25] H. J. Niu and D. P. Hampshire, Phys. Rev. Lett., **91**, 027002 (2003).
 - [26] Y. Nambu, Phys. Rev., **117**, 648 (1960).
 - [27] H. Hoppe, U. Zülicke, and G. Schön, Phys. Rev. Lett., **84**, 1804 (2000).

- [28] K. Kazymyrenko and X. Waintal, *Phys. Rev. B*, **77**, 115119 (2008).
- [29] D. P. Lide, ed., *CRC Handbook of Chemistry and Physics*, 90th ed. (CRC Press, 2010).
- [30] J. Bardeen, L. N. Cooper, and J. R. Schrieffer, *Phys. Rev.*, **108**, 1175 (1957).
- [31] H. Takayanagi and T. Kawakami, *Phys. Rev. Lett.*, **54**, 2449 (1985).
- [32] S. Boulay, J. Dufouleur, P. Roche, U. Gennser, A. Cavanna, and D. Mailly, *J. Appl. Phys.*, **105**, 123919 (2009).
- [33] J. P. Morten, D. Huertas-Hernando, W. Belzig, and A. Brataas, *Europhys. Lett.*, **81**, 40002 (2008).

